Experimental and Computational Assessment of High-Temperature Properties in Ti-Based High Entropy Alloys

by

Alireza Nazarahari

A Dissertation Submitted to the Graduate School of Sciences and Engineering in Partial Fulfillment of the Requirements for the Degree of Doctor of Philosophy in

Mechanical Engineering

KOÇ ÜNİVERSİTESİ

January 9, 2024

Experimental and Computational Assessment of High-Temperature Properties in Ti-Based High Entropy Alloys

Koç University

Graduate School of Sciences and Engineering

This is to certify that I have examined this copy of a doctoral dissertation by

Alireza Nazarahari

and have found that it is complete and satisfactory in all respects,
and that any and all revisions required by the final examining
committee have been made.

Committee Members:

_____
Prof. Demircan Canadinç (Advisor)

_____
Prof. Hans Jürgen Maier

_____
Prof. Murat Sözer

_____
Assoc. Prof. Uğur Unal

_____
Assist. Prof. Sıdıka Mine Toker

Date: _____

Per Aspera Ad Astra!

ABSTRACT

Experimental and Computational Assessment of High-Temperature Properties in Ti-Based High Entropy Alloys

Alireza Nazarahari

Doctor of Philosophy in Mechanical Engineering

January 9, 2024

During the last two decades, high entropy alloys (HEAs) have gained noticeable attention due to their outstanding properties and potential for various applications. Within the prospective applications, due to their high melting point and high thermal stability, refractory high entropy alloys (RHEAs) are considered an alternative to Ni-based superalloys for high-temperature applications. Therefore, in order to shed light on the high-temperature properties of RHEAs, two aspects of their properties were investigated. After a brief introduction to the concepts discussed in this thesis, the oxidation behavior of four different HEAs was investigated via static oxidation experiments utilizing a variety of surface and structural characterization methods such as X-ray photon spectrometry (XPS), X-ray diffraction (XRD), scanning electron microscopy (SEM). The results suggested that three different oxidation mechanisms in these alloys are dependent on the composition, temperature, and crystal structure of the HEAs. In addition, each element's effect on these alloys' oxidation behavior was discussed. In the second part of the thesis, using atomistic simulations, the effect of the formation of chemical short-range order (CSRO) on mechanical properties was investigated in two different compositions of RHEAs. The results showed that the CSRO formation in these alloys can increase the materials' strength while maintaining the HEAs' ductility. In addition, the effect of CSROs on deformation-induced phase transformation (DIPT) was captured via atomistic simulations. To validate these results, an extensive amount of in-situ compression experiments under SEM were performed and these results validated the formation of HCP phases due to DIPT. Overall, the results and discussions in this thesis provide a better view of the high-temperature properties of the HEAs with the aim of enabling their applications at high temperatures.

ÖZETÇE

Ti-Bazlı Yüksek Entropili Alaşımların Yüksek Sıcaklık Özelliklerinin Deneysel ve Hesaplamalı Değerlendirilmesi

Alireza Nazarahari

Makine Mühendisliği, Doktora

9 Ocak 2024

Son yirmi yılda, yüksek entropili alaşımlar (HEA'lar), olağanüstü özellikleri ve çeşitli uygulama potansiyelleri nedeniyle dikkat çekici bir ilgi kazanmıştır. İleriye dönük uygulamalarda, yüksek erime noktaları ve yüksek termal stabiliteleri nedeniyle, refrakter yüksek entropi alaşımlar (RHEA) lar, yüksek sıcaklık uygulamaları için Ni Bazlı süper alaşımlara alternatif olarak kabul edilmektedir. Bu nedenle RHEA'ların yüksek sıcaklık özelliklerine ışık tutmak için özellikleri iki farklı yönden araştırıldı. Bu tezde tartışılan kavramlara kısa bir giriş yapıldıktan sonra, dört farklı HEA'nın oksidasyon davranışı, X-ışını foton spektrometresi (XPS), X-ışını kırınımı (XRD), taramalı elektron mikroskobu (SEM) gibi çeşitli yüzey ve yapısal karakterizasyon yöntemleri kullanılarak statik oksidasyon deneyleri yoluyla incelenmiştir. Sonuçlar, bu alaşımlardaki üç farklı oksidasyon mekanizmasının HEA'ların bileşimine, sıcaklığına ve kristal yapısına bağlı olduğunu göstermiştir. Ayrıca her bir elementin bu alaşımların oksidasyon davranışı üzerindeki etkisi tartışılmıştır. Tezin ikinci bölümünde atomistik simülasyonlar kullanılarak kimyasal kısa menzilli düzen (CSRO) oluşumunun HEA'ların iki farklı bileşimi üzerindeki etkisi araştırılmıştır. Sonuçlar, bu alaşımlardaki CSRO oluşumunun, HEA'ların sünekliğini korurken malzemelerin mukavemetini artırabildiğini gösterdi. Ek olarak, deformasyona bağlı faz dönüşümü (DIPT) etkisi atomistik simülasyonlar aracılığıyla ortaya koyuldu. Bu sonuçları doğrulamak için SEM altında çok sayıda yerinde (in-situ) sıkıştırma deneyi yapıldı ve bu sonuçlar, DIPT etkisinin bir sonucu olarak HCP fazlarının oluşumunu doğruladı. Genel olarak, bu tezdeki sonuçlar ve tartışmalar, yüksek sıcaklıklarda uygulamalarını mümkün kılmak amacıyla HEA'ların yüksek sıcaklık özelliklerine ilişkin daha iyi bir görüş sağlamıştır.

ACKNOWLEDGMENTS

I would like to express my sincere gratitude to my Ph.D. advisor, Prof. Demircan Canadinç, for his constant support, both scientifically and personally, since starting my M.Sc. in 2019. His guidance and mentorship were essential parts of my Ph.D. studies; without them, my Ph.D. would have gone down a different path.

My sincere appreciation goes to the dissertation committee, Prof. Murat Sözer, and Assoc. Prof. Uğur Unal, for their numerous valuable suggestions in my thesis progress committee. I also want to thank Prof. Hans Jürgen Maier and Assist. Prof. Sıdıka Mine Toker for their insightful feedback and contributions to my Ph.D. thesis.

In addition, I wanted to thank my colleague and friend, Mr. Hüseyin Can Özdemir, for all we went through in the last four years, both in the work environment and in life. Moreover, I wanted to thank Mr. Christian Hinte for being a great host during my work visits to Germany and being a brilliant scientist who shared valuable information on many topics. In addition, I need to thank Ms. Anja Krabbenhöft and Ms. Ece Kesme for their help with some of the surface characterizations in this work.

I also need to thank my friends who were there for me whenever I was in trouble: Ms. Yağmur Ersoy, Ms. Ezgi Demiröz, Ms. Tatiana Blank, and Ms. Bengisu Yılmaz. My life as an international student would have been much different without them. I also should not forget the people whose support, even from a long distance, was essential to me, My family, and Ms. Maryam Hedayat.

Finally, I wanted to thank the Graduate School of Science and Engineering (GSSE) at Koç University and the Institute für Werkstoffkunde (IW) in Leibniz Universität Hannover for their financial support.

TABLE OF CONTENTS

LIST OF TABLES

LIST OF FIGURES

ABBREVIATIONS

at.%	Atomic Percent
BCC	Base Centered Cubic
BCT	Body Centered Tetragonal
CCA	Chemically Complex Alloys
DIPT	Deformation-Induced Phase Transformation
EDM	Electric Discharge Machine
EDX	Energy Dispersive X-ray
FCC	Face Centered Cubic
FF	Force Field
GIXRD	Grazing Incident X-ray Diffraction
HEA	High Entropy Alloy
LAMMPS	Large-Scale Atomic/Molecular Massively Parallel Simulator
MC	Monte Carlo
MD	Molecular Dynamics
MEA	Medium Entropy Alloy
PBR	Pilling-Bedworth Ratio
PVD	Physical Vapor Deposition
RF	Radio Frequency
RHEA	Refractory High Entropy Alloy
SE	Secondary Electron
SEM	Scanning Electron Microscopy
TRIP	Transformation-Induced Plasticity
VAR	Vacuum Arc Remelting
XPS	X-ray Photo Spectrometry
XRD	X-ray Diffraction

Chapter 1:
INTRODUCTION

1.1 High Entropy Alloys (HEAs)

High Entropy Alloys (HEAs), also known as Chemically Complex Alloys (CCAs) and multi-principle alloys, are a group of novel alloys that gained noticeable attention within the last 20 years thanks to their interesting properties and potential applications. These alloys typically contain four or more elements with contents ranging between 5-35 at.% and were introduced simultaneously by two groups in 2004 [1, 2]. The idea behind the development of HEAs was to investigate the parts of the phase diagram that contained single-phase solid solutions but were far from the compositions of conventional alloys (dilute solutions of alloying elements inside a primary component) [1]. Initially, four core effects were suggested to describe the unconventional properties of these alloys [3]. These effects were:

1- High (configurational) entropy effect:

The idea behind the high entropy effect, suggested by Yeh et al., was that increasing the number of elements results in higher configurational entropy of the alloy. Therefore, the Gibbs free energy of the single-phase solid solution is lower than the intermetallic compounds. To be more specific, if the Gibbs free energy is defined as:

$$\Delta G = \Delta H - T\Delta S \qquad (1.1)$$

Then, the $\Delta G_{solid\ solution} < \Delta G_{Intermetallic}$ due to the fact that $\Delta S_{configurational}$ is higher in the HEAs compared to intermetallic compounds [2]. Although this idea theoretically seems reasonable, numerous HEAs that do not follow this rule and form various intermetallic compounds have been found [4, 5]. In fact, only a handful of HEAs form single-phase solid solutions, suggesting the importance of enthalpic effects in the thermodynamics of phase formation.

2- Severe lattice distortion:

As mentioned before, HEAs are composed of several elements, each with a different atomic radius and electro-negativity. As a result, the lattice of HEAs would experience a high degree of distortion due to the mismatch of these elements. The lattice mismatch can

cause difficulty in the movement of dislocations and diffusion of alloys, as reported in several studies [6, 7]. However, more recent studies questioned the extent of the mismatch compared to conventional alloys. These studies suggest that the lattice distortion amount, although larger, is not significantly higher than some conventional alloys [8, 9].

3- Sluggish diffusion:

The mismatch of properties between different atoms of HEAs can cause a more difficult movement of atoms within the lattice compared to conventional alloys. Therefore, theoretically, the diffusion rate in HEAs is expected to be sluggish, resulting in higher stability of alloys at higher temperatures. However, several recent studies pointed out that the effect of high configurational entropy and the lattice mismatch does not directly cause sluggish diffusion. In other words, the slow diffusion in HEAs are a result of elemental effect rather than a general rule [10-12]

4- Cocktail effect:

The compositional nature of the HEAs demands combining several elements in large portions. Therefore, occasionally, this combination results in a synergic effect compared to the conventional alloys of that element. As a result of this combination, it is possible to tailor the properties of HEAs to gain properties exceeding the boundaries of conventional alloys [13].

Although the theory behind the HEAs has changed during the last two decades, and some of the initial ideas about mechanisms in HEAs were proven to be inaccurate, many HEAs with interesting properties have been developed as a result of these studies. Out of these alloys, two families of HEAs attracted the most attention: Cantor alloys based on CrCoFeMnNi and Senkov alloys based on HfNbTaTiZr, which showed interesting microstructure that made them worthwhile for an extensive amount of studies [1, 14]. To be more specific, the original Cantor alloy forms a face centered cubic (FCC) structure and has shown sluggish diffusion, Transformation-induced plasticity (TRIP), and Twinning-induced plasticity (TWIP) properties that made them promising for applications that demand superior mechanical properties [15, 16]. On the other hand, the original Senkov alloy (HfNbTaTiZr) has a BCC structure showing ductility at room temperature while being composed of refractory elements with high melting points, therefore, a potential alloy for high-temperature applications [17]. A summary of these properties is provided in Figure 1.1. As this thesis is intended to shed light on the high-temperature properties of HEAs, the focus will be on the Senkov family of alloys.

1.2 Potential applications of the HfNbTaTiZr family of HEAs

Studies on the properties of the HfNbTaTiZr family of HEAs showed their promising properties for two categories of applications: biomedical applications and high-temperature applications. The path for investigating biomedical and orthopedic applications is incentivized by the fact that none of the elements in the HfNbTaTiZr are known to be toxic in the human body [18], and these alloys have shown decent corrosion resistance in in-vitro biocompatibility experiments [19-22]. In addition, several studies pointed out the fact that HfNbTaTiZr and its derivatives have lower elastic modulus compared to conventional biomedical alloys such as CoCr-based or Ti-Based alloys [23, 24]. The low elastic modulus is essential for orthopedic implants as the high deviation between elastic modulus of the alloy and the human bone causes a shielding effect. The shielding effect results in weakening the connection between the orthopedic implant and human bone by damaging the bone tissue, leading to the failure of the treatment [25].

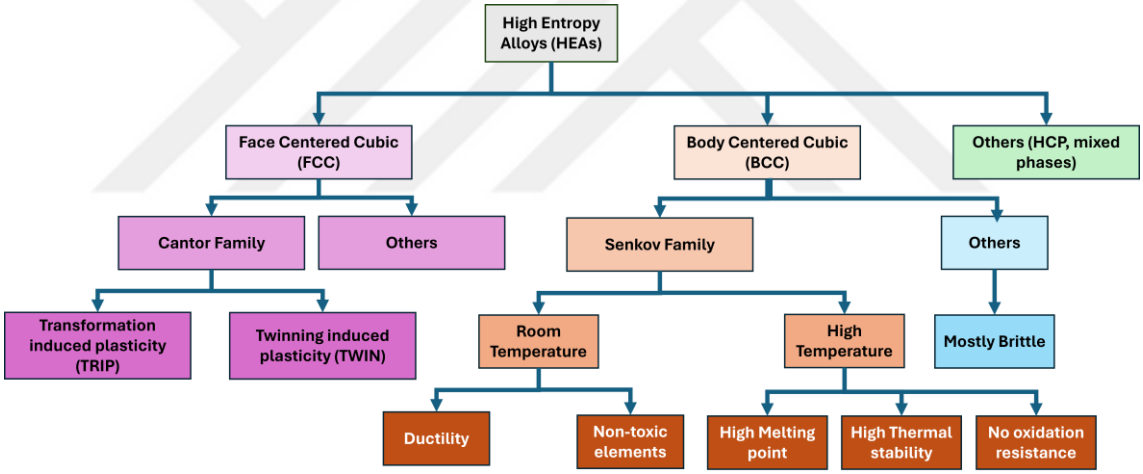

Figure 1.1 Schematic of different families of HEAs and their important properties.

On the other hand, the potential for high-temperature applications of HEAs is perceived due to the possibility of using high melting point elements in the composition of alloys and their thermal stability and strength at high temperatures [26-28]. In fact, refractory high entropy alloys (RHEAs) that are made of refractory metallic elements have the capacity to replace nickel superalloys in high-temperature applications. In particular, the current design of highly efficient jet engines is constrained by the fact that even when internal cooling methods are applied, the working temperature of the engines is very close to the current nickel-based superalloys' melting point. Therefore, increasing the working temperature of the engines and their efficiency, is restricted by the lack of sufficiently

strong material [29]. As a result, any material with a high melting point and acceptable mechanical properties can be highly desirable, making RHEA family of alloy a potent candidate. These alloys are commonly made of elements such as Hf, Nb, Ta, Ti, Zr, V, and Mo, which pass the criteria of higher melting point than Ni. In addition, several studies pointed out their significant high-temperature strength and thermal stability [30, 31]. However, despite their favorable mechanical properties, these alloys greatly suffer from low oxidation resistance at high temperatures and need compositional optimization to enhance their oxidation properties [32, 33].

1.3 Oxidation in Metallic Materials

By definition, an oxidation reaction is when an element chemically reacts with oxygen atoms and forms a new compound containing oxygen. Oxidation is a spontaneous process that can happen at any temperature, depending on the atmosphere of the element and its oxygen affinity. In materials engineering, oxidation can be used as a tool to form a hard oxide layer on the surface of materials that can increase their hardness and corrosion resistance. However, in high-temperature applications, oxidation is usually considered a problem to solve, rather than a desirable property [34, 35].

In order to understand the oxidation properties of an alloy, it is necessary to understand its mechanism of oxidation, which can be different depending on each alloy. However, to give a simplified and generalist view of oxidation mechanisms in metallic materials, we can consider the following steps as depicted in Figure 1.2:

1- The oxygen molecules are delivered to the Gas-Scale interface due to mass transfer phenomena in the gas phase.
2- Oxygen atoms are incorporated into the oxide scale in the interface.
3- The reacting metal atoms from the bulk alloy are delivered to the alloy-scale interface.
4- The metal atom is incorporated into the oxide scale in the interface.
5- Transport of atoms of metal or/and oxygen within the scale [34, 36].

After the transportation phenomena mentioned above, the chemical reaction can occur within the scale.

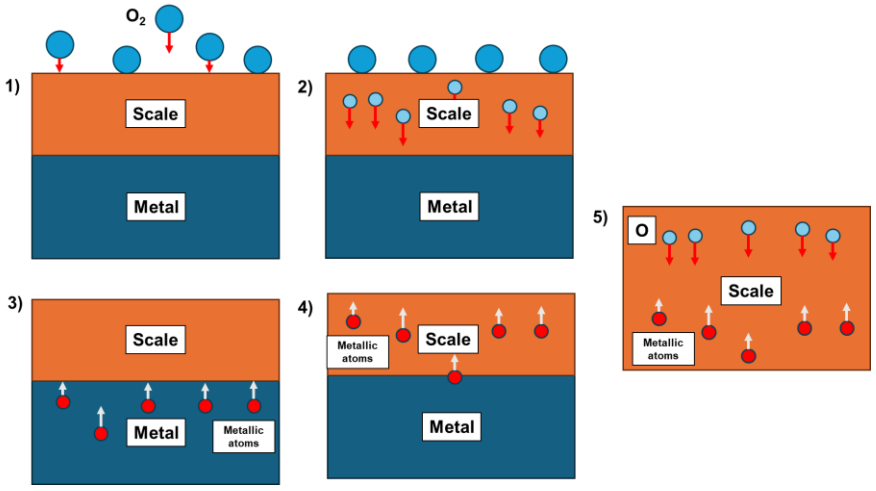

Figure 1.2 Depicting the transformation phenomena related to the oxidation of metals. 1-1) Shows the delivery of oxygen molecules to the surface. 1-2) the incorporation of Oxygen molecules to the oxide scale. 1-3) shows the delivery of metallic atoms to the scale interface. 1-4) the incorporation of metallic atoms to the scale. 1-5) diffusion of oxygen and metallic atoms inside the oxide scale.

To measure the oxidation reaction rate (how fast the oxidation occurs), one can write the oxidation reaction as follows:

$$\frac{x}{y}M + \frac{1}{2}O_2 = \frac{1}{y}M_xO_y \text{ (1.2)}$$

Kinetic rate law can be derived based on the above formula:

$$\frac{d\varepsilon}{dt} = f(t) \text{ (1.3.)}$$

With ε being a measure for the amount of reaction at the time t. therefore, it is possible to write that:

$$d\varepsilon = dn_{MxOy} = -\frac{dn_m}{x} = -\frac{dn_{O_2}}{y} \text{ (1.4)}$$

As a result, several methods can be devised to calculate the amount of progress in a reaction. The standard experimental methods are either measuring the consumption of oxygen or measuring the amount of oxide formation through mass change via a precise scale [34, 37]

Rates of oxidation reactions are usually controlled by two types of kinetics: linear and parabolic kinetics. Linear kinetics typically happens at very high temperatures or in atmospheres with low oxygen content (low oxygen partial pressure). In such cases, the

diffusion of the oxygen and the metal atoms inside the scale is so fast that they do not control the reaction rate. One can formulate the rate constant in this kinetic via [35-37]:

$$\frac{dx}{dt} = K_l\ ,\ X = \ K_l t \text{ (1.5)}$$

Here K_l is the linear rate constant.

The second type of kinetics that is more common in intermediate temperatures is parabolic kinetics due to the diffusional processes controlling the reaction rate. To be more specific, as the diffusion rate of metals and oxygen is the slowest step of the oxidation reaction, the parabolic behavior of diffusional phenomena controls the reaction. This can be formulated as follows:

$$\frac{dx}{dt} = \frac{k_p}{x},\ x^2 = 2k_p t \text{ (1.6)}$$

With K_p being the parabolic rate constant [35-37].

Effect of mechanical stresses in oxidation of metallic alloys

Mechanical stresses are one of the main factors in defining the stability of the oxide scale and its ability to protect the alloy from oxidation. More specifically, if no external source of force is applied to the alloy, the compressive force existing in the oxide scale will be balanced with the tensile force in the alloy. However, if this balance is removed and the stresses pass the critical value of ultimate tensile or compression strength, the oxide will fail mechanically which can result in deformation and/or fracture of scale, causing further damage to the alloy [38].

The source of stresses forming in the oxidation process can be divided into two main categories: a) stresses that form due to an increase in the temperature and b) the stresses that form due to the formation of the oxide. In particular, as the volume of the oxide phase is different from the parent alloy and since the alloy is constrained geometrically, this volume change results in stresses that can cause failure in the oxide scale [39].To quantify the sources of the stresses, the Pilling-Bedworth (PB) factor was devised as the ratio of oxide phase volume to the alloy volume [40, 41]

$$P - B\ factor = \frac{V_{oxide}}{n.V_{metal}} = \frac{M_{oxide}\cdot\rho_{oxide}}{n.M_{metal}\cdot\rho_{metal}} \text{ (1.7)}$$

Here, the V stands for the molar volume of the oxide of the metal, M is the atomic mass, ρ is the density, and n is the number of metal atoms for each molecule of oxide.

In the cases where the P-B factor is less than one, tensile stress will form in the oxide scale, resulting in the discontinuous formation of oxides such as those forming from alkaline metals [34]. On the other hand, when the P-B factor is above one, the oxide scale will experience compression due to the expansion of the oxide. Although compression is a desirable state for the oxide scale, it is not a guarantee for the protection of the alloy. For example, in alloys where the stress formed in the oxide scale is larger than the yield stress of the oxide material, plastic deformation occurs. However, as most of the oxide compounds are not ductile materials, the stresses may pass the ultimate tensile or compressive strength of the compound, resulting in mechanical failure of the scale. The mechanical failure can show itself as either a crack forming on the scale or, in more severe cases, spallation of oxide from the surface [42]. In both cases, these damages cause exposure of more alloy to the atmosphere, further damaging the alloy.

Selective oxidation

As with any type of chemical reaction, oxidation follows the rules of thermodynamics. Therefore, in the case of an alloy that constitutes several elements, the element that forms a more stable oxide compound will be preferred for oxidation reaction compared to the other elements. This preferential oxidation is the basis for oxidation protection of metallic alloys [34, 35]. To be more specific, by the addition of elements that can form thin, compact, and stable oxide compounds on the surface, one can improve the oxidation resistance of alloys significantly. This is the basis of oxidation protection in alloys such as CoCr-based and Ni-based alloys, where a compact oxide of Cr_2O_3 and Al_2O_3 provides significant protection [43, 44]

Internal oxidation

Internal oxidation of elements can happen when oxygen atoms can diffuse inward to the alloy while the metallic atoms have insignificant diffusion compared to oxygen. Therefore, oxygen atoms can penetrate inside the alloy, and if the oxide of one of the elements of the alloy is highly stable compared to the others, this element oxidizes inside the material, leaving a precipitate of oxide within the alloy. This phenomenon is known as internal oxidation and is considered to have a detrimental effect on the oxidation protection of metals [45].

To alleviate this problem, several measures can be taken. One is the composition modification of the alloy in a way that the oxide layer on the surface decreases the inward oxygen diffusion. As a result, the critical oxygen content necessary for oxidation reaction

(partial pressure of the oxygen) will not be available. Therefore, oxidation is thermodynamically prevented. The second method is forming a dense but thin oxide layer of the same alloy in a controlled atmosphere. This way, although the composition remained the same, due to the kinetics of the oxygen diffusion, the internal oxidation will not occur [34, 46]

Volatilization of metallic alloys

In some metals, oxide compounds that form during oxidation reactions are not stable at the reaction's temperature (or pressure); thus, they volatilize and leave the oxide scale. Examples of these oxides are Mo, V, and W, which can evaporate after a critical temperature. The extent of the damage caused by volatilization is very high, usually resulting in the destruction of the scale and powderization of alloys [34, 47, 48]

1.4 Atomistic Simulations

Since the introduction of computers to scientific society, computer simulations have found their place quickly as they provide a significant tool to solve problems that were impossible to solve by experimental or analytical methods. These scientific problems, according to their nature, can be divided into different scales, macro-scale or micro-scale problems, and various methods have been developed according to their scale. For example, computational simulations using the finite element method or computational fluid dynamics were created to solve problems of macro scales, such as stress distribution in an industrial component or airflow on an aircraft wing [49]. On the other hand, atomistic simulations were created to answer the need to solve problems stemming from atomistic scale phenomena. As an example of such simulations, one of the first computer simulations was performed to simulate a nuclear detonation reaction using atomistic simulations [50].

To better understand atomistic simulations, dividing them based on their computational techniques is beneficial as shown in Figure 1.3. Ab initio or first-principle methods calculate the properties of materials by solving quantum mechanics equations. Although these methods have the great advantage of being accurate in predicting different properties of materials, they are incredibly costly in terms of computational resources. The second group is the empirical force field (FF) methods that use interatomic potentials developed based on ab initio or experimental data. Within the methods that use empirical force fields, molecular dynamics (MD) and the Monte Carlo (MC) simulations bear great importance due to their many applications in the materials science field.

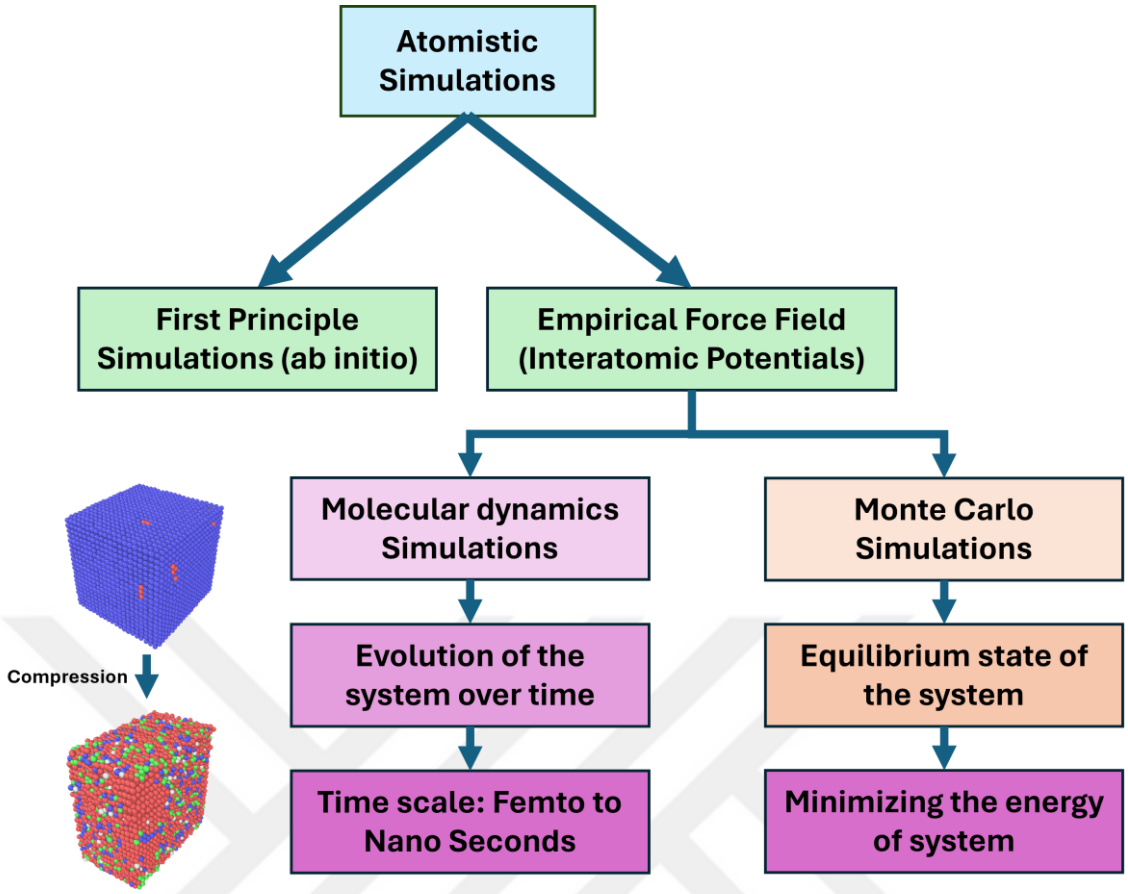

Figure 1.3 Schematic of different categories of atomistic simulations.

Molecular dynamics (MD) simulations

Molecular dynamics simulations use the force fields (interatomic potentials) created for a material to solve Newtonian physics of motions on the atoms of a system during a specific period. The MD simulations can capture a system's evolution under different conditions, such as mechanical loading, vibration, or heating. Therefore, many problems can be projected under these conditions, and the dynamic response of the materials can be captured during these simulations [51].

Although MD simulations can solve many problems with less computational cost compared to ab initio simulations, they have their own limitations and downsides. The two main limitations of MD simulations are the time scale and the computational cost arising from large system sizes [52].

Time scale problem in MD simulations

As mentioned previously, MD simulations solve the Newtonian movement of atoms for a specific time. More specifically, the MD simulations' time scale is in the order of several

femtoseconds (10-15 seconds) to several nanoseconds (10^{-9} seconds), depending on the computational resources. Considering this timescale, this method cannot study many phenomena that occur over a longer time. For example, any phenomena that include diffusional movements of atoms in solids, such as diffusion of metallic elements in alloys, are extremely hard to study using classical MD methods. Thus, alternative solutions should be considered in such cases [51, 52].

Monte-Carlo simulations can be utilized to alleviate the issue of time scales in MD simulations for some systems. The simplistic explanation of this method would be that the global minimum for the system's energy (state of the system) is searched via a systematic approach. Specifically, interatomic potentials can provide information on the state of the energies in the systems. Then, a change is made to the system, and the new value of the energy is measured. If the energy is lower than the previous energy, the change is approved, and the system evolves to a lower energy state (more stable). However, if the energy is not lower than the previous state, a criterion is considered to accept or reject the move. This criterion is created to help the system move out of the possible local minimums of energy it might face. Subsequently, in an ideal case, we reach a position where the system's state no longer changes, and the global minimum of the energies is found [51, 53].

System size problem in MD simulations

To gain an accurate understanding of a physical phenomenon such as dislocation movement, thermal conductivity, and phonon movement, a certain number of atoms are necessary in a simulation system. This number of atoms can range from a couple of thousands of atoms to millions of them. Therefore, in simulations of problems that a high number of atoms is needed, computational cost can be extremely high, demanding supercomputers and high parallel computation methods to be used [54, 55].

With this problem limiting the use of MD simulations, a Large-scale Atomic/Molecular Massively Parallel Simulator (LAMMPS) was developed in the 1990s and was released as an open-source code in 2004 to facilitate simulations that need classical MD simulations [56]. Using this code, various properties such as mechanical, phononic, and surface reactions such as adsorption can be simulated. In addition, Monte-Carlo

simulations have been recently integrated into this code to allow the simulation of systems that need longer time scales. The significant advantage of LAMMPS is its ability to run highly parallel simulations and, as a result, reduce the computation time on multi-core systems, opening the route to run MD simulations on dedicated workstations and super computers.

Considerations while using MD and MC simulations

Although the MD and MC simulations have opened a new door to explore the world of materials science, these methods have two noticeable constraints. To be more specific, the need to develop a new interatomic potential for each pair of elements in the simulation is highly limiting, as developing such potentials demands a significant amount of computational work by using first principle calculations and then fitting the values to the experimental reference results. The second limiting factor is the projection of the atomistic results to macro-scale physics. In particular, if the input for the MD simulations is not correctly chosen, it can produce misleading and inaccurate results that seem correct. In other words, “Garbage in – garbage out.” Therefore, it is essential to know the physics of the problems and the correct application of MD and MC methods to the systems. More importantly, deducing information from the atomistic simulations needs consideration of both the time scale and size of the phenomena happening in the studied material.

Chapter 2:
Uncovering the surface property – oxidation mechanism relationships in refractory high entropy alloys

2.1 Introduction

In the last decade, high entropy alloys (HEAs), also known as multi-principal alloys, have been shown to exhibit superior mechanical properties such as high strength, wear resistance, and toughness that are perceived to be the result of the four core effects of lattice distortion, sluggish diffusion, high entropy, and cocktail effects [57, 58]. Among the HEAs, refractory high entropy alloys (RHEAs) that are mainly composed of refractory elements such as Nb, Mo, Ta, V, and W alloyed with other high-melting-point elements have shown great potential for both high- and low-temperature applications. In particular, due to their high-temperature stability and specific strength, these alloys show great potential for applications in aerospace, and especially jet engines [26, 59, 60]. On the other hand, RHEAs composed of non-toxic elements such as Ti, Ta, Nb, Hf and Zr exhibit good corrosion resistance and biocompatibility that can synergize with their room temperature ductility, impact toughness, and good wear resistance, making them good candidates for biomedical applications such as orthopedic implants [21, 22, 61].

Despite their attractive properties, RHEAs suffer from the lack of intrinsic oxidation resistance and are susceptible to catastrophic failure in case of exposure to an oxidative atmosphere at elevated temperatures [32, 62, 63]. The lack of intrinsic protection against oxidation causes two significant shortcomings for these alloys: for one, it limits their utility at elevated temperatures as parts made from these alloys would fail under thermomechanical stresses in air atmosphere. Secondly, in low-temperature applications, low oxidation resistance constrains the manufacturability of the parts made from RHEAs. Specifically, high-performance parts usually undergo a step of hot deformation, such as hot forging or hot rolling in their production, where providing a constant protective atmosphere might be either impractical or highly expensive [64]. Similar problems are also expected for additively manufactured RHEA parts [65, 66], further providing a motivation for improving the oxidation resistance of this class of alloys to fully exploit their potential at both high and low temperatures.

In conventional alloys, improving the oxidation resistance can be achieved by alloying with Al, Cr, or Si, also known as oxide formers, which form a protective dense Al_2O_3, Cr_2O_3, or SiO_2 layer on the surface. These oxide layers efficiently slow down

oxygen diffusion into the lower layers while allowing selective oxidation of the protective element to maintain the scale [34, 35]. A similar approach has been taken to improve the oxidation resistance of RHEAs in several studies, demonstrating the more complicated nature of the oxidation mechanisms in these alloys. Notably, as Al_2O_3 is one of the best oxide formers in terms of stability and protection, many studies aimed to improve the oxidation resistance of RHEAs by alloying them with Al [33, 67-71]. For example, Sheikh et al. showed that adding Al could enhance the oxidation resistance of RHEAs studied. However, they also pointed out the complicated nature of oxide scale formation in RHEAs that can either prevent the formation of protective oxide layers on the surface or cause significant deterioration of the RHEAs' mechanical properties owing to the formation of undesirable brittle intermetallic compounds [72, 73]. In another study, Waseem et al. demonstrated that, although Al provided protection against oxidation to some extent, volatilization of Mo as one of the constituent elements caused significant oxidation damage [74]. As these examples indicate, although alloying with a potent oxide former such as Al is necessary, forming a truly protective oxide layer is not possible without sufficient knowledge about the oxidation mechanism of the RHEAs. Therefore, an in-depth study of the surface and the oxide layer formation without the oxide formers is crucial to provide insight into developing oxidation-resistant RHEAs.

In the present study, a thorough experimental approach was undertaken to understand the RHEAs' oxidation and scale formation mechanisms in the absence of protective oxide-forming elements to shed light on the prerequisites of forming a protective oxide layer. In particular, four different polycrystalline RHEAs, namely HfNbTaTi, HfNbTaTiZr, HfMoTaTiZr, and NbMoTaTiZr were investigated via various characterization methods such as scanning electron microscopy (SEM), energy-dispersive X-ray spectroscopy (EDX), X-ray diffraction (XRD), and X-ray photoelectron spectroscopy (XPS) to understand the scale forming mechanisms in each of these alloys. As demonstrated by many studies from different scientific fields, the XPS method is a powerful tool to investigate the oxidation state of the species of elements on the outermost surfaces of samples, providing detailed information about the surface chemistry [75-77]. Therefore, in the present study, a detailed analysis of the XPS method was combined with Ar+ ion etching to gain a deeper understanding of the oxidation and scale-forming mechanisms within the surface layer of each sample. In addition, using the physical vapor deposition (PVD) method, an amorphous NbMoTaTiZr coating was produced to compare the oxidation response of an amorphous RHEA with its polycrystalline counterpart. The

results of this investigation showed that three different oxidation mechanisms prevail in the RHEAs studied: formation of a non-protective scale, powderization of the sample, and amorphous oxidation. In addition, Mo and Nb were observed to induce a detrimental effect on the oxidation behavior and integrity of the samples. Overall, the current findings provide important information about the oxidation mechanisms in RHEAs, which could aid developing novel oxidation-resistant RHEAs.

2.2 Experimental details

The HfNbTaTi (HEA1), HfNbTaTiZr (HEA2), HfMoTaTiZr (HEA3), and NbMoTaTiZr (HEA4) HEAs with the compositions shown in Table 2.1 were produced in form of disks via the vacuum arc remelting (VAR) method using elemental powders of 99.9% purity. In order to increase the homogeneity of the alloys, they were remelted and flipped five times during manufacturing in a Ti-gettered argon atmosphere. Subsequently, rectangular samples of 10 mm × 5 mm × 1 mm were extracted from the disks using electrical discharge machining (EDM). The samples underwent grinding using emery paper with grit sizes ranging from 240 to 2500 and were finally polished with 0.3 μm alumina slurry resulting in a mirror-like surface.

Table 2.1 Nominal chemical compositions of the RHEAs investigated

Alloy name	Atomic percentage (at.%)					
	Ti	Ta	Hf	Nb	Mo	Zr
HEA1	50	16.67	16.67	16.67	-	-
HEA2	20	20	20	20	-	20
HEA3	20	20	20	-	20	20
HEA4	20	20	-	20	20	20

In order to produce the amorphous NbMoTaTiZr alloy (HEA4C), a physical vapor deposition (PVD) target with the same composition as the HEA4 was manufactured (Kurt J. Lesker PA, USA). Specifically, a radio frequency (RF) magnetron sputtering device (NVTS-400, Nanovak Ar-Ge, Ankara, Turkey) was used for depositing the HEA4 on CoCrMo (27 wt.% Cr, 6 wt.% Mo and balance Co) substrates under Ar flow, while a base pressure of 10^{-7} torr was maintained during the coating procedure. The reason for choosing a CoCrMo substrate was its relatively high resistance to oxidation at the

intended test temperatures. Prior to applying the vacuum and performing the coating process, the chamber was purged with high-purity N_2. Afterwards, the PVD target was pre-sputtered for 5 minutes to remove the oxides and possible impurities while a shutter isolated the substrates. Subsequently, 150 watts of power was utilized for sputtering while ten standard cubic centimeters per minute of Ar flowed inside the chamber. The resulting thickness was measured via SEM, showing that about 600 nm of coating thickness was achieved for all the HEA4C samples.

For the static oxidation experiments, separate batches of samples (HEA1-4 and HEA4C) were put in a box furnace and were heated from room temperature to the target temperatures of 700 ℃, 800 ℃, and 900 ℃. Subsequently, they were held at their respective temperatures for one hour and then cooled in air. All subsequent analyses were carried out on the samples' top surfaces that were exposed to air. The phases present in the samples were analyzed with XRD employing a Bruker D8 Advanced X-ray diffractometer equipped with a Cu-K_α source. An incident angle range of 15° to 100° was used for samples HEA1-4 in Bragg-Brentano geometry. By contrast, grazing incident X-ray diffraction (GI-XRD) mode was used in the range of 20° to 100° for analyzing the HEA4C samples to improve the detection of peaks from the coated alloy. In order to enhance the signal-to-noise ratio for detection of minor peaks, all samples were oscillated one millimeter around the point of the incident in planar directions while the measurements were conducted. The DIFFRAC.EVA software and PDF-4+ 2022 database were used for the identification of the corresponding compounds.

To Investigate the surface morphology of the samples, a field emission scanning electron microscope (FE-SEM, Zeiss SUPRA 55VP) was employed, while the chemical composition of each sample was analyzed utilizing energy-dispersive X-ray spectroscopy (EDX, Bruker AXS GmbH). In order to examine the oxide species of the surface layer, X-ray photoelectron spectrometry (Thermo Scientific K-alpha) with a monochromatic Al – K_α X-ray source (1486.6 eV energy, 12kV voltage and spot size of 400 μm x 400 μm) was utilized. In order to gain insight into the oxide species of the lower layers and their chemical composition, depth profiling was performed within an area of 2 mm x 2 mm with the aid of an Ar^+ ion source operated at 10 nA and 1 kV at a 30° angle, resulting in estimated 0.2 nm/s sputtering rate (calibrated to a Ta_2O_5 standard sample). In order to maintain charge neutralization, a flood gun was also utilized. The software used for peak deconvolution and quantitative analysis of the XPS results was Thermo Scientific Avantage software (v. 5.949). The acquired results were normalized so that the carbon-

carbon bond was associated with a binding energy of 284.8 eV, and the SMART background was used for the peak deconvolution. The relative sensitivity factors of pure elements included in the Avantage software were utilized while calculating the atomic percentage of oxide states formed on the surface via the integrated intensities (area) of the deconvoluted peaks. Considering that HEA-3 and HEA-4 samples were powderized during the oxidation experiments and their surface oxide layers diminished, comparison of the results of their surface characterization with the other samples would have been misleading, and thus they were exempted from XPS and SEM analyses.

2.3 Results

The photographs acquired from the samples following the oxidation experiments are shown in Figure 2.1. These images indicate that the oxidation response of the alloys can be categorized into two groups based on the integrity of the scale formed on the surface after exposure to high-temperature oxidation. The first group comprises the alloys that maintained their surface integrity, namely HEA1, HEA2, and HEA4C, while the second group comprises the HEA3 and HEA4 samples, i.e., those where the scale spalled and the samples lost integrity. The effect of oxidation temperature on HEA1 samples can be seen in Figure 2.1a-c, which shows that at 700 °C (Figure 2.1a), the sample did not show noticeable damage from oxidation; however, as the temperature was raised to 800 °C (Figure 2.1b), minor cracks formed at the edge of the samples, causing slight spallation of scale around the edge. With a further increase of temperature to 900 °C (Figure 2.1c), a considerable part of the scale was spalled off, as shown in greater detail in Figure 2.2a (this region is referred to as the “descaled region” in the remainder of the article). A similar behavior was observed in the HEA2 samples (Figure 2.1d-f). However, in these samples, there is a noticeable change in the smoothness of the surface as compared to the HEA1, observed in the form of scale buckling. It is notable that in the sample oxidized at 900 °C (Figure 2.1f), a small segregation of the element Ta was detected by EDX (as in Figure 2.2d). After the oxidation experiment, this area appeared as a white and highly brittle segment of the sample. Such inhomogeneity (Figure 2.2c) is caused by the VAR process and is a known issue reported for other as-cast RHEAs [22, 26, 78]. In particular, due to the high melting points of RHEAs, even after several remelting cycles, some zones within the material cannot be thoroughly melted, leaving pure particles of high-melting-temperature elements unmixed. This part of the sample was avoided during characterization and scale analysis.

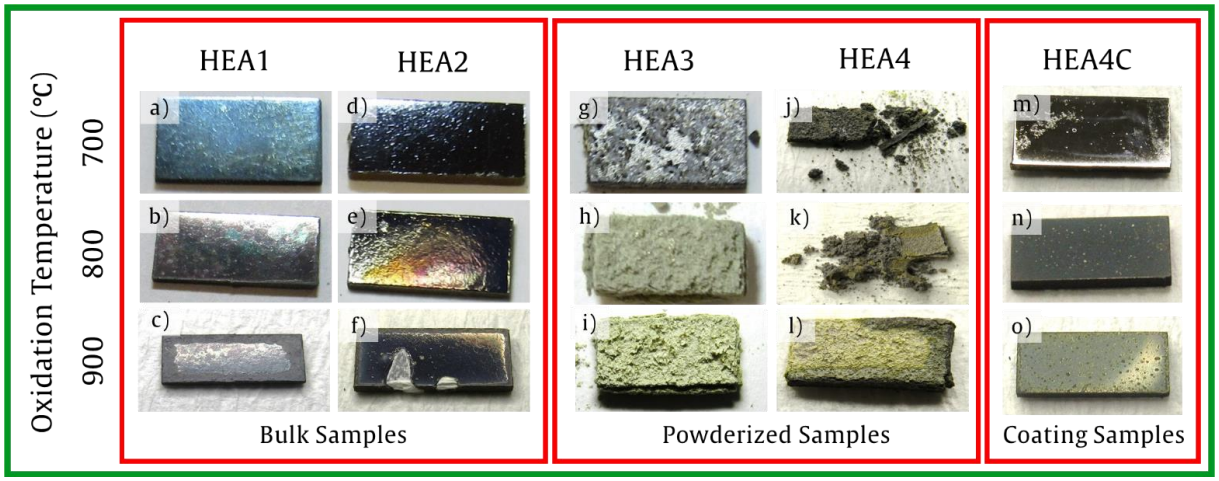

Figure 2.1. Photographs showing the state of the samples following the oxidation experiments

The HEA4C sample (Figure 2.1m-o) also showed similar surface integrity following oxidation as compared to HEA1 and HEA2. However, the edge effect was less noticeable in HEA4C, which could be associated with the curvature of the coated material on the edges creating less stress concentration as compared to the sharp edges of the EDM cut samples. The effect of temperature on these alloys is also significant. The sample oxidized at 700 °C maintained its metallic shine even after the oxidation; however, as the temperature increased to 800 °C, the metallic shine was lost, and spallation took place on small parts of the surface. In contrast to HEA1 and 2, these parts are uniformly distributed around the surface and not concentrated around the edge, indicating a potentially different oxidation mechanism (Figure 2.1n and Figure 2.1o).

The second group of alloys, the ones that lost their integrity, are shown in Figure 2.1g-i for HEA3 and Figure 2.1j-l for HEA4. As various properties of HEA2 have already been studied [14, 79], it would be worthwhile to compare HEA3 and HEA4 with HEA2 since these alloys are all equimolar quinary alloys with common Ti, Ta, and Zr elements. As compared to the HEA2, the Nb element was replaced with Mo in the HEA3 alloy, and these samples underwent catastrophic failure and were powderized. The effect of temperature is noticeable in these alloys: at 700 °C, the sample surface shows damage and spallation due to oxidation. However, the damage significantly increased as the temperature increased, and the whole surface was powderized. A further temperature increase did not cause significant additional damage.

As compared to HEA2, Hf was substituted with Mo in HEA4. This substitution resulted in more pronounced catastrophic damage of the sample at 700 °C and further powderization at 800 °C when compared to HEA3. Therefore, one can indicate the higher damage caused by presence of Nb as compared to that brought about by Hf, as evident from the comparison of HEA3 and HEA4. However, the HEA4 sample oxidized at 900 °C, although severely damaged, did not powderize completely, which might indicate a different oxidation mechanism. It should be noted that the HEA4 and HEA4C show entirely different behaviors, although they have similar compositions. Therefore, the effect of the polycrystalline microstructure with grain boundaries versus the amorphous state can be observed here.

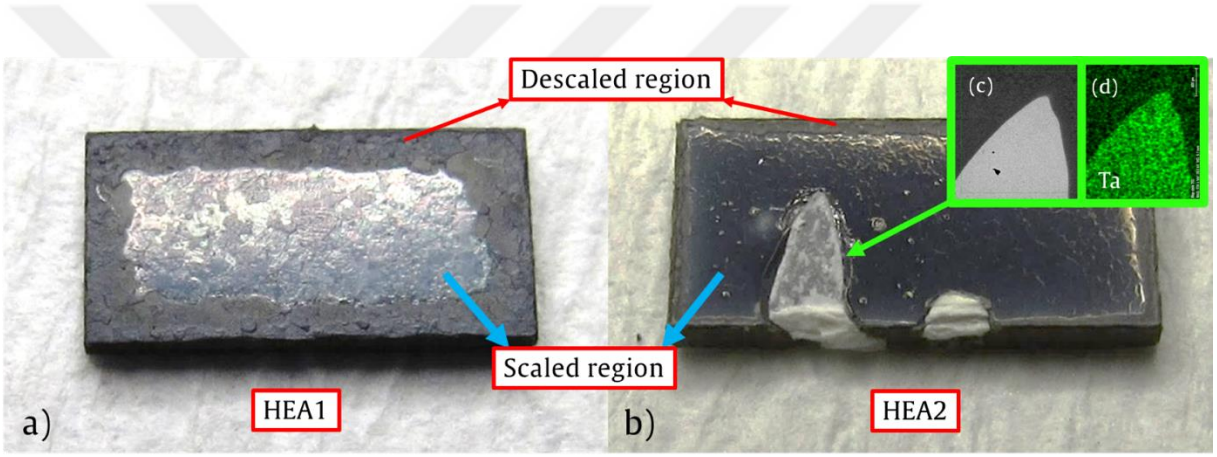

Figure 2.2. (a) HEA1 and (b) HEA2 samples that underwent oxidation at 900 °C, (c) backscattered electron micrograph of the Ta segregation area in the HEA2 sample, and (d) Ta segregation mapped with EDX

The secondary electron SEM micrographs of the scaled region from the HEA1 and HEA2 samples are presented in Figure 2.3, showing the morphology of the scales following oxidation at different temperatures. As presented in Figure 2.3a, HEA1 at 700 °C revealed no significant oxidation features. However, as the temperature increased to 800 °C, needle-like features, also referred to as “whiskers”, formed on the surface (Figure 2.3b). As the temperature rose to 900 °C, the whiskers grew in size (Figure 2.3c). In contrast to the HEA1, the HEA2 exhibited whisker formation already at 700 °C, and these whiskers grew further at 800 °C. As the temperature increased to 900 °C (Figure 2.3f), the entire surface of the sample was covered with whiskers. Two distinct differences between HEA1 and HEA2 are prevalent: firstly, the shape of the whiskers in HEA1 is

prismatic, while the HEA2 features cylindrical whiskers, indicating a difference between their chemical compositions [80, 81]. The second difference is that the HEA1 surface looks rigid in a way as the formed whiskers are linked, covering the surface thoroughly, while the HEA2 surface exhibits many pores that can facilitate the oxidation process.

Figure 2.4 presents the microstructure of the descaled region in the HEA1 and HEA2 samples that underwent oxidation at 900 °C. This region represents the composition and microstructure of the lower layers of the scaled region. As shown in Figure 2.4a, the HEA1 sample has a dense microstructure with crystallites filling the surface. On the other hand, the HEA2 possesses a microstructure with many voids. Although one could argue that these voids formed due to the formation of volatile oxide species, such a claim would not be reasonable for HEA2, as no known oxide compound of HEA2 volatilizes at the temperatures used in the experiments. In addition, in the case of volatilization, the surface should have shown a sign of evaporation or sublimation, such as partial scale loss across the surface and not only the edges, which was not observed in HEA2. Thus, these voids are potentially formed due to the Kirkendall effect rooted in unequal diffusion of elements to the scale versus the bulk of the sample [34, 82, 83].

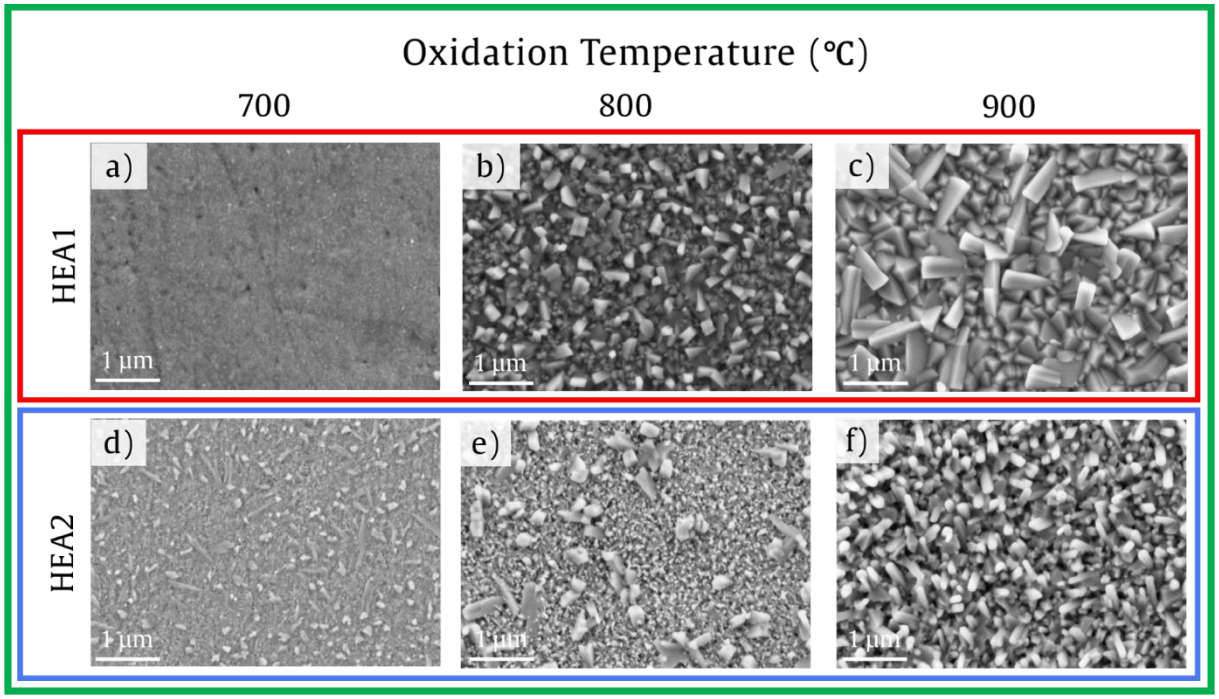

Figure 2.3. Secondary electron SEM micrographs of the scaled regions from the surface of HEA1 samples that underwent oxidation at (a) 700 °C, (b) 800 °C, and (c) 900 °C; a similar region in HEA2 samples oxidized at temperatures 700 °C, 800 °C, and 900 °C for

(d), (e), and (f), respectively

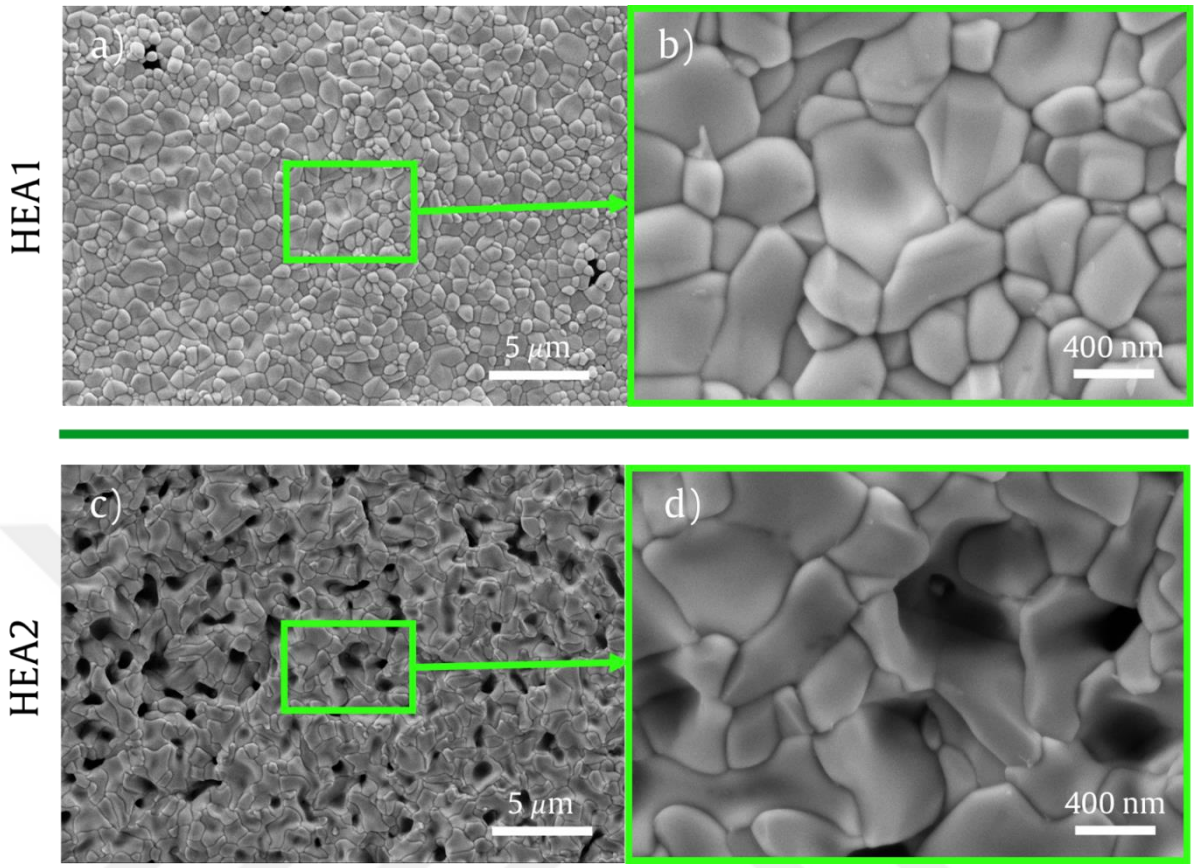

Figure 2.4. Secondary electron SEM micrographs taken from the descaled region of HEA1 (a and b) and HEA2 (c and d) samples that underwent oxidation at 900 °C

Figure 2.5 presents the distribution of elements in both scaled and descaled regions for HEA1 and HEA2 obtained by EDX mapping. Accordingly, the Ti content is higher in the scaled region, while Ta and Hf concentrations are higher in the descaled region (Figure 2.5a). Considering that the descaled region was below the scaled region before spallation, the relative composition of lower layers of the scale can be inferred from this region. This is possible owing to the short duration of the experiments, limiting the amount of the compositional change via diffusion or oxidation (the difference between microstructures shown in Figure 2.3 and 2.4 support this idea). The higher content of Ti in the scaled region as compared to the descaled one evidences the migration and diffusion of Ti atoms towards the surface to participate in the oxidation reaction. Although Ti does not have the lowest oxide formation energy as compared to the other elements in the HEA1 composition, the relatively smaller size of Ti atoms facilitates diffusion while other elements such as Hf and Ta oxidize internally [84, 85]. For HEA2, on the other hand, the

Ti concentration is higher in the descaled region, while other elements are distributed almost equally across both regions (Figure 2.5b), which can be associated with the sluggish diffusion effect, decreasing the mobility of the Ti atoms. Another possible reason for the mitigation of Ti from the scaled regions is that the compounds that were thermodynamically more favored for oxidation repelled the Ti from the scale due to the lower limit for dissolving Ti. The lower dissolution limit affects the chemical potential difference needed for the migration of atoms, therefore reducing the Ti content on the surface [34, 35].

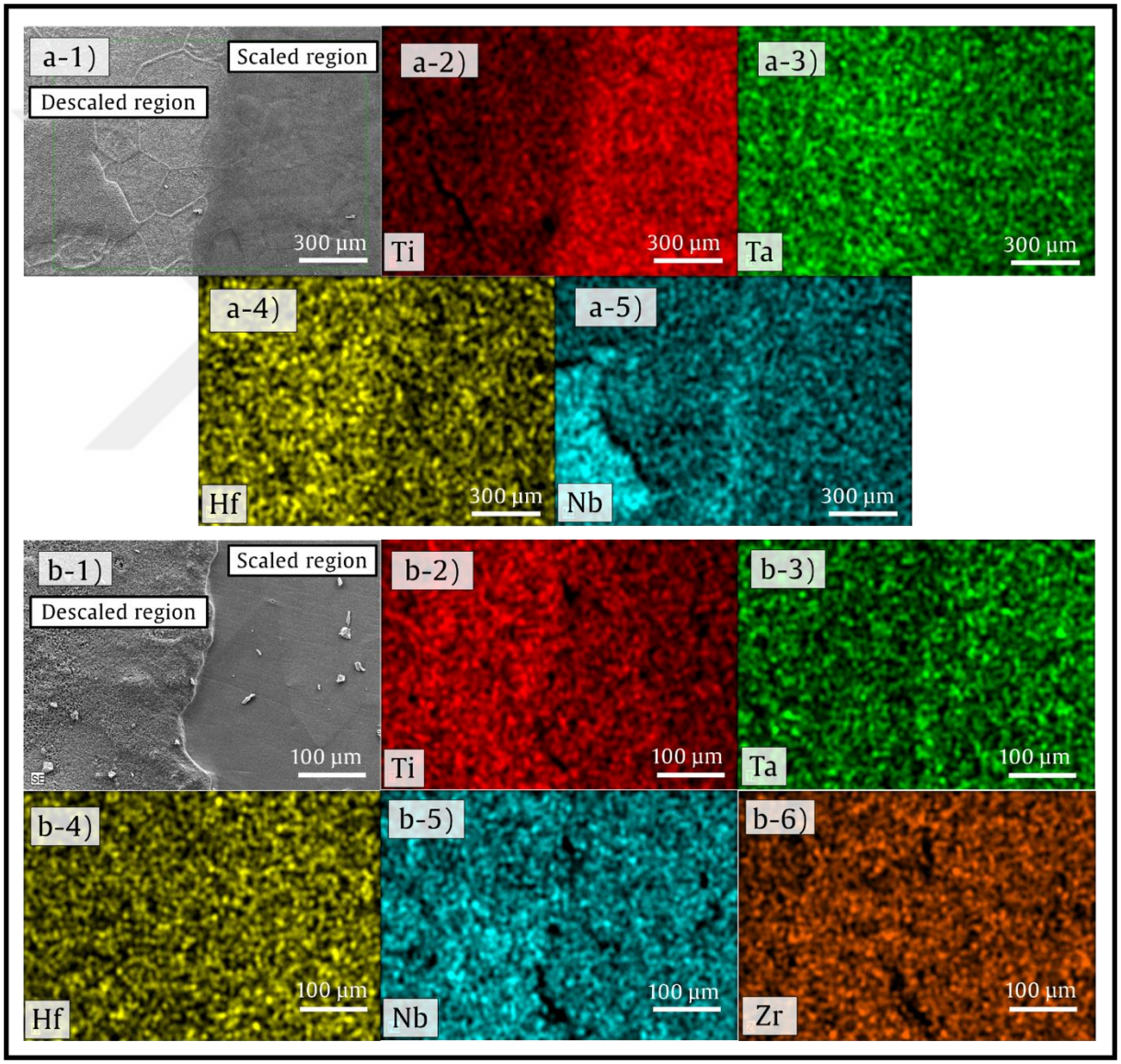

Figure 2.5. a) EDX mappings of scaled and descaled regions of HEA1 oxidized at 900 °C, b) EDX mapping of scaled and descaled regions of HEA2 oxidized at 900 °C

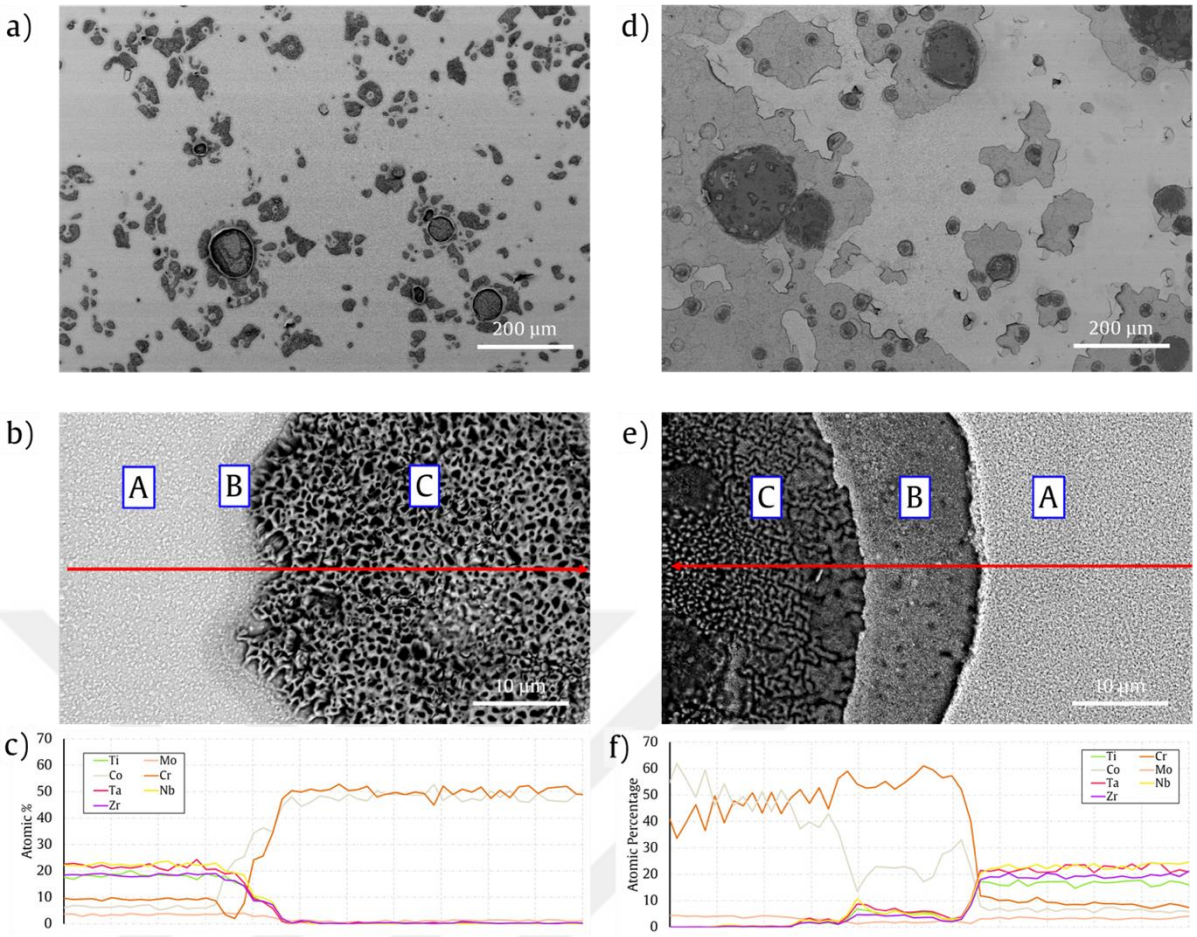

Figure 2.6. a) Backscattered electron SEM micrograph of HEA4C sample oxidized at 800 °C, b) higher magnification detail of one of the features appearing on the HEA4C sample following oxidation, and c) elemental composition acquired from line scan EDX measured along the redline shown in (b); (d), (e) and (f) similar data as a)-c) obtained from the HEA4C sample oxidized at 900 °C

Figure 2.6 shows the surface of HEA4C samples after oxidation. As can be seen in Figure 2.6a, after oxidation at 800 °C, the sample exhibited island-like damaged areas on its surface. A closer look at these areas (Figure 2.6b) shows the presence of three distinct regions: region A is an oxidized area of the sample without noticeable damage. Region C is where the coating was completely lost and a highly porous surface remained, and region B constitutes a transition zone between regions A and B. Figure 6c presents an EDX line scan from the red line indicated in Figure 2.6b, demonstrating that region C was completely depleted from the coating, and only Cr and Co signals were received from the substrate. Therefore, it can be inferred that the spallation of the coating, instead of occurring uniformly, initiated at these specific points, and then spread throughout the

surface. This is also indicated by the transformation of region A to region C. Overall, as the temperature increased to 900 °C, smaller areas of region A were observed, region B was predominant. In addition, region B was more prevalent at 900 °C (Figure 2.6e) than it was at 800 °C (Figure 2.6b), and had more pronounced borders at 900 °C. This can be attributed to the sideway diffusion of oxygen to the lower layers of scales through the already damaged scale, while the oxygen diffusion from the top surface causes partial scale detachment.

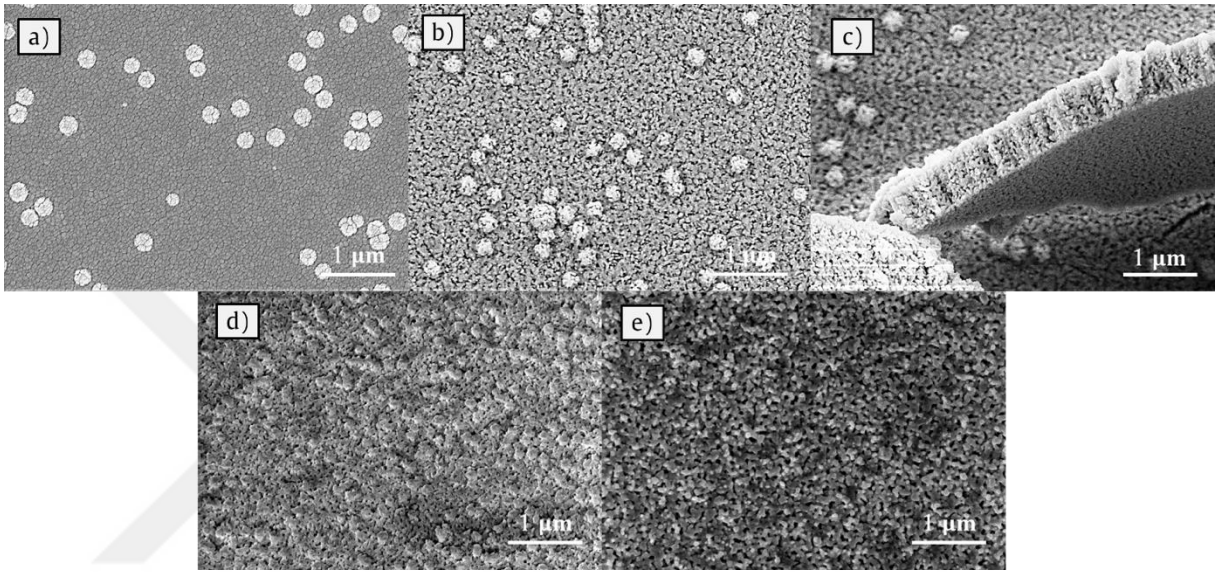

Figure 2.7. Secondary electron SEM images of a) the as-coated HEA4C, b) the HEA4C sample oxidized at 700 °C, c) the cross-section of the sample oxidized at 700 °C, d) the HEA4C sample oxidized at 800 °C, and e) the HEA4C sample oxidized at 900 °C

Figure 7a shows the HEA4C sample in the as-coated form shortly after PVD coating, demonstrating that the HEA4 coating features an amorphous morphology similar to the previously reported amorphous RHEAs [86, 87] . Apparently, following the coating process, globular features are spontaneously formed on the surface of this sample. Point EDX measurements were performed on these features; however, considering the small size of the features as compared to the larger depth of signal collection when using EDX, no significant compositional differences were observed. However, it is speculated that these features are air-formed oxides forming upon coating, similar to what Hruska et al. reported in HfNbTaTiZr coatings [88]. Subsequently, the samples were oxidized and the corresponding SEM micrographs are presented in Figure 2.7b-e, which were taken from region A of Figure 2.6 at higher magnification. The first observation is the prevalence of

pores on the surface (Figure 2.7b), further extending throughout the coating (Figure 2.7c). As the temperature increased to 800 °C, the globular features disappeared from the surface, and the further temperature increase to 900 °C caused the pores to grow further, decreasing the thickness of the remaining material. These figures suggest the different oxidation mechanism active in the HEA4C samples that are subject to the volatilization of Mo.

Extensive XPS analysis was carried out in order to understand the chemistry and the oxidation state of the oxide scales in the RHEA samples. Figure 8 presents the XPS spectra of the constituent elements of the HEA1 sample, which indicate that Ta_2O_5, HfO_2, Nb_2O_5, and TiO_2 are the most common oxide species on the surface of this sample. However, considering the compositional complexity of RHEAs and the complex compounds that are possible to form due to oxidation, assigning the acquired spectra to such simple compounds without additional information might be misleading. Specifically, there can be complex oxides (for example ABO_4, where A and B are two metallic elements with oxidation state of +4) such that each element possesses similar oxidation states as the simpler compounds (for example AO_2 and BO_2 that both have +4 oxidation state). These oxidation states results in a similar XPS spectrum. A similar consideration should be taken into account while analyzing the data acquired from HEA2 and HEA4C presented in Figure 2.9 and Figure 2.10. Considering this, Figures. 2.8-2.10 suggest a similar condition in the Hf, Nb, Ta, Ti, and Zr spectra, indicating the formation of high valence oxides on the surface. Moreover, the results show that some elements also form lower valence oxides at lower temperatures.

Particular caution should be taken in the analysis of Mo Spectra shown in Figure 2.10 a1, b1, and c1. Peak analysis of Mo compounds is an intricate process, as the literature on the MoO_3 and MoO_2 compounds has proven that XPS spectra of MoO_2 have two different doublets, representing the screened and unscreened signals [89]. In addition to the complications arising from the nature of Mo oxides, one of the Ta 4d doublets overlaps with the Mo spectrum range due to the existence of Ta in the present samples. Such peaks of inner orbitals are usually broader (higher full-width half maximum (FWHM)), and the chemical shift between the doublets is also much larger. As a result, the second doublet of Ta 4d is not visible in the current Mo spectra [90]. Considering these factors in analyzing and peak fitting of Mo oxidation states, the present results showed that temperature significantly affects the oxidation state of Mo compounds. As shown in Figure 2.10 a1 and Figure 2.10 b1, one can detect both Mo^{+4} (screened and

unscreened) and Mo^{+6} peaks. However, as the temperature increased to 900 °C, the peak intensity of Mo^{+4} (screened) and Mo^{+6} decreased significantly. This change is associated with the fact that MoO_3 is a volatile compound and evaporates around 830 °C [91]; thus, it was lost from the surface of the samples. The unscreened peaks of Mo that still exist represent the remnants of Mo on the surface.

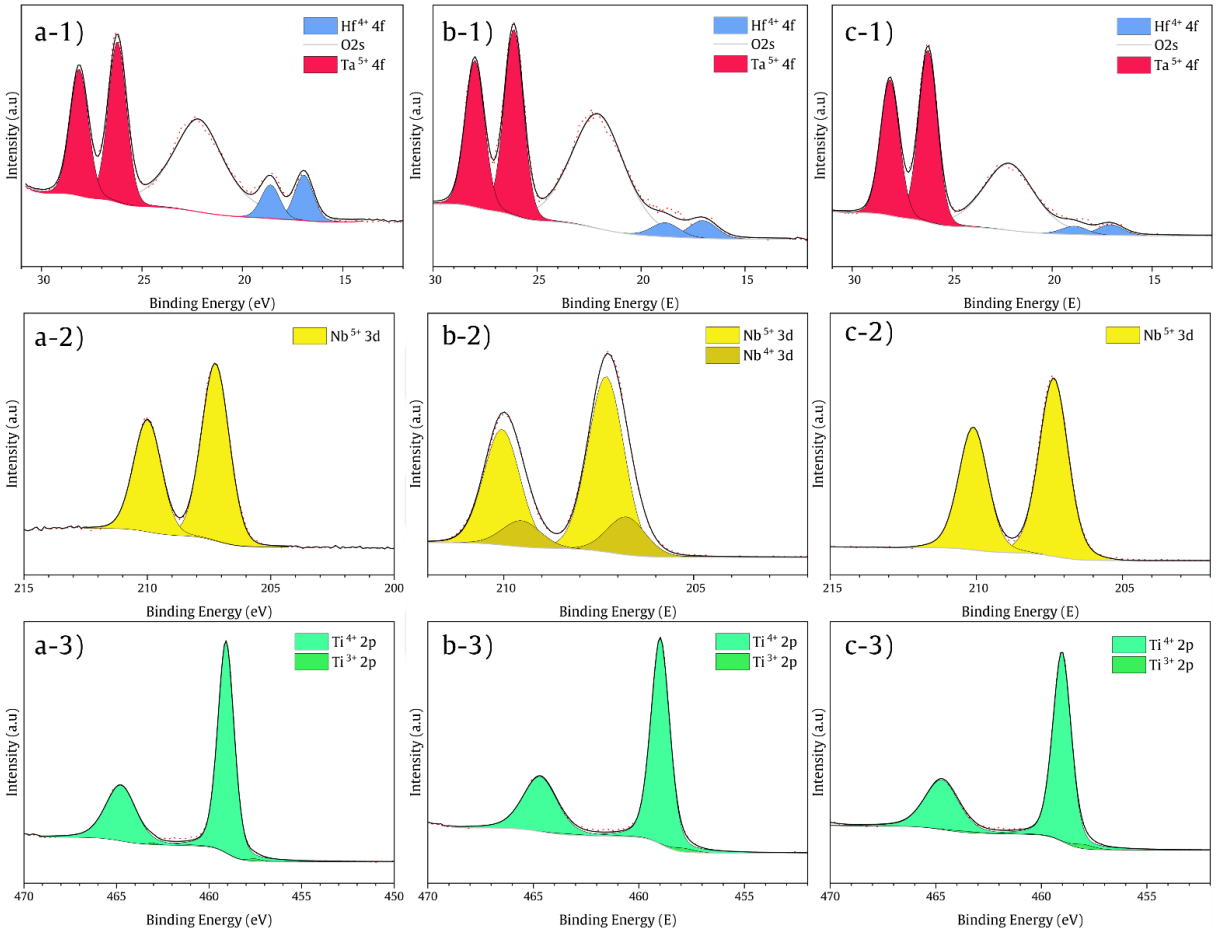

Figure 2.8. XPS spectra of (1) Hf and Ta, (2) Nb, and (3) Ti acquired from the surface of the HEA1 samples oxidized at a) 700 °C, b) 800 °C, and c) 900 °C.

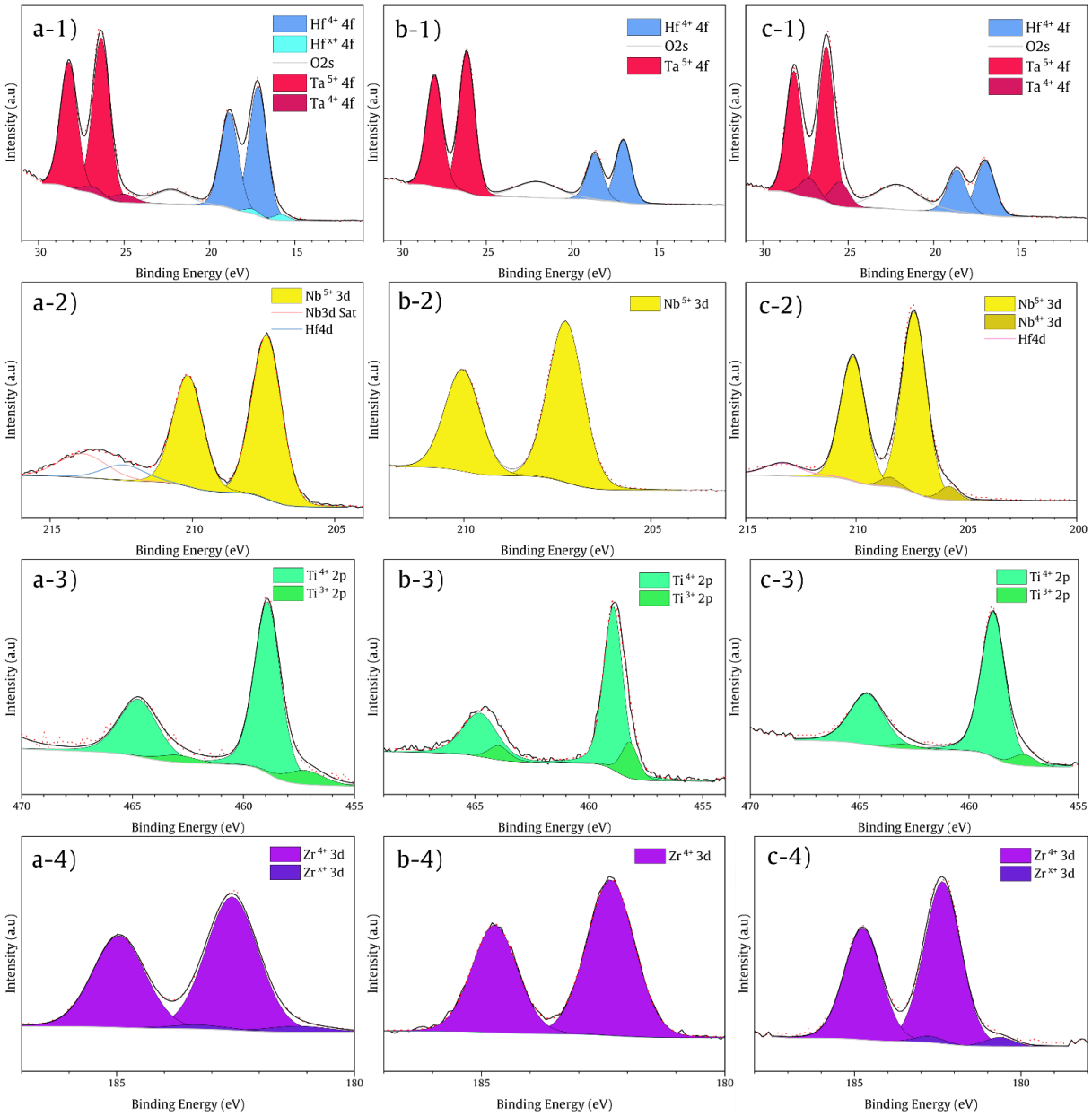

Figure 2.9. XPS spectra of (1) Hf and Ta, (2) Nb, (3) Ti, and (4) Zr acquired from the surfaces of the HEA2 samples oxidized at a) 700 °C, b) 800 °C, and c) 900 °C

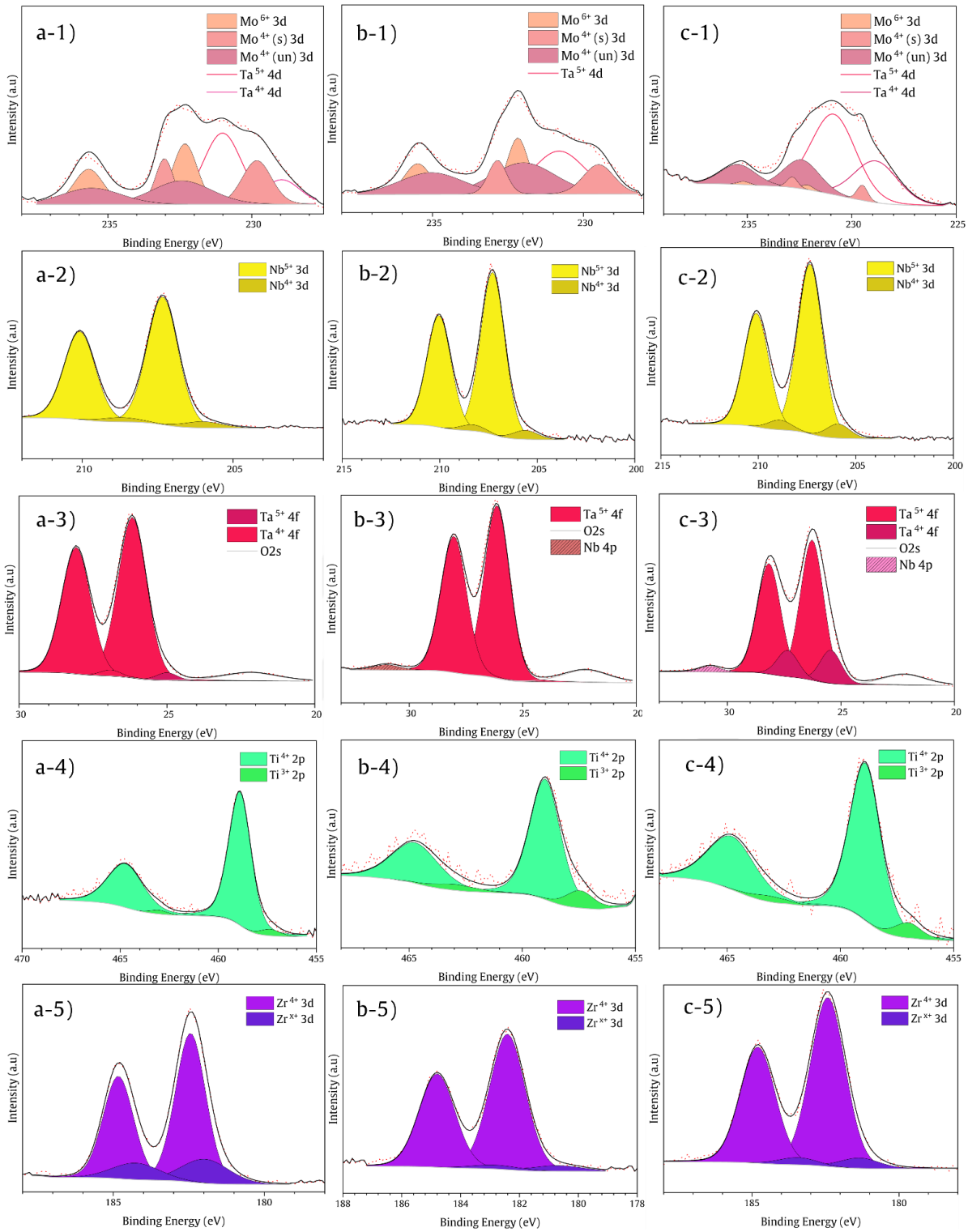

Figure 2.10. XPS spectra of (1) Mo, (2) Nb, (3) Ta, (4) Ti, and (5) Zr acquired from the surfaces of the HEA4C samples oxidized at a) 700 °C, b) 800 °C, and c) 900 °C

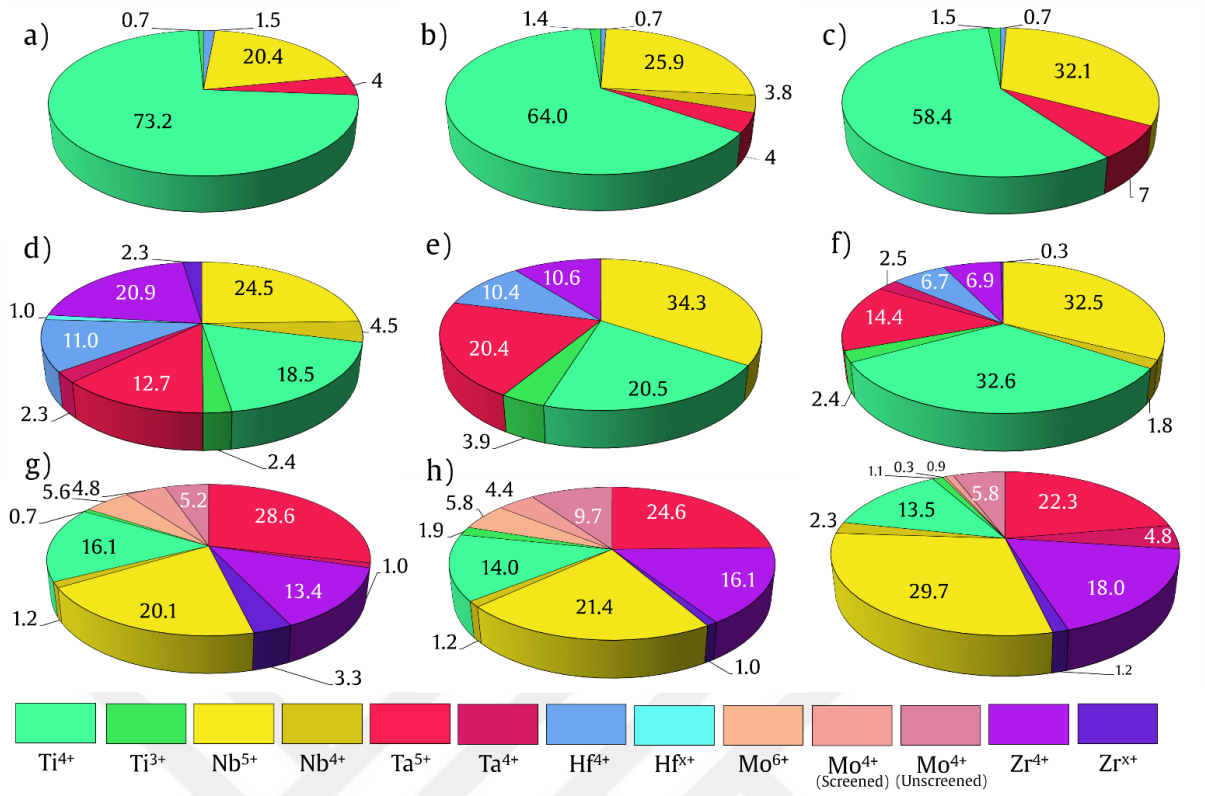

Figure 2.11. Distribution of different oxidation states on the surface of HEA1 oxidized at a) 700 °C, b) 800 °C, and c) 900 °C; (d-f) and (g-i) show similar information for the HEA2 and HEA4C samples, respectively

Figure 2.11 presents the distribution of different oxide states on HEA1, HEA2, and HEA4C surfaces oxidized at different temperatures. As shown in Figure 2.11a, the HEA1 sample oxidized at 700 °C is mainly composed of Ti^{4+} and Nb^{5+} with contents higher than the as-cast (50 at.% Ti and 16.6 at.% Nb). In contrast, a minimal amount of Hf is seen, which can be attributed to the internal oxidation of the Hf that prevents the transfer of Hf atoms to the surface. As temperature increased from 700 °C to 900 °C, a decrease in the Ti content of the surface becomes obvious while the Nb content increased (Fig 11b and Figure 2.11c). These results hint at two outcomes: for one, since the depth of measurement using the XPS method is less than 10 nm, considering the SEM results shown in Figure 2.3, it is possible to assign whiskers formed on the surface to oxide compounds with a significant amount of Nb. Secondly, considering the deterioration of the oxide layer on the surface of HEA1 as temperature increased and the simultaneous decrease in the Ti content, one can attribute the better oxidation resistance of HEA1 at 700 °C to the high Ti^{4+} content of the surface, forming a more uniform and protective oxide layer. Concurrently, the higher Nb content of the surface deteriorated the oxide

layer.

Figure 2.11d shows the surface composition of HEA2 oxidized at 700 °C. Similar to HEA1, Nb is one of the prevalent elements on the surface; however, HEA2 shows a more variable surface, and the compositions of the constituent elements are closer to their as-cast states. As the temperature increased to 900 °C, Nb and Ti dominated the surface, and the content of Hf and Zr decreased notably [92, 93]. It can be deduced that the higher affinity of Nb and Ti to oxygen provided the necessary chemical potential for the diffusion of these elements to the outermost surface, while their mobility facilitated the movement of atoms from layers below the surface. Similar to HEA1, the lower content of Hf and Zr is attributed to the internal oxidation of these elements. It should be noted that the difference between the amount of Ti measured by the EDX and XPS methods is due to the depth from which the data are acquired. The XPS method provides information from a thin layer of material (about 10 nm), while the EDX results presented in Figure 2.5 are in the order of a few micrometers.

The surface composition of HEA4C is presented in Figure 2.11g-h. Previous studies on Mo oxidation suggest that between 550 °C and 700 °C, an oxide scale of Mo can form simultaneously with the volatile MoO_3. However, for temperatures higher than 800 °C, MoO_3 volatilizes as soon as MoO_3 forms, and beyond 900 °C, the volatilization is fast enough, such that the controlling reaction of the process is the diffusion of oxygen atoms [91]. Therefore, it is expected to have a higher percentage of all Mo species on the surface as the temperature increases from 700 °C to 800 °C, which was also the case for the current samples. This increase is due to the oxide formation reaction and the volatilization occurring on the surface, and thus a build-up of MoO_3 is expected. As the temperature increased to 900 °C, MoO_3 evaporated faster from the sample due to higher reaction rates. Consequently, the overall content of Mo on the surface decreased. Similar behavior has been previously observed in other alloys containing Mo [94]. On the other hand, for the other constituent elements of the HEA4C sample, there was no significant change when the temperature increased from 700 °C to 800 °C. The percentage change associated with the temperature increase from 800 °C to 900 °C was roughly equal to the change resulting from the loss of Mo, enhancing the atomic percentage of other elements. The relatively less significant change in the compositions of the HEA4C sample could be attributed to the oxidized amorphous microstructure with a lower density but with many pores, hindering significant diffusion of atoms.

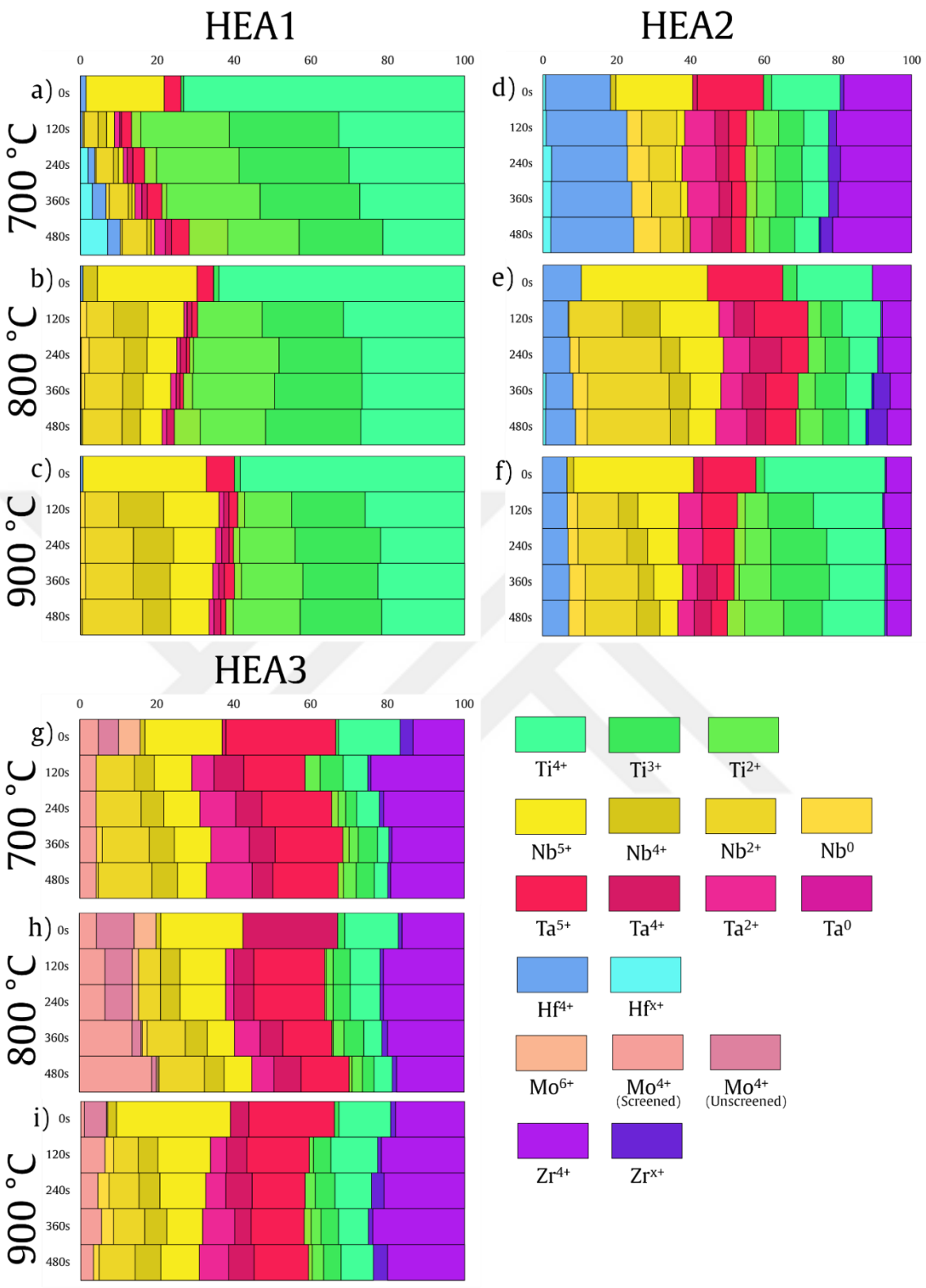

Figure 2.12. Distribution of different oxidation states in HEA1 samples oxidized at a) 700 °C, b) 800 °C, and c) 900 °C, as obtained upon employing various Ar^+ ion etching durations, (d-f) and (g-i) show similar results for HEA2 and HEA4C, respectively; the 0s ion etching represents the unetched surface of the samples, and the 480s represents the

deepest layer that XPS measurement was taken from, corresponding to about 100 nm

Figure 12 illustrates the distributions of oxidation states in the HEA1, HEA2, and HEA4C samples oxidized at different oxidation temperatures for various depths of measurements. The Ar^+ ion etching depth was calibrated based on the Ta_2O_5 reference and is estimated as 100 nm for 480 seconds duration of ion etching. However, this is not an exact depth value as the material parameters can significantly affect the etching rate, resulting in different values for different samples within each etching interval. In addition, the sample surfaces exhibit higher valence oxidation states, while lower layers have species with a variety of states. These states can both represent the formation of suboxide in these samples and indicate the formation of complex oxides with lower oxidation states.

Considering these points, several trends for each element are seen: the amount of Hf species in both HEA1 and HEA2 is inversely correlated with temperature, and as temperature increased, the overall amount of Hf in the layers decreased [93]. Because the depth of the measured layers is about 100 nm, one can assume that the measured volume is from the oxide grown on the surface and not affected but substrate. Therefore, it is possible to state that the scale formed on the surface was depleted from Hf either due to thermodynamic reasons, such as the internal oxidization of Hf, or low dissolution or affinity of Hf to form compounds with the previously formed Nb and Ti compounds. Also, the relatively lower mobility and larger radius of Hf atoms can kinetically lead to a relatively smaller Hf content on the surface.

The results presented in Figure 2.12 demonstrate that mainly high valence Ti^{4+} is present on the surface of all of the alloys studied. However, at lower depths Ti^{3+} and Ti^{2+} also exist. Although several studies attributed these states to TiO_2 or Ti_2O_3 and TiO [95, 96], these Ti oxidation states might also represent the formation of mixed and complex oxides such as $TiNbO_4$ or $ZrTiO_4$ with close oxidation states [97]. Similar behavior was observed for Nb and Ta (Figure 2.12), such that the Nb oxidation state was primarily high valence Nb^{5+} near the surface, with lower layers partially substituting Nb^{5+} with Nb^{4+}, Nb^{3+}, and Nb^{2+} [92, 98]. The distribution of Ta on the surface is mostly associated with Ta^{5+}, and within lower layers, it was replaced partially by Ta^{4+} and Ta^{2+} [99-101]. Noticeably, the amount of Ta does not change significantly along the scale near the surface, which can be attributed to this element's large atomic radius and lower diffusivity.

Quantitatively analyzing Mo XPS measurements can be challenging due to the

difficulty in accurately fitting the peaks associated with Mo, especially when its spectrum overlaps with the spectra of other elements (such as Ta 4d). Therefore, special care was taken to make the peak fitting process consistent with previous works [90], while also maintaining consistency among the current samples. Accordingly, the results presented in Figure 2.12(g-i) show an interesting trend in the samples, such that at 700 °C (Figure 2.12g), the majority of the Mo content was located on the surface, while a smaller quantity was present underneath. In contrast, at 800 °C, close to the MoO_3 volatilization temperature, volatilization occurred as MoO_3 formed and the overall amount of Mo increased, which can be attributed to the increased diffusion of Mo atoms towards the surface to participate in an oxidation reaction, as also indicated by the coexistence of Mo^{6+} mixed with Mo^{4+}. As temperature increased to 900 °C, a decrease in the overall Mo content was observed, and the remaining Mo content in the lower layers was associated with Mo^{4+} (screened), which can be attributed to Mo dissolved in the oxide compounds.

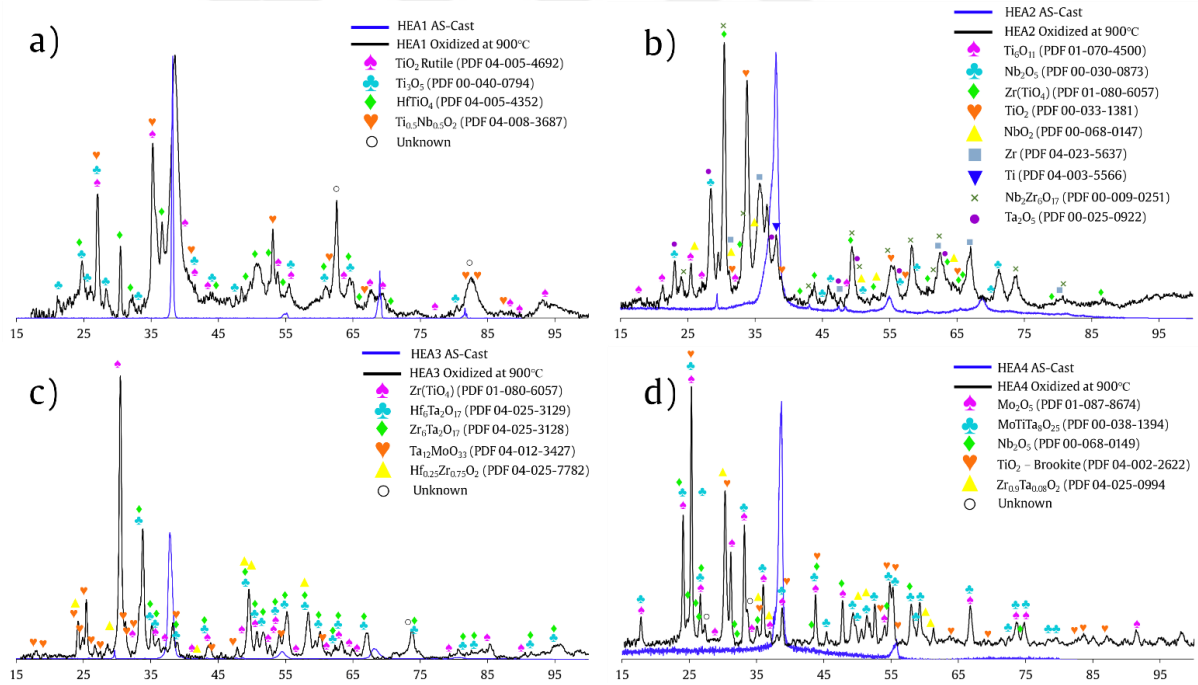

Figure 2.13. XRD scans of a) HEA1, b) HEA2, c) HEA3, and d) HEA4 in the as-cast form (blue) and oxidized at 900 °C (black); some of the compound peaks are not shown for the sake of clarity

The phase distributions in the samples were examined with XRD, as shown in

Figure 2.13, where the data plotted in blue correspond to the as-cast sample, while the black curve represents the oxidized sample at 900 °C in each subplot. Specifically, the HEA1 sample oxidized at 900 °C (Figure 2.13a) exhibited fewer oxide compounds than the other samples, and the peak from the substrate was still significant. Most of the compounds in this sample are Ti-based compounds, which is expected considering the higher atomic percentage of Ti in this sample. The significant TiO_2 (rutile) peak can be attributed to the better oxidation property of this sample, while the mixed oxide of $Ti_{0.5}Nb_{0.5}O_2$ and $HfTiO_4$ can be representative of the aforementioned complex oxidation states as the Ti, Nb, and Hf all exhibit a 4+ state in these compounds. It should be mentioned that there are peaks that could not be accurately assigned to a compound using the available PDF database, and are therefore marked as ”unknown”.

Figure 2.13b presents the XRD profile of HEA2, evidencing the presence of a wider variety of oxides than in HEA1. In this sample, the signal intensity measured from the original as-cast material is much lower than that acquired from the HEA1, indicating a greater occurrence of internal oxidation. However, the elemental peaks of Ti and Zr detected might represent unreacted parts of the sample. Besides, a variety of oxides of Nb and Ti were present in this sample, indicating a mixture of oxides forming in the sample. As for the HEA3 sample (Figure 2.13c) that experienced pesting, the scale powderized from the surface. The corresponding XRD results show that no signal was acquired from the as-cast form, indicating that the sample was completely oxidized. Besides, all the compounds identified are complex oxides, which is one of the side effects of losing the surface scale. Similar to the HEA3, the HEA4 (Figure 2.13d) also lost integrity, and the surface scale was powderized. The mixed oxide of $MoTiTa_8O_{25}$ is a highly complex oxide that matches the present data and does not protect the material due to the non-uniform and porous scale it forms [102]. Besides this compound, a mixture of other porous oxides, such as Nb_2O_5 and Mo_2O_5, prevents the formation of any protective layer, resulting in loss of the scale.

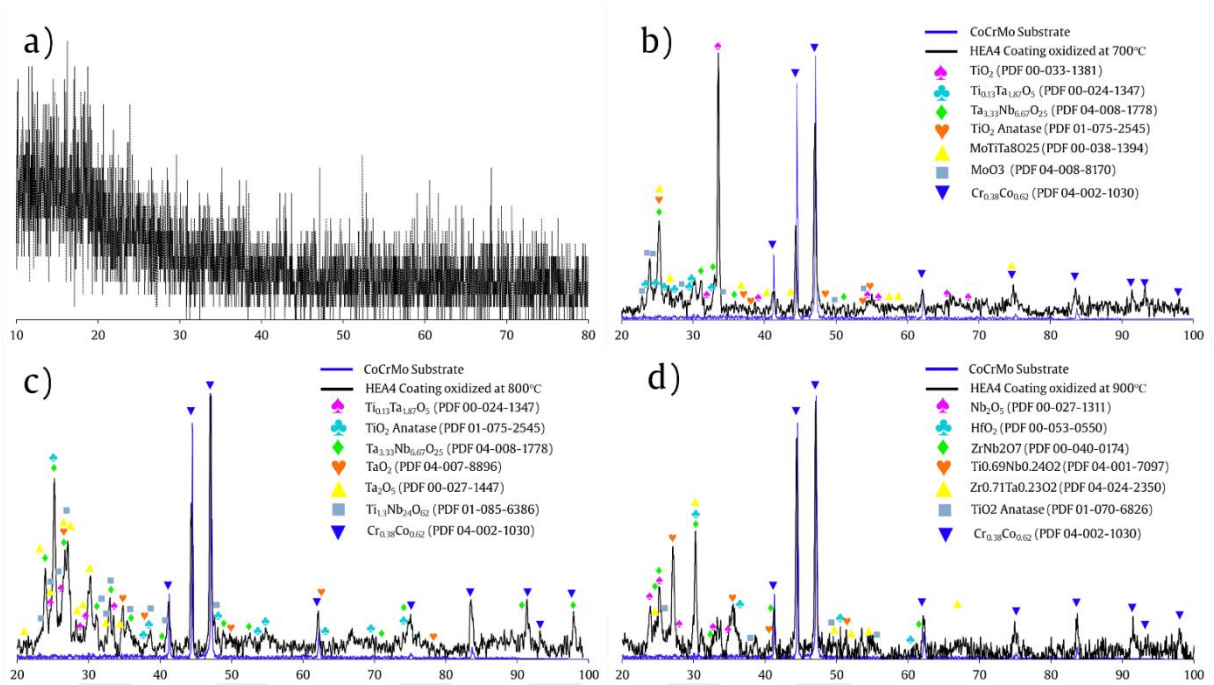

Figure 2.14 a) Grazing incident XRD measurements of the HEA4C sample in the as-coated form, demonstrating an amorphous structure; (b-d) present the HEA4C samples oxidized at 700 °C, 800 °C, and 900 °C, respectively

Figure 2.14a presents the grazing incident XRD measurement results from the surface of the HEA4C sample in the as-coated form, clearly indicating the amorphous nature of the coating, as in the cases of similar PVD-coated RHEAs [86, 87]. Notably, no signal was acquired from the CoCrMo substrate. Figure 2.14 (b-d) presents the GI-XRD measurements from the HEA4C samples oxidized at 700 °C, 800 °C, and 900 °C, respectively. At 700 °C, the sample exhibited significant TiO_2 (anatase), TiO_2 (a hexagonal species), and $MoTiTa_8O_{25}$ peaks. Besides, it also contained MoO_3, which shows that at 700 °C, Mo still existed in higher quantity in the sample. However, as the testing temperature increased, it was not possible to find any significant amount of MoO_3 in the sample. In addition, at 800 °C, the TiO_2 anatase peak increased in intensity, and the hexagonal TiO_2 peak was not detected anymore, while at 900 °C, the anatase peak intensity was very low. In addition, more mixed oxides were formed at 900 °C. A comparison of Figure 2.13d and Figure 2.14d shows the difference in oxidation response between the polycrystalline bulk (HEA4) and the amorphous (HEA4C) samples: at 900 °C, Mo compounds were observed in the HEA4, while no Mo-bearing compound was found in HEA4C at this temperature. The total loss of Mo in the HEA4C sample is attributed to the less compact structure of the amorphous materials that allow for easier

evaporation of MoO_3, in addition to the possibility that Mo atoms formed an amorphous compound not detectable via XRD. On the other hand, due to the polycrystalline structure of the HEA4, Mo atoms had more difficulty diffusing out of the crystal lattice to participate in the volatilization reaction, and thus they formed complex oxides with other elements.

2.4 Discussion

The current set of experimental findings revealed that three different oxidation mechanisms were prevalent in the alloys studied. The first one was observed in the HEA1 and HEA2 samples, which formed and then partially lost their scales during the oxidation experiments (Figure 2.1a-f). Specifically, the loss of scale initiated and progressed around the sample edge, such that compressive or tensile stresses prevailed due to the difference between the oxide and metal volume. The sharp corners and/or edges of the samples act as a point of stress concentration, failing first beyond the plastic limit of the oxide [34]. However, it was apparent that the failure was not limited to the outermost edge of the samples, and rather grew towards the center, as well (Figure 2.2). This can be associated with the fact that failed edges not only produce new points of stress concentration but also allow for the sidewise diffusion of oxygen, which can increase the rate of oxidation. In addition, the oxidation damage on the scaled parts of the samples also revealed itself in form of surface distortion and buckling of the scale (also known as blisters). The formation of such features is representative of compressive stresses resulting from the formation of oxides on the surface [38]. This effect can be estimated by the Pilling-Bedworth ratio (PBR), which is defined to express the ratio of volume change between the oxide and the metal [103]. The PBR values of the high valence oxides observed in the current study are presented in Table 2. Accordingly, Nb and Ta have very high PBR values that can create high compressive stresses on the surface. The combination of the compressive stresses with the depletion of the layer below the scale (Figure 2.4c) would result in the loss of the scale's rigidity, eventually leading to buckling on the surface. In addition to buckling, one of the features that might represent the compressive stresses created on the surface is the formation of whiskers. Previous studies on the formation of whiskers suggested compressive stresses as one of the main drivers of whisker growth on the surfaces of materials, especially in cases where volatile species do not exist [80, 81, 104]. In the case of HEA1 and HEA2,the XPS results (Figure 2.11) suggested the high

Nb content of these whiskers, supporting this argument.

Table 2.2. PBR values for some of the high valence oxide compounds formed by the constituent elements of the RHEA samples.

Compound	PBR
HfO_2	1.62 [105]
MoO_2	2.94 [106]
MoO_3	3.38 [106]
Nb_2O_5	2.69 [105]
Ta_2O_5	2.47 [105]
TiO_2	1.73 [105]
ZrO_2	1.56 [105]

The second mechanism of oxidation observed in the present study was prevalent in HEA3 and HEA4 samples that formed no stable scale, leading to pesting of the whole sample. The main reason for this catastrophic failure was their Mo content, which forms volatile compounds at temperatures as low as 550 °C, reaching its highest oxidation rate at around 830 C° [91]. Due to this rate increase, the additional damage between the samples oxidized at 700 °C and 800 °C is visible, while no further damage was observed upon increasing the temperature to 900 °C. In addition to volatilization, the Mo oxides also have very high PBR values that can cause severe damage even prior to volatilization. Similarly, comparing the difference between HEA3 and HEA4 samples, one can observe the effect of replacing Hf with Nb, such that the noticeably higher PBR of Nb than that of Hf leads to additional stress formation and further damage during oxidation (Figure 2.1).

The oxidation mechanism observed in the amorphous HEA4C sample constitutes the third type of oxidation observed in the present study. Even though the HEA4C sample has the same chemical composition as the HEA4 sample, it exhibited a completely different oxidation response due to its amorphous microstructure (confirmed by GI-XRD (Figure 2.14a)). Specifically, at 700 °C, the HEA4C sample did not show a sign of oxidation visible to the unaided eye. However, using the SEM, one can see the transformation of the amorphous but packed surface (Figure 2.7a) to a porous structure across the whole coating (Figure 2.7b and c) caused by the volatilization of Mo. The

reason that the oxidation occurred throughout the coating is attributed to the fact that amorphous materials have higher diffusion rates for oxygen as compared to the diffusion rate of oxygen in crystalline compounds through both crystal lattice and grain boundaries [107, 108]. The increase in the oxidation temperature caused further damage reflecting itself as island-like spallation of the oxidized coating, leaving a highly porous surface with no significant amount of coated material remaining. The island-like features expanded as the temperature increased to 900 °C, which can be attributed to the sidewise diffusion of oxygen from the already damaged surfaces. This form of damage differs from the pesting of the HEA4 sample that caused uniform spallation of the whole surface. In addition, the fact that Mo compounds still existed in HEA4 at 900 °C (Figure 2.13d) suggests the more difficult volatilization of Mo in the polycrystalline samples as compared to the amorphous counterparts (Figure 2.14 d). Another point of discussion concerns the elemental effects on oxidation. To begin with, the current findings have demonstrated that Nb has a detrimental effect on oxidation in all of the alloys studied herein. The XPS and EDX results suggest that the Nb atoms diffused to the surface, and owing to its high PBR and the highly porous oxides it forms, scale failure was unavoidable. In the case of samples that did not form a scale, Nb severely damaged the integrity of samples due to similar reasons. As for Hf and Zr, both the EDX and the XPS results suggest that these elements tend to oxidize internally and did not diffuse to the surface to participate in scale formation. The difference between the oxidation responses of Hf and Nb is visible in HEA3 and HEA4, demonstrating the internal oxidization of Hf while its lower PBR prevents extensive damage similar to the one caused by Nb. The Ti and Ta elements, on the other hand, can have different oxidation responses depending on the experimental condition and the alloy. While Ta internally oxidized in HEA1, it participated in the scale formation in HEA2. On the other hand, Ti can form a semi-protective layer when its concentration is high (HEA1), and the temperature is low. However, it did not provide any protection with lower concentrations and at higher temperatures. Finally, the Mo element had a detrimental effect in all instances, as the volatilization prevents any uniform formation of scales. Therefore, if a RHEA does not have effective oxide formers or protective layers, Mo will lead to failure at elevated temperatures.

2.5 Conclusions

In this study, four polycrystalline refractory high entropy alloys (RHEAs), namely HfNbTaTi (HEA1), HfNbTaTiZr (HEA2), HfMoTaTiZr (HEA3), and NbMoTaTiZr (HEA4) alloys, and an amorphous NbMoTaTiZr (HEA4C) RHEA were studied to uncover the oxidation mechanisms active. In particular, polycrystalline alloys produced by vacuum arc remelting and the amorphous alloy made via PVD were oxidized at 700 °C, 800 °C, and 900 °C. Subsequently, the oxidized samples were thoroughly characterized utilizing a variety of microscopy techniques. The corresponding set of experimental findings demonstrated the presence of three distinct oxidation mechanisms: (i) scale forming, loss of scale owing to stress concentration and subsequent buckling of scale and formation of whiskers, (ii) powderization of samples facilitated by the volatilization of Mo, and (iii) thorough oxidation of the amorphous coating due to the higher diffusion rate of the oxygen within the porous surface. Furthermore, Mo was shown to cause catastrophic failure of the samples due to the volatilization at temperatures as low as 700 °C, while Nb was also found to be detrimental as its oxide diffuses to the surface and damages the scale due to its high Pilling-Bedworth ratio. Overall, the current findings emphasize the need for careful tailoring of the elemental compositions of RHEAs prior to their utility at elevated temperatures.

Chapter 3:
Atomistic Simulation of Chemical Short-Range Order and its effect on Mechanical Properties of Refractory High Entropy Alloys at Various Temperatures

3.1 Introduction

In the last 20 years, the concept of high entropy alloys (HEAs) has attracted attention due to opening a new door to a vast compositional space (four or more elements with compositions ranging from 5 to 35 at.%) that grants the possibility of achieving enhanced properties for a variety of applications [58, 109]. As a result of many studies focusing on HEAs, two family of alloys stand out due to their desirable properties: single-phased FCC-structured HEAs with CoCrFeNiMn being the most prominent one [1] and single-phased BCC-structured ones with HfNbTaTiZr being the most well-known [14]. The HfNbTaTiZr alloy and other alloys of this family have the advantage of containing high melting point refractory elements in their composition, therefore having the potential to be utilized in high and ultra-high-temperature applications. Besides the potential high-temperature applications, their desirable toughness and ductility at room temperature [17] and their relatively high strength at high temperatures [110] can provide an opportunity for deepening the knowledge on the trade between ductility and strength and the role of different strengthening mechanisms.

The conventional strengthening approaches of metallic alloys at room temperature include methods such as solid-solution strengthening, grain refinement, and precipitate hardening. However, in high-temperature applications, alternative solutions are needed due to the effect of temperature on the microstructure. In particular, grain refinement methods fail to provide a sustainable hardening method as grains recrystallize and grow if exposed to sufficiently high temperatures [111, 112]. In addition, polycrystalline materials under constant load suffer from creeping at high temperatures, necessitating the use of single crystalline materials for critical components. Moreover, precipitate hardening methods are restricted to specific groups of alloys at high temperatures, as many of the precipitated phases decompose or transform at high temperatures, losing their hardening effect [113]. Therefore, a method that can provide hardening independent of the grain structure of the materials and is able to enhance the properties of the matrix of an alloy is highly desired.

Chemical short-range order (CSRO), being defined as the formation of order in an alloy

in the atomic scale over domains of several nanometers, is a phenomenon that can be utilized to improve the mechanical properties of materials [114, 115]. The mechanism behind the CSRO strengthening effects is a highly debated topic. However, based on the results of experimental works, two of the suggested mechanisms are more agreed on. One, the CSRO increases the yield strength of the materials as it increases the energy needed to initiate the slip of dislocations [116, 117]. Secondly, the CSRO has a friction-hardening effect; therefore, it not only increases the yield strength, but also increases the overall flow stress of the materials [118]. Considering these two mechanisms, CSRO can be used as a potential tool to engineer the mechanical properties of HEAs, as the compositions of these alloys can provide the possibility of CSRO formation.

One of the main reasons for the uncertainties regarding CSRO's hardening mechanisms is the difficulty of experimental conditions to directly observe the formation of CSROs and their interaction with the surrounding atoms under loading. In particular, such measurements need the samples to undergo in-situ experiments under high-resolution transmission electron microscopy (TEM). Even in such cases, isolating the effect of CSRO from other potential hardening effects is challenging due to sample preparation difficulties. More importantly, such experimental considerations are even more restrictive for observing CSRO effects at high temperatures [119, 120]. Therefore, any tool that can facilitate the investigation of the hardening mechanisms of CSROs can lead to the development of a novel approach to enhancing HEA's mechanical properties.

Out of the computational methods, Atomistic simulations are the primary tools to shed light on phenomena such as CSRO originating from the atomistic scale. Within the different atomistic simulations, the ones using interatomic potentials (empirical force fields) are preferred for the investigation of mechanical properties as they require a large number of atoms to capture the different aspects of material deformation. Therefore, using the proper interatomic potentials, molecular dynamics (MD), and Monte-Carlo (MC) simulations can deepen the knowledge of materials in conditions where experimental methods or other types of atomistic simulations are prohibitively expensive. In this regard, a handful of studies have applied MD and MC simulations to gain insight into the CSRO effect on the Medium entropy alloys (MEAs) and HEAs. Jian et al. performed MD and MC simulations on the CoCrNi MEA to understand the effect of lattice distortion and the CSRO on the deformation mechanism of this alloy. They found out that the Shockley partials form inside the CoCr-ordered clusters, which have the lowest stacking fault energy compared to the other regions, resulting in higher shear strains in these phases

[121]. Zhang et al. performed similar simulations on the CoCrNi alloy focusing on CSRO and found that the significant toughness and strength of CoCrNi alloys arise from the combination of CSRO and twin-induced deformation [122]. In the case of HEAs, Haung et al., by performing ab initio calculations, developed an interatomic potential for the HfNbTaTiZr system to investigate the formation of CSROs in these alloys. Although most of their work is dedicated to developing interatomic potential, they successfully showed the formation of CSRO with the B2 ordering in these alloys. However, they did not investigate the mechanical effect of the CSRO on the alloys [123]. Therefore, a clear understanding of the CSRO hardening mechanism in the HfNbTaTiZr refractory high entropy alloys (RHEAs) is still missing.

In this study, two alloys of HfNbTaTiZr and $HfNbTaTi_3$ were chosen as a representative of the BCC-structured RHEAs, which have already shown promising properties in several previous studies [20-22]. The hypothesis in this work is that CSRO in RHEAs of HfNbTaTiZr alloys significantly affects the mechanical properties and can be a defining factor in improving the hardness, toughness, and ultimate strength of the investigated alloys. To support this hypothesis, using the interatomic potential developed by Huang et al. [19], BCC systems of each alloy were created with random configurations of atoms for each element. Subsequently, Monte Carlo simulations were performed to achieve the equilibrium state of the systems. After examining the state of the systems for the possible formation of CSROs, these systems were utilized to conduct compression simulations for different system sizes, strain rates, and temperatures to understand the effect of these parameters. In addition, the evolution of the systems during the simulations were observed, unraveling the phase changes due to deformation in these alloys. To validate these results, microhardness measurements and in-situ compression tests under SEM were conducted to validate the phase transformation and the strengthening effect of the formation of CSROs. The microhardness measurements validated the increase in the hardness of the alloys, and the BCC to HCP phase transformation was supported by post-deformation XRD measurements. Finally, cryogenic in-situ XRD measurements and cryogenic scanning electron microscopy imaging were conducted to detect the formation of possible temperature-induced martensite. Overall, the results of this work suggested the positive effect of CSROs on the hardness and strength of the RHEAs while pointing out the importance of grain boundaries on the overall strength of these alloys.

3.2 Computational methods and validation experiments

Atomistic Simulations

In order to perform atomistic simulations on the $HfNbTaTi_3$ (named H1 for convenience) and HfNbTaTiZr (equimolar, named H2) alloys systems, a 20X20X20 base centered cubic (bcc) single crystals of the alloys with their respective atomic composition were constructed using Atomsk [124]. These systems were utilized as the initial configuration of atoms to perform the hybrid Monte-Carlo (MC) simulations to investigate the formation of chemical short-range order (CSRO) and their effect on the mechanical properties of HEAs at room temperature (300K) and high temperatures (1273K). Periodic boundary conditions were applied in three dimensions for systems, and all of the simulations were performed in a Large-scale Atomic/Molecular Massively Parallel Simulator (LAMMPS, version 23 Jun 2022) [125]. The interatomic potential used in this work was developed by Huang et al. for the HfNbTaTiZr system. This potential has shown accurate results in reproducing the physical properties of HfNbTaTiZr and alloys made with similar compositions [123]. Visualization and detection of the crystal structure of the systems were conducted using OVITO (version 3.9.4) [126].

In order to perform hybrid Monte Carlo (MC) simulations to achieve the equilibrium state of the systems, the atom/swap method implemented in LAMMPS was used [53]. This method has already proven its capability to achieve the equilibrium state of other systems [123, 127]. The H1 and H2 systems were equilibrated for 30 ps under an isothermal-isobaric (NPT) ensemble at the intended temperature. Subsequently, the atom/swap fix in the LAMMPS was utilized. This fix performs 10 MC swaps every 100 steps for each pair of atoms for 1 million steps. During this process, an NPT ensemble with a nose-hoover thermostat and barostat is applied to accommodate the changes in the system. The systems before the MC simulations are designated AS (As-is); after the MC simulations, they are designated AN (Annealed) for convenience.

In order to perform compression on HEAs, the aforementioned systems were duplicated 2 and 4 times in each direction, as mentioned in Table 1. Larger systems used here are necessary to capture different aspects of materials' mechanical properties on an atomistic scale. To perform the compression tests, systems were equilibrated for 30 ps and then compressed by the engineering strain rate mentioned in Table 1 in the [100] direction. This direction has been selected as previous studies showed that the [100] family has higher stability to crystal rotation [128]. The simulation length was chosen in a way that

the final strain was 30%.

In order to measure the CSRO, the Pyscal library [129] was utilized, which uses the following formula for measuring the pairwise short-range chemical order, which is based on the de Fontaine [130] work:

$$\alpha_{ij} = \frac{n_j/m_A - c_j}{\delta_{ij} - c_j}$$

In this formula, i refers to the reference atom type, n_j is the number of atoms of the non-reference type between the c_j atoms in the ith shell and m_A is the concentration of non-reference atoms. The value of α_{ij} is equal to one if the i and j are equal.

Table 3.1 Simulation Information of the molecular dynamics' simulations.

Sim. #	Alloy	State	Temp. (K)	Size	Width in (A)	#Atoms (k)	Engineering Strain Rate (%/ps)	Simulation run (k)	strain (%)
1	H1	AS	300	20X20X20	66.49	16	0.5	60	30
2	H1	AS	300	20X20X20	66.49	16	1	30	30
3	H1	AN	300	20X20X20	66.49	16	0.5	60	30
4	H1	AN	300	20X20X20	66.49	16	1	30	30
5	H1	AN	1273	20X20X20	66.49	16	0.5	60	30
6	H1	AN	1273	20X20X20	66.49	16	1	30	30
7	H2	AS	300	20X20X20	66.49	16	0.5	60	30
8	H2	AS	300	20X20X20	66.49	16	1	30	30
9	H2	AN	300	20X20X20	66.49	16	0.5	60	30
10	H2	AN	300	20X20X20	66.49	16	1	30	30
11	H2	AN	1273	20X20X20	66.49	16	0.5	60	30
12	H2	AN	1273	20X20X20	66.49	16	1	30	30
21	H1	AS	1273	20X20X20	66.49	16	1	30	30
22	H1	AS	1273	20X20X20	66.49	16	0.5	60	30
21	H2	AS	1273	20X20X20	66.49	16	1	30	30
22	H2	AS	1273	20X20X20	66.49	16	0.5	60	30
13	H1	AS	300	40X40X40	133.1	128	1	30	30
14	H1	AN	300	40X40X40	133.1	128	1	30	30
15	H2	AS	300	40X40X40	133.1	128	1	30	30
16	H2	AN	300	40X40X40	133.1	128	1	30	30
17	H1	AS	1273	40X40X40	133.1	128	1	30	30
18	H1	AN	1273	40X40X40	133.1	128	1	30	30
19	H2	AS	1273	40X40X40	133.1	128	1	30	30
20	H2	AN	1273	40X40X40	133.1	128	1	30	30

Validation experiments

Two refractory high entropy alloys (RHEAs) of $HfNbTaTi_3$ and HfNbTaTiZr were produced using vacuum arc melting (VAR) under a Ti-gettered atmosphere. During this

process, the button-shaped samples were flipped several times and remelted to achieve higher homogeneity. Subsequently, samples were machined down to large disk shapes, and then rectangular samples of 10x5x1 mm were cut from both alloys using electrical discharge machining (EDM). To assess the effect of heat treatment and the potential formation of CSRO, the samples were placed inside a quartz tube, and after several purging of argon, a vacuum was applied to the tubes. Subsequently, the samples were annealed at 1000 °C for 72 hours and were water-quenched afterwards. The samples with no heat treatment are designated as AS (As-cast) and after heat treatment are called HT (heat treated). In addition, to perform compression tests and evaluate the response of the material under loading, four cylindrical samples with 1 mm diameter and 3 mm height were cut using EDM, and two of them were heat treated in a similar way mentioned before.

Crystallography and phase analysis were done using the X-ray diffraction method (XRD, Bruker D8 Advanced X-ray diffractometer, Cu-Kα source). In order to obtain the potential phase changes in the alloys due to temperature, a low-temperature XRD measurement was conducted using liquid nitrogen. During the measurement, samples were put on an aluminum heat sink inside an insulated vessel. The measurement of temperature using a thermocouple showed roughly -120 °C during measurements.

To analyze the microstructure and the chemical distribution of elements in the samples, scanning electron microscopy (SEM, Zeiss Supra 55 VP) was utilized in combination with energy dispersive x-ray (EDX) mapping (Bruker AXS GmbH, Karlsruhe, Germany). Using the same microscope, the in-situ compression experiments were conducted using a compression module (Kammrath-Weiss GmbH) to detect the response of the H1 alloy under compression. To measure the hardness of the alloys, the microhardness method (Struers, Duramin) was used with a force of 981.2 mN and an indentation time of 13 seconds. Each measurement was repeated at least six times, and the indentation points were selected within the grain of the samples.

3.3 Computational results

Short range chemical order (CSRO)

In order to perform an analysis of the effects of the CSRO on the mechanical properties of HEAs, the first step is to assess the formation of such orderings in these materials. To do so, the CSRO parameters of the MC simulations are provided in Figure 3.1-3.4 for both H1 and H2 systems at 300K and 1273K. In these results, positive values represent pairwise repulsion, negative values show the pairwise attraction of elements, and zero represents random distribution. In Figure 3.1, two clear trends are visible; the pairs of Ta and Nb are highly attractive to each other, while they are repulsive to the rest of the pairs. On the other hand, the Hf and Ti pairs attract each other and repel the other pairs. Therefore, the original random order is not a thermodynamically stable state. Figure 3.2 Shows the effect of temperature on the pairs mentioned in Figure 3.1. As can be seen, temperature suppresses the extent of attraction/repulsion behavior; however, they exist with pairs of Hf-Nb, Hf-Ta, and Nb-Ta being the most repulsive and Hf-Ti and Ta-Ti being the most attractive. Considering these results, it is reasonable to say that the CSRO formation and the pairs involved in it are temperature dependent, as the temperature defines the thermodynamics of the formation of CSROs, and MC simulations only consider the thermodynamic effects and not the kinetics. In addition, consideration should be made for the alloys such as H1 with non-equimolar content, as the elements with higher content (here Ti) can have inflated values for other pairs. Thus, it is possible to say that thermodynamically, the H1 alloy is more random at higher temperatures and CSROs form to a greater extent at lower temperatures.

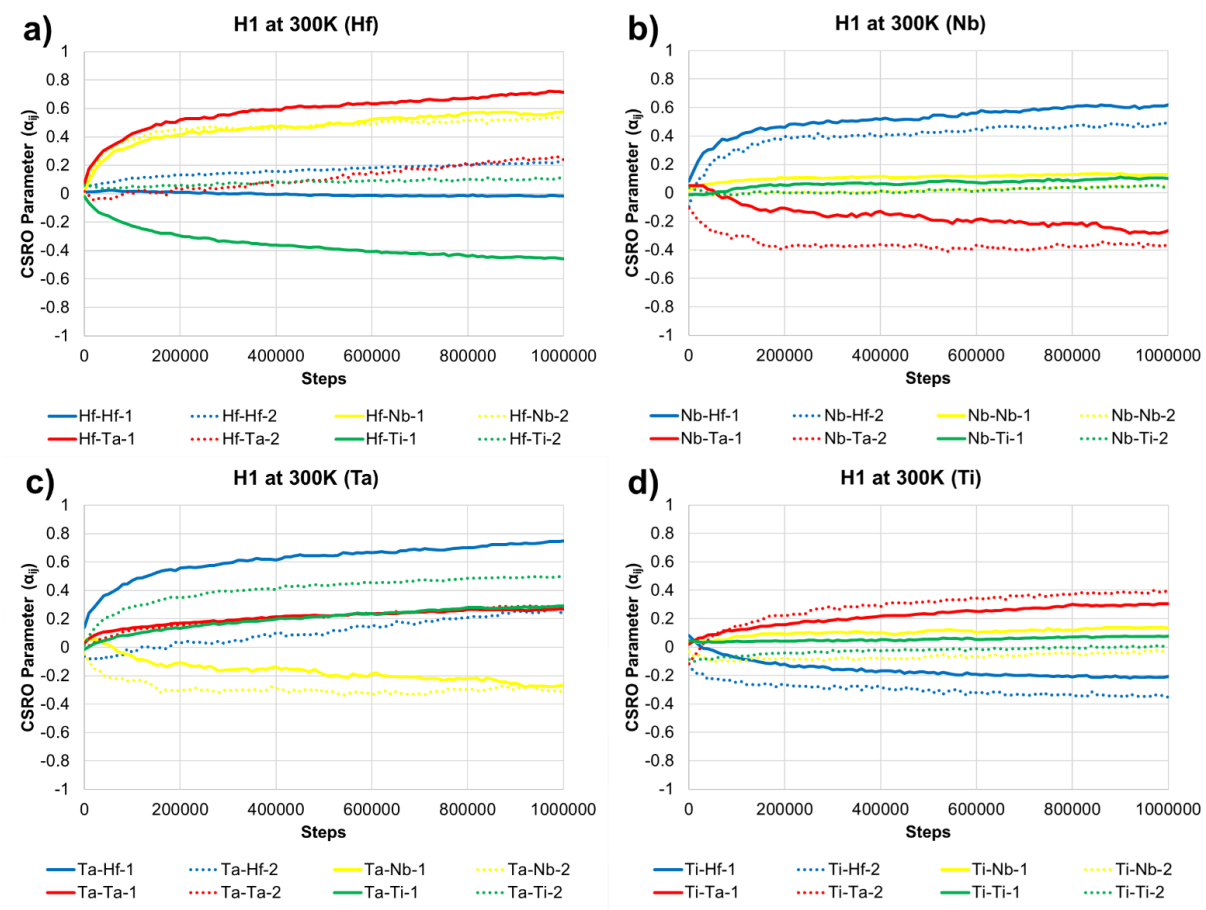

Figure 3.1 CSRO parameters of H1 alloy calculated for pairs of a) Hf, b) Nb, c) Ta, and d) Ti during MC simulation at 300K representing the short-range order in the alloy. Numbers beside the pairs represent the first and second shells from which the parameters were calculated.

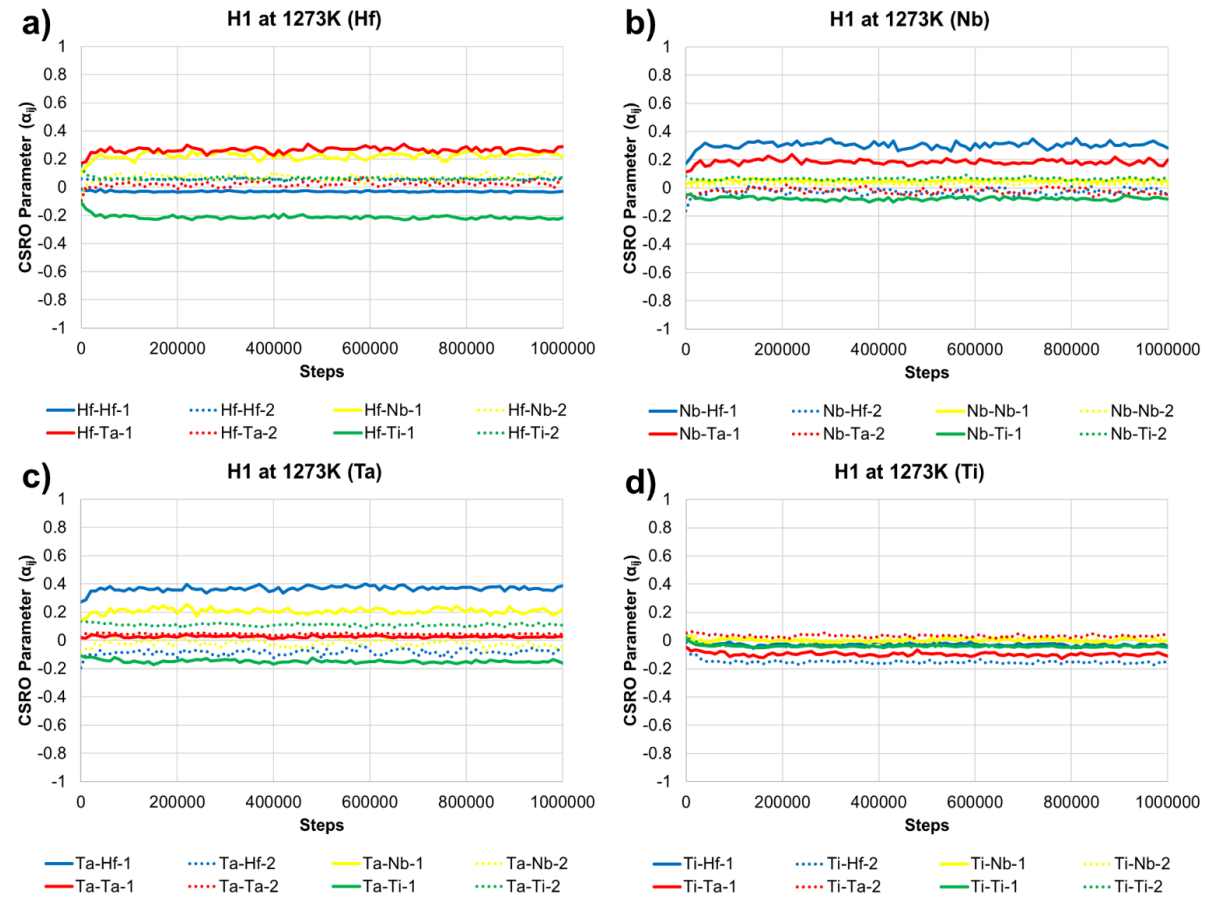

Figure 3.2. CSRO parameters of H1 alloy calculated for pairs of a) Hf, b) Nb, c) Ta, and d) Ti during MC simulation at 1273K.

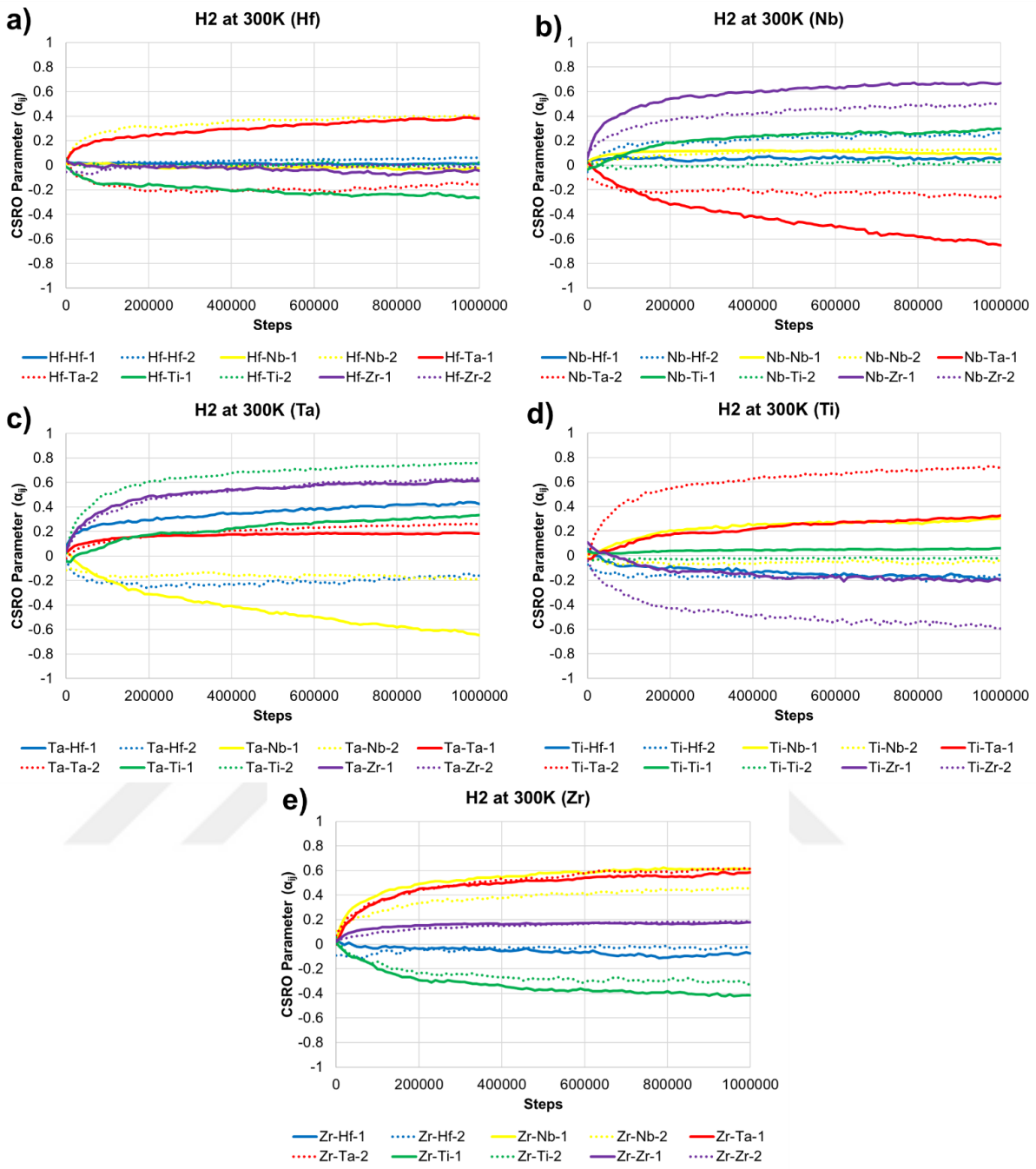

Figure 3.3. CSRO parameters of H2 alloy calculated for pairs of a) Hf, b) Nb, c) Ta, d) Ti, and e) Zr during MC simulation at 300K.

Figures 3.3 and 3.4 show the CSRO parameters calculated during the MC simulation for H2 alloy at 300K and 1273K temperatures. Similar to the H1, the initial random configuration was not stable, and it is clear that some pairs have the tendency to form CSRO. At 300K, the most prominent attractive pairs are Nb-Ta, Hf-Ti, and Ti-Zr and the repulsive ones were Hf-Ta, Hf-Nb (second shell), Nb-Zr, Nb-Ti, Ta-Ti, Ta-Zr. The Nb-Ta pair was previously reported by Huang and experimental works to form B2 ordering [17, 123] as shown in Figure 3.5 a. However, the formation of ordering between the Hf-

Ti and Ti-Zr can be seen that was not reported before (Figure 3.5 b). In addition, there are some HCP phase forming that are rich with Hf, Ti, and Zr (approximately 75 at.%). Considering the fact that the Hf-Zr pair does not show any sign of attraction, one can say the attraction caused by Ti can bring Hf and Zr together to form the HCP phase. Such phases have been detected experimentally in bulk form in H2 samples [131]. Figure 3.4 shows the effect of temperature on the formation of CSRO in H2 alloy. Unlike the H1 sample, which had a significant difference between the two temperatures, most pairs maintained their pairwise attraction or repulsion position. However, similar to H1, the higher temperature causes the extent of CSRO to reduce. In addition, it is noticeable that higher temperature causes quicker convergence of CSRO parameters; however, it should not be associated with higher diffusion rates, as MC simulations do not consider the kinetics of the reactions. The faster convergence is due to higher energy of the systems that can result in a higher number of MC attempts to be accepted.

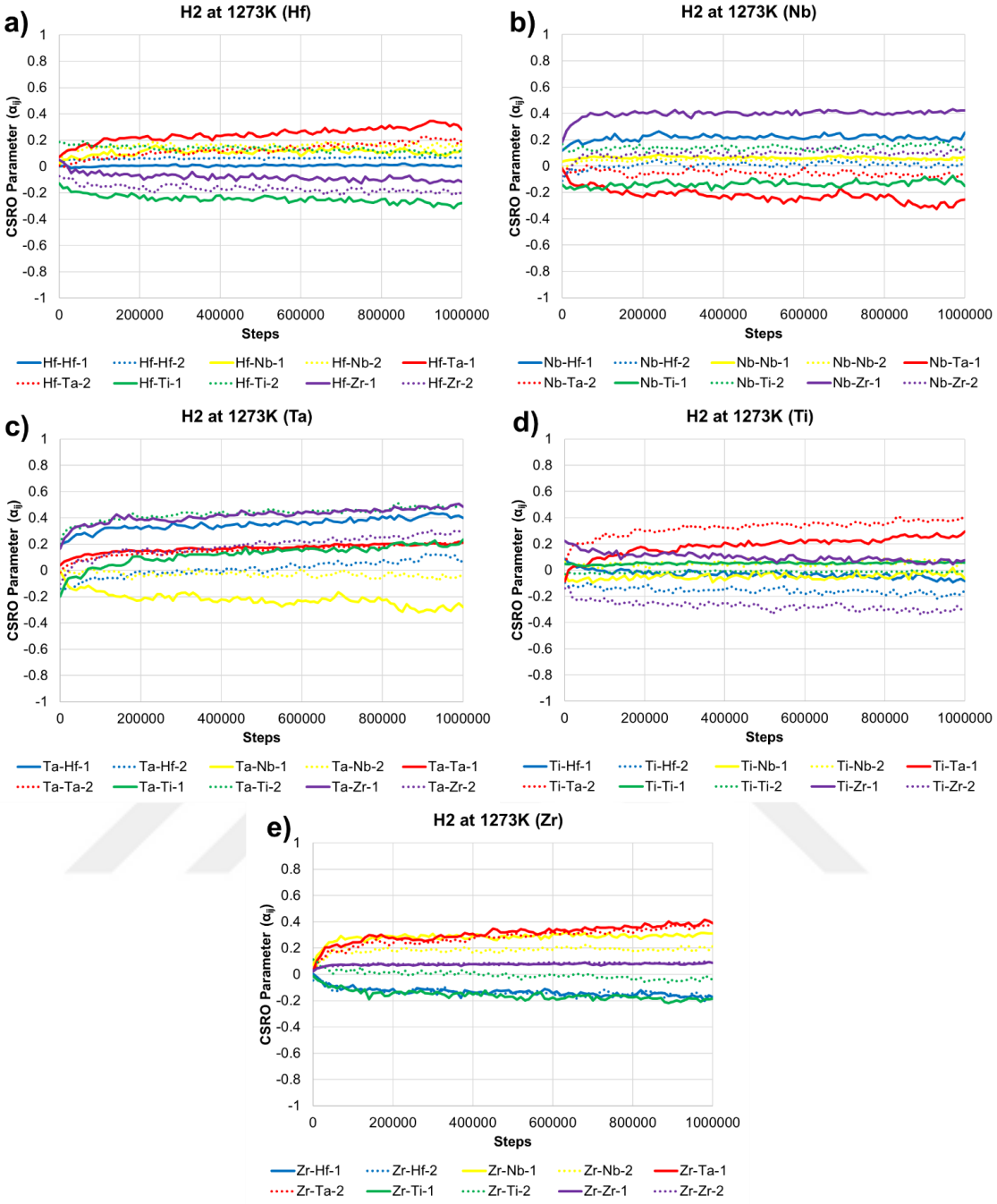

Figure 3.4. CSRO parameters of H2 alloy calculated for pairs of a) Hf, b) Nb, c) Ta, d) Ti, and e) Zr during MC simulation at 1273K.

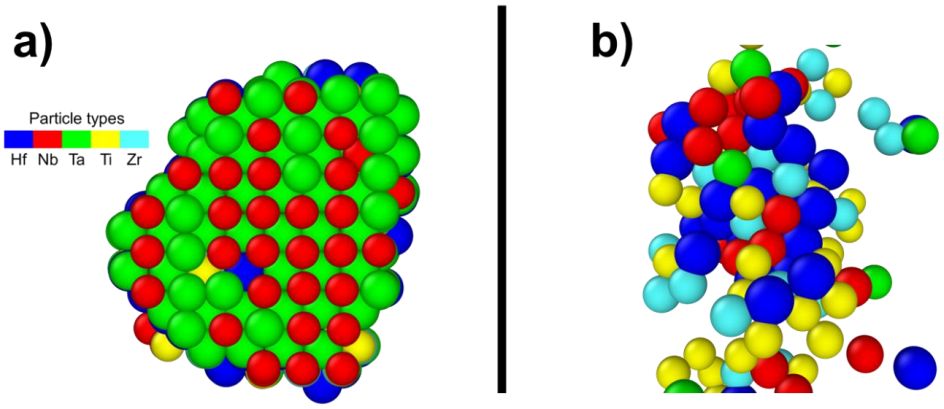

Figure 3.5 Visual examples of the formation of CSRO in the H2 alloy. a) B2 ordering b) formation of Hf-Ti-Zr rich clusters.

Compression simulations

In order to understand the effect of CSROs on the mechanical properties of HEAs, compression simulations were performed on the H1 and H2 alloys in two states of AS (before MC simulations) and AN (After MC simulations) in both 300K and 1273K temperatures. Before focusing on these systems' mechanical response, it is necessary to validate if the results have converged to a sufficiently accurate position. Therefore, to validate the convergence of the results, simulations were performed on two different sizes of 20X (16000 atoms) and 40X (124000 atoms). To be more specific, certain mechanical properties and deformation mechanisms are dependent on the number of atoms involved in them. Therefore, in the case that the system size is not large enough, this deformation mechanism simulated by MD might not reflect the phenomena properly. The results of the simulations for different sizes are presented in Figure 3.6. As can be seen, the results of the simulations in all alloys, states, and temperatures are similar and do not have a significant deviation from each other, and it is possible to use the system with 16000 atoms for further studies. In addition to the size effect, one can validate the results' relevance by examining the material's behavior under different strain rates. As shown in Figure 3.7, the strain rate increase is causing increased hardness and strengthening in the materials. This is an expected behavior in the materials investigated by MD simulations, as suggested by previous studies [132]. Considering these two validation steps, one can argue that the MD simulations performed on the materials are reasonably accurate for the intended orientation and system size.

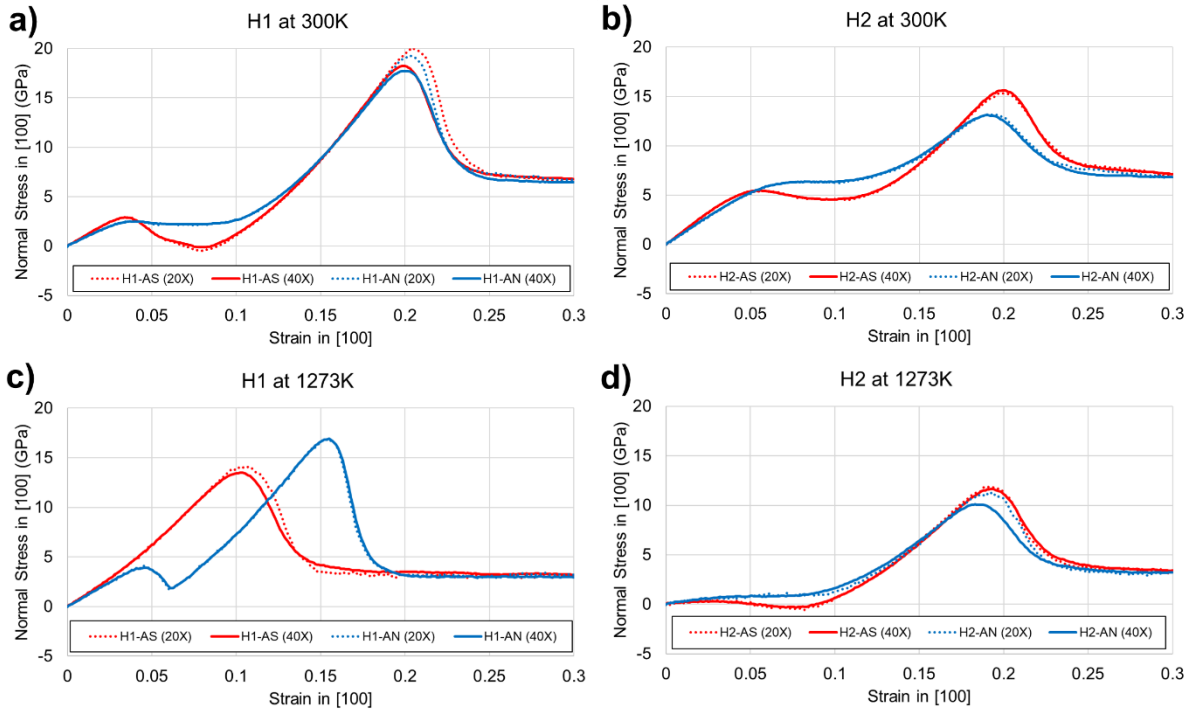

Figure 3.6 The stress-strain curve resulting from compression MD simulations of H1 and H2 presents the system size effect on the simulation results.

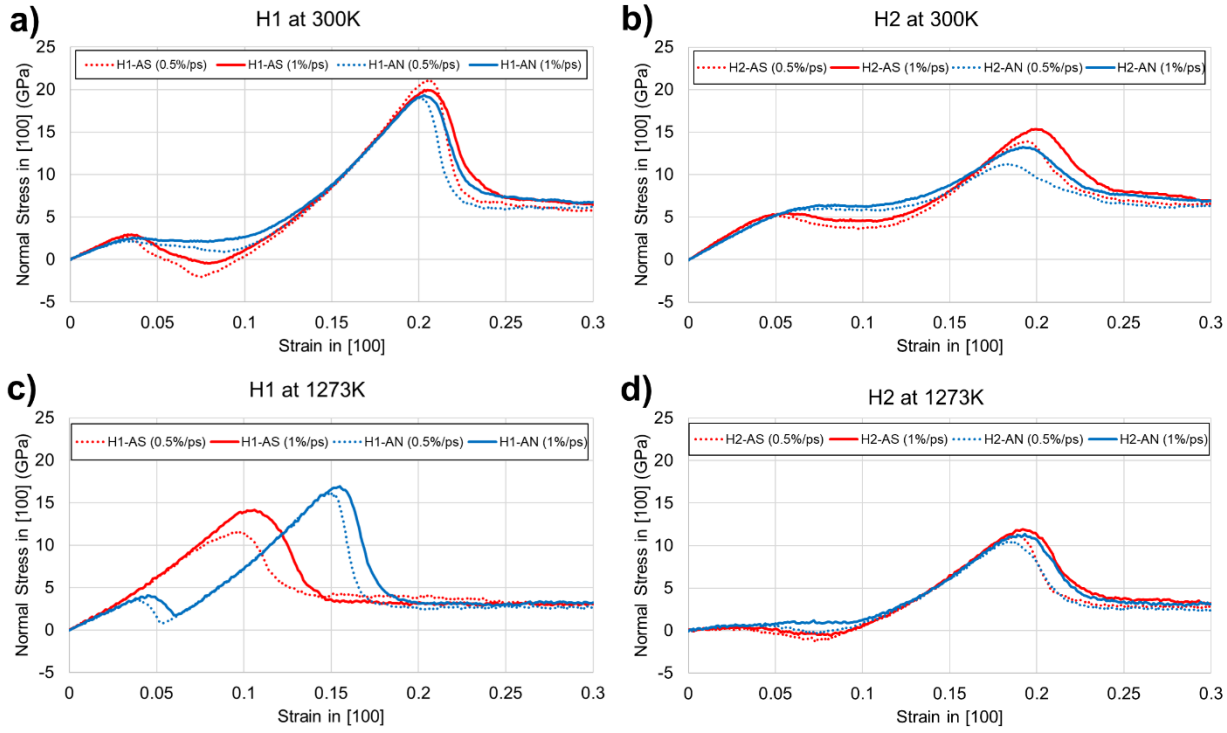

Figure 3.7. The stress-strain curve resulting from compression MD simulations of H1 and H2 (20X system size) presents the strain rate effect on the simulation results.

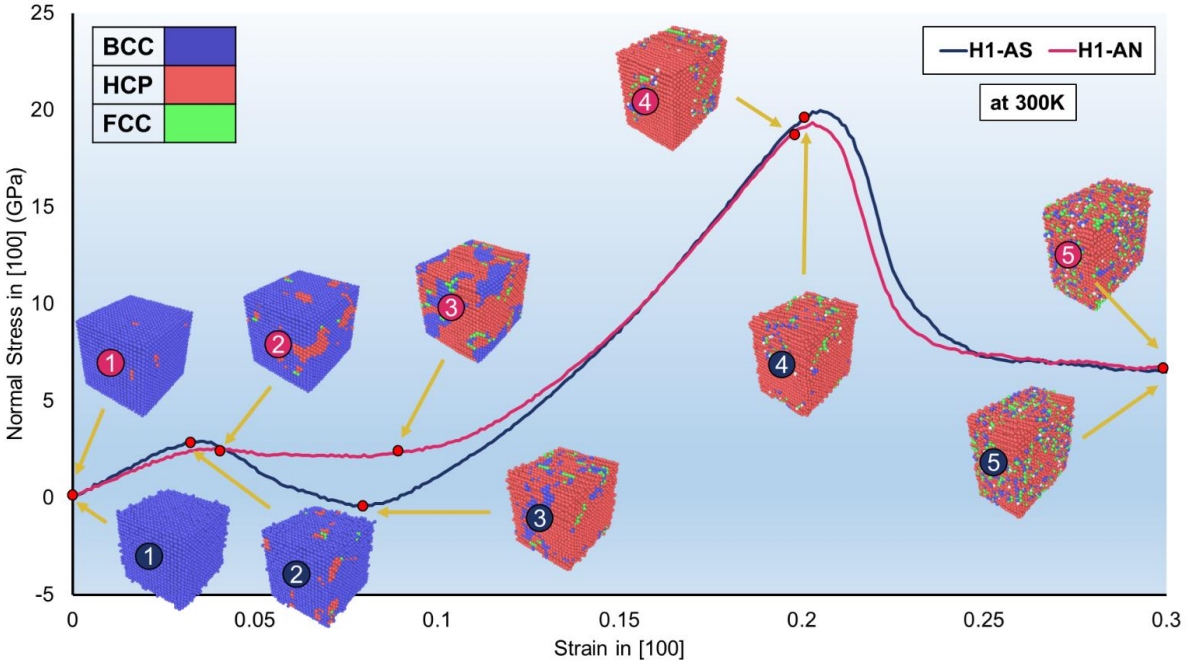

Figure 3.8 Stress-strain curve acquired from the compression simulations of H1-AS and H1-AN system at 300K. The materials crystal structure is provided beside the curves.

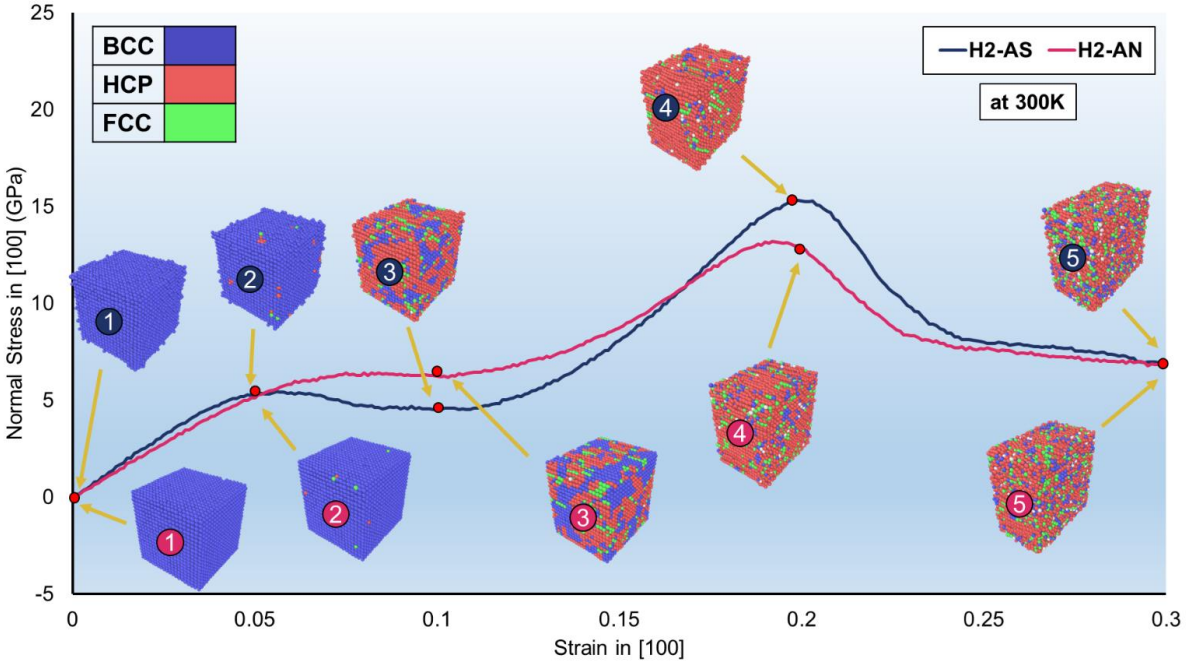

Figure 3.9 Stress-strain curve acquired from the compression simulations of H2-AS and H2-AN system at 300K. The systems' crystal structure is provided beside the curves.

The data presented in Figure 3.8 includes the Stress-Strain curve and the state of the H1 alloy during compression at 300K. As can be seen, both H1-AS and H1-AN start from the BCC structure, with some atoms of HCP configuration in H1-AN formed after the

MC simulations. As the deformation initiates in the H1-AS system, the stress measured in the [100] direction increases up to approximately 4%. After this point, the stress values decrease noticeably, suggesting not only strain-hardening does not occur in the material, but a negative stress value around 8% deformation was observed. The increase and decrease in the stress measured in the HEAs at this range has already been observed experimentally in other families of HEAs and is attributed to the twinning nucleation [133]. However, one might question the negative stress values acquired around 8% deformation. This rather odd behavior is due to the nature of MD simulations. In particular, unlike experimental methods that the deformation is caused by a certain amount of load applied on a surface; the deformation is applied to the system, and the resulting stresses are measured. Therefore, in the cases that material spontaneously transforms, deforming the system does not require any stress.

The crystal structure of the H1-AS system at around 8% is mostly HCP, suggesting the deformation-induced phase transformation (DIPT) from BCC to HCP which has been observed in FCC HEAs [134, 135]. Subsequent deformation in the sample follows the typical strain hardening behavior until failure at 20% deformation. In contrast to H1-AS, the H1-AN sample does not show the twinning behavior as was observed in the H1-AS. However, the BCC to HCP transformation makes it clear that the DIPT behavior exists in this system, resulting in additional ductility in this material. Similar to H1-AS, the H1-AN follows a strain-hardening behavior after 10% deformation. Comparing the two states of H1-AS and H1-AN, one can argue that the CSRO formation in the AN system has made the formation of Twinning-induced plasticity (TWIN) more difficult, resulting in additional strength.

Figure 3.9 presents the compression results for the H2 samples at 300K. In comparison to H1 systems, both H2-AS and H2-AN show higher strength. Deformation of the H2-AS sample shows a reduction in the stresses around 5% deformation, similar to H1-AS, and is attributed to twinning initiation in the systems. The system's structure of around 10% deformation suggests that the BCC to HCP transformation also exists in this system. Further increase in the deformation results in the strain hardening. The effect of CSROs in the H2-AN system has similar properties compared to the H1-AN. Here, the annealing increases the strength of the material during plastic deformation. However, the failure stress in the H2-AN is lower than in H2-AS. Comparing the results of the H1 and H2 at room temperatures suggests the overall positive effect of CSROs on the deformation response of both HEAs studied. Both materials had an increase in their strength, while

the ductility of them was not compromised.

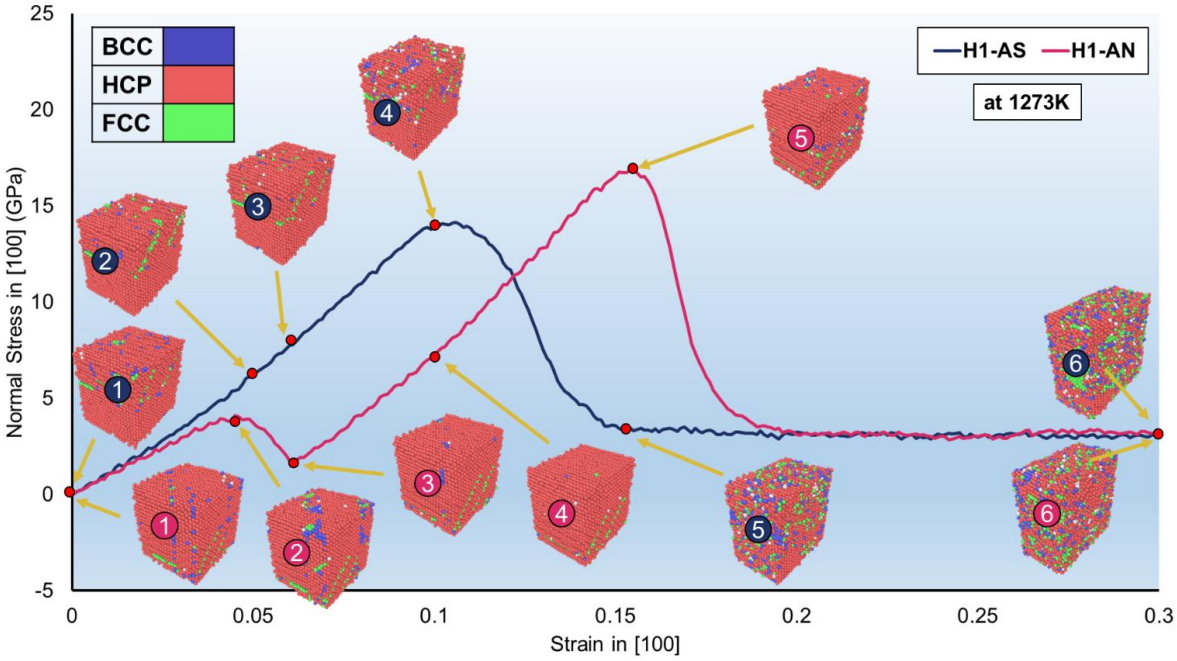

Figure 3.10 Stress-strain curve acquired from the compression simulations of H1-AS and H1-AN system at 1273K. The systems crystal structure is provided beside the curves.

Figure 3.10 presents the results of compression simulation on the H1 systems at a temperature of 1273K. The first observation is that, unlike the 300K systems, H1 systems have an HCP crystal structure at this temperature. Therefore, the deformation response of the H1-AS sample at this temperature is different from the 300K one. As can be seen, the sample does not show any sign of twinning (reduction in the stresses), and the strain-hardening phenomenon exists in this sample from the start of the deformation. On the contrary, the H1-AN system has an entirely different response, showing an apparent twinning effect and a subsequent strain hardening with overall strength and ductility higher than the H1-As. Considering these two curves, it is reasonable to say that in the H1 sample, the formation of CSRO, although not as pronounced as the lower temperature one, improved the ductility of the systems and enhanced the strength of the H1 system.

The compression results of the H2 system at 1273K are provided in Figure 3.11. Unlike the H1 system, the crystal structure of the H2 system remained BCC at 1273K. Therefore, the deformation on H2 samples is more relatable to the lower temperatures. As can be seen, the deformation in the samples happens with minimum resistance from the material up to 10% deformation for both AS and AN state. During the deformation, HCP phases

form in both samples. However, there is a slight hardening in the H2-AN, resulting from CSRO formation. After 10% deformation, the strain-hardening behavior is observed until failure. Considering these results, one can deduce that although the yield strength of the H2 material is very low at high temperatures, the formation of CSRO can help stabilize the material to some extent by disrupting the TWIN behavior in the material.

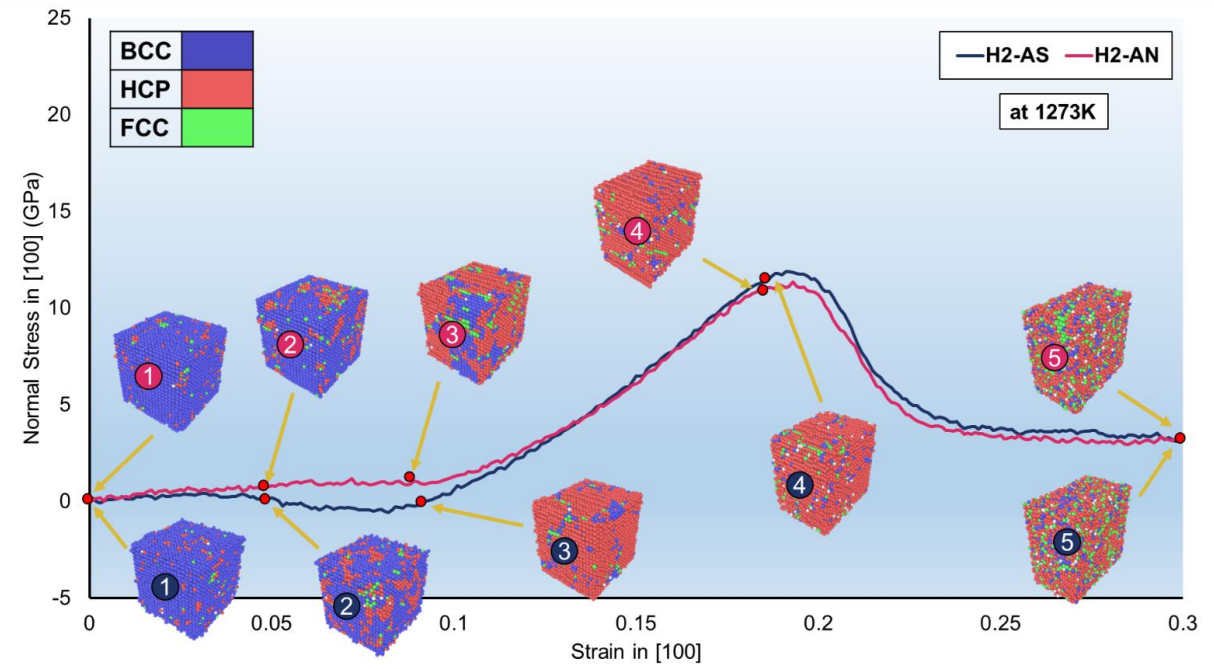

Figure 3.11 Stress-Strain (S-S) curve acquired from the compression simulations of H2-AS and H2-AN system at 1273K. The systems' crystal structure is provided beside the curves.

3.4 Validation experiments results

In order to validate the computational results and prior to analyzing the effect of CSRO on samples, it is necessary to investigate the crystal structure and the phases existing in the alloys. Therefore, the XRD measurement results acquired from H1 and H2 samples at room temperature are presented in Figure 3.12. a and b, respectively. The samples utilized here were rectangular, which made rotation and oscillation of the samples possible during measurements. The oscillation and rotation of samples are essential as they allow for collecting signals from a higher number of grains and orientations. Therefore, the results here are expected to include most of the peaks in these materials. The peaks acquired from the H1 samples are related to BCC structure, and heat treatment did not cause a significant effect on the acquired peaks from the H1 samples.

On the other hand, XRD results acquired from the H2 As-cast sample (Figure 3.12 b) show peaks from two BCC phases and an HCP phase. Several other works have reported these structures in the HfNbTaTiZr and similar alloys, which are considered a side effect of the cooling rate in the VAR casting method [17, 136]. On the other hand, the results acquired from the H2-HT sample show the dissolution of the hcp phases. In addition, the BCC1 and BCC2 phase (110) peaks are sharper.

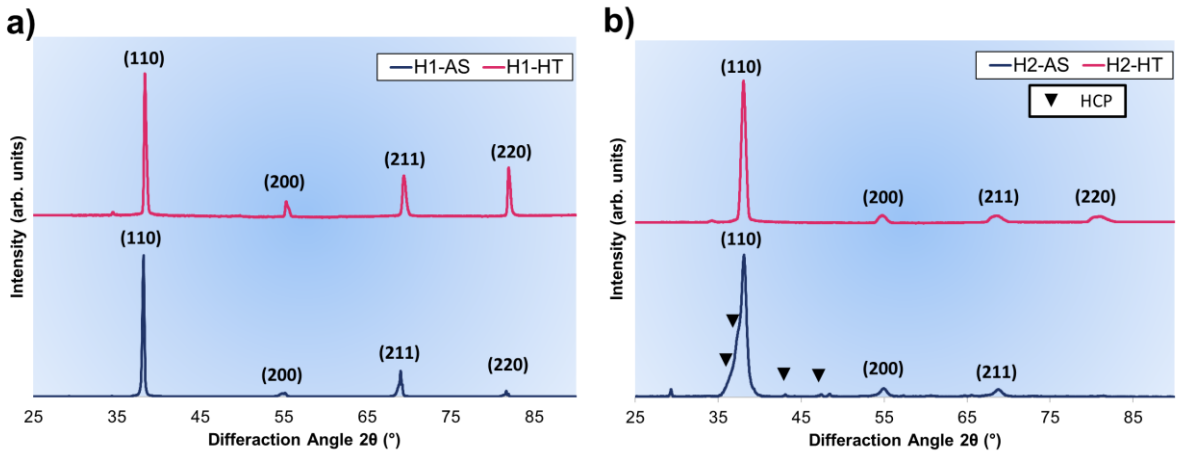

Figure 3.12 a) XRD measurement of As-cast (AS) and heat treated (HT) of H1 sample. b) Similar results for H2 samples. Notably, the AS-cast results are from a previous work [21].

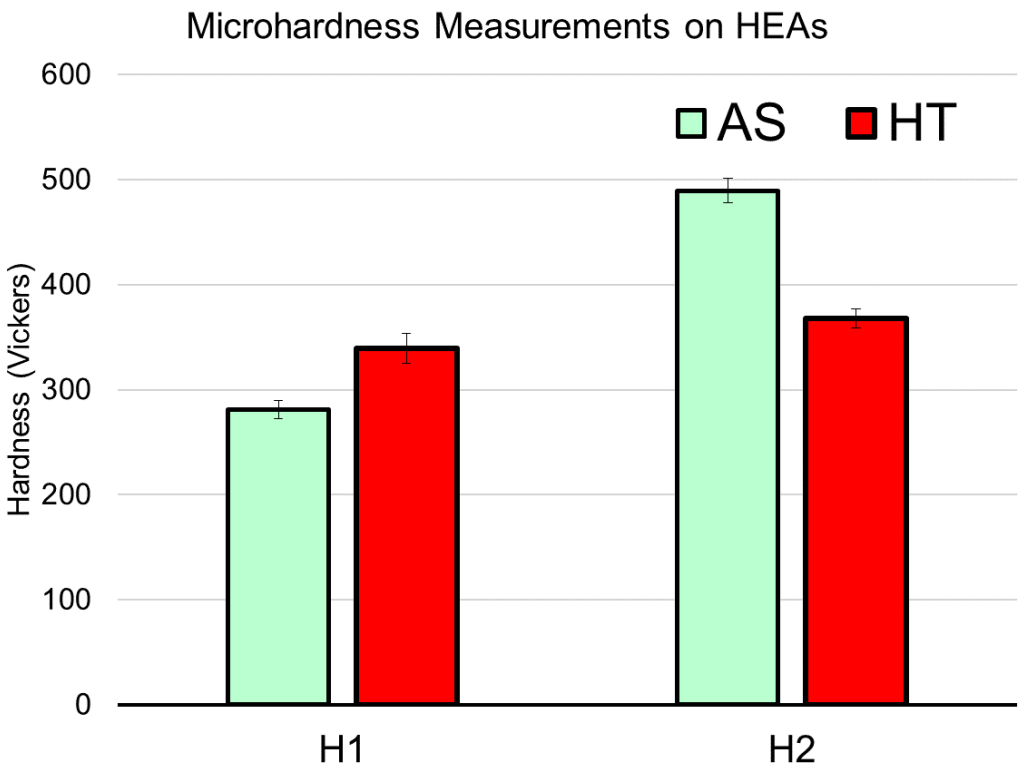

Figure 3.13 The microhardness measurement performed on H1 and H2 samples in both As-cast (AS) and heat-treated (HT) conditions.

Microhardness measurements were performed to assess the effect of the prolonged heat treatment process on the hardness of H1 and H2 samples, and the results are presented in Figure 3.13. As can be seen, two distinct behaviors were observed. Heat treatment on the H1 sample caused an increase in the hardness of the sample, while the hardness in the H2 samples was reduced by approximately 20%. As the microhardness measurements were performed under a microscope, the measurements were conducted on areas within the grains. Therefore, the increase in the hardness of the H1 sample is attributed to the dissolution of dendritic arms and formation of CSRO in these samples. On the other hand, the decrease in the hardness of the H2 sample is attributed to the dissolution of the hard HCP phases, as supported by the XRD measurements in Figure 3.12 b).

For two reasons, the further validation was focused only on the H1 samples: 1) The existence of the HCP phase in the H2 sample prevents isolation of the CSRO effect on the mechanical properties, and 2) the H2 alloy composition is extensively studied through experimental methods and a sufficient number of quality studies exist on this material.

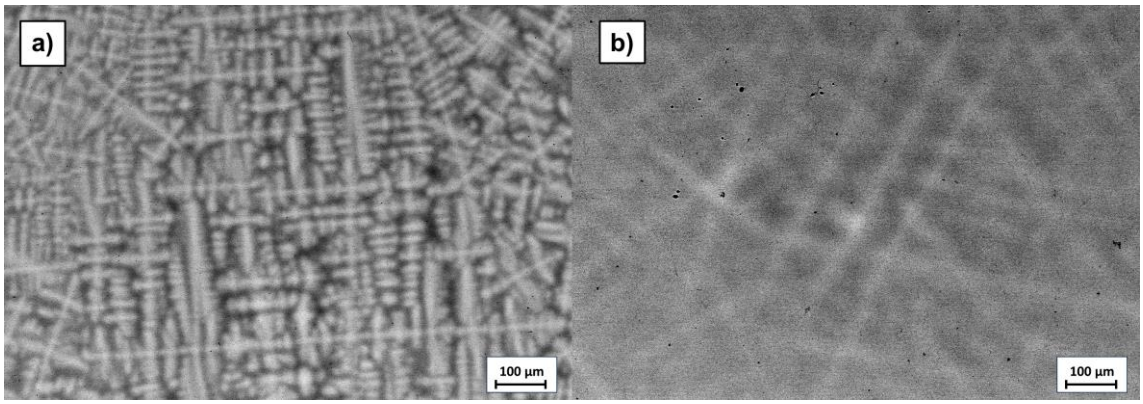

Figure 3.14 BSE image from the microstructure of a) H1-AS and b) H1-HT samples.

Figure 3.14 shows the microstructure of H1-AS and H1-HT samples. As can be seen, the microstructure of H1-AS is highly dendritic, which is a typical side effect of the cooling rates in the VAR method. The line-scan EDX measurement performed on the dendritic arms (not shown here) showed that the arms are Ta and Nb rich, while the interdendritic region is Ti and Hf rich. This is an expected solidification behavior, as Ta and Nb both have higher melting points than Hf and Ti and solidify earlier and form the dendrites. After heat treatment, the extent of the dendrites decreased significantly. However, traces of them still exist in the samples. The persistence of dendrites after such a long homogenization process suggests that the Ta and Nb combinations are thermodynamically favorable.

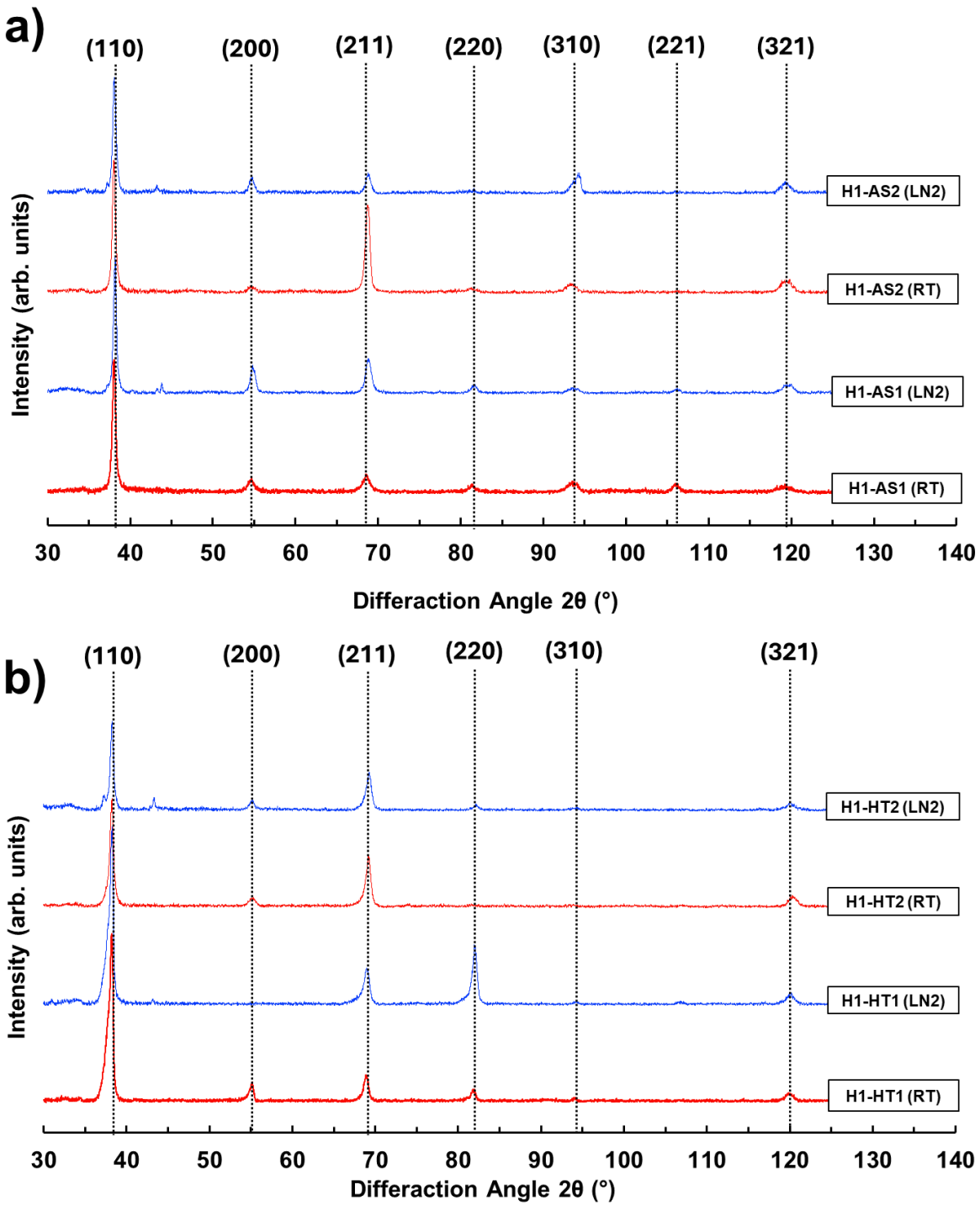

Figure 3.15 a) XRD measurement of two different As-cast H1 compression samples measured at room temperature (RT) and measured while immersed in liquid nitrogen (LN2). b) Similar results were obtained for heat-treated H1 samples.

Figure 3.15 shows the results of XRD measurements on the compression samples (prior to compression) at room temperature and while they were immersed in Liquid nitrogen (LN2). The measurements were done on two different samples to consider the possibility

of sample variation in the results, as the rotation and oscillation of samples were not possible in this setup. As shown in Figure 3.15 a, the H1-AS samples at room temperature are made of a single bcc phase. However, after cooling them down via LN2, small hcp peaks appeared in the samples. Performing a similar experiment on the heat-treated H1 samples is provided in Figure 3.15 b., which recommends two changes in the samples. First, the samples have wider (110) peaks that are related to the formation of B2 ordering in the material and is evidence for the formation of CSROs. Second, the cooling down of the heat-treated samples causes some minor HCP peaks in the samples, which suggests the formation of a small amount of temperature-induced martensite phases in the alloy. However, no visual evidence of such temperature-induced transformation was observed in SEM images taken at cryogenic temperatures, suggesting the small size and amount of these phases.

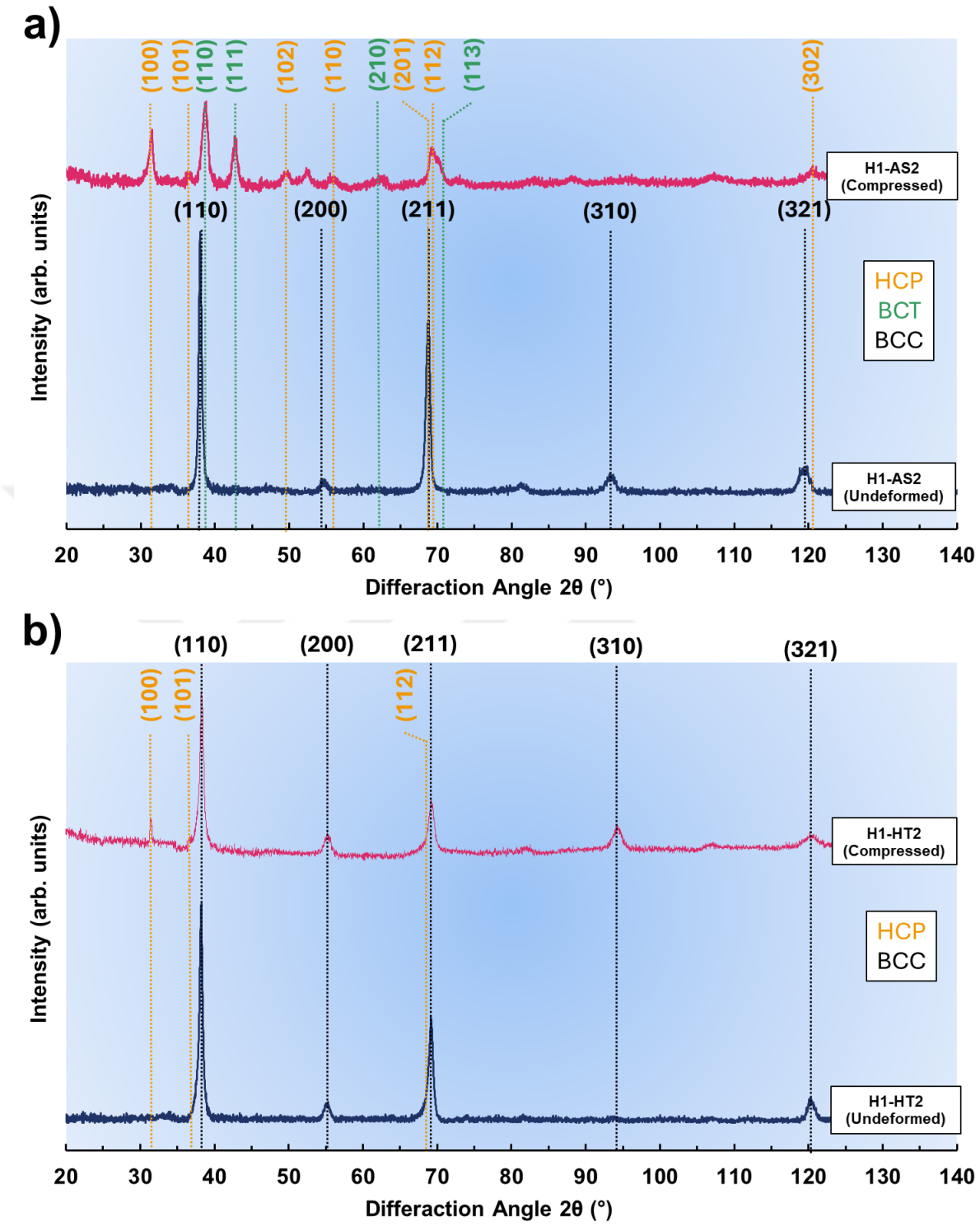

Figure 3.16 XRD measurements performed on H1 samples in both AS and HT states before and after compression at room temperatures.

In order to observe the effects of compression on the samples and understand their potential phase transformation, H1-AS and H1-HT samples were compressed using a compression module, and the results are provided in Figure 3.16. Figure 3.16 shows that

the compression experiment caused a significant change in the H1-AS sample; one HCP phase and one Body Centered tetragonal (BCT) phase were formed in these samples, suppressing the signals acquired from the BCC phase. On the other hand, Figure 3.16 b shows that even after such a high degree of compression, minor HCP peaks are formed, and the BCC phase is maintained. This suggests that the heat treatment performed on the sample stabilized the BCC phase which is an indirect sign for the formation of CSRO in this alloy.

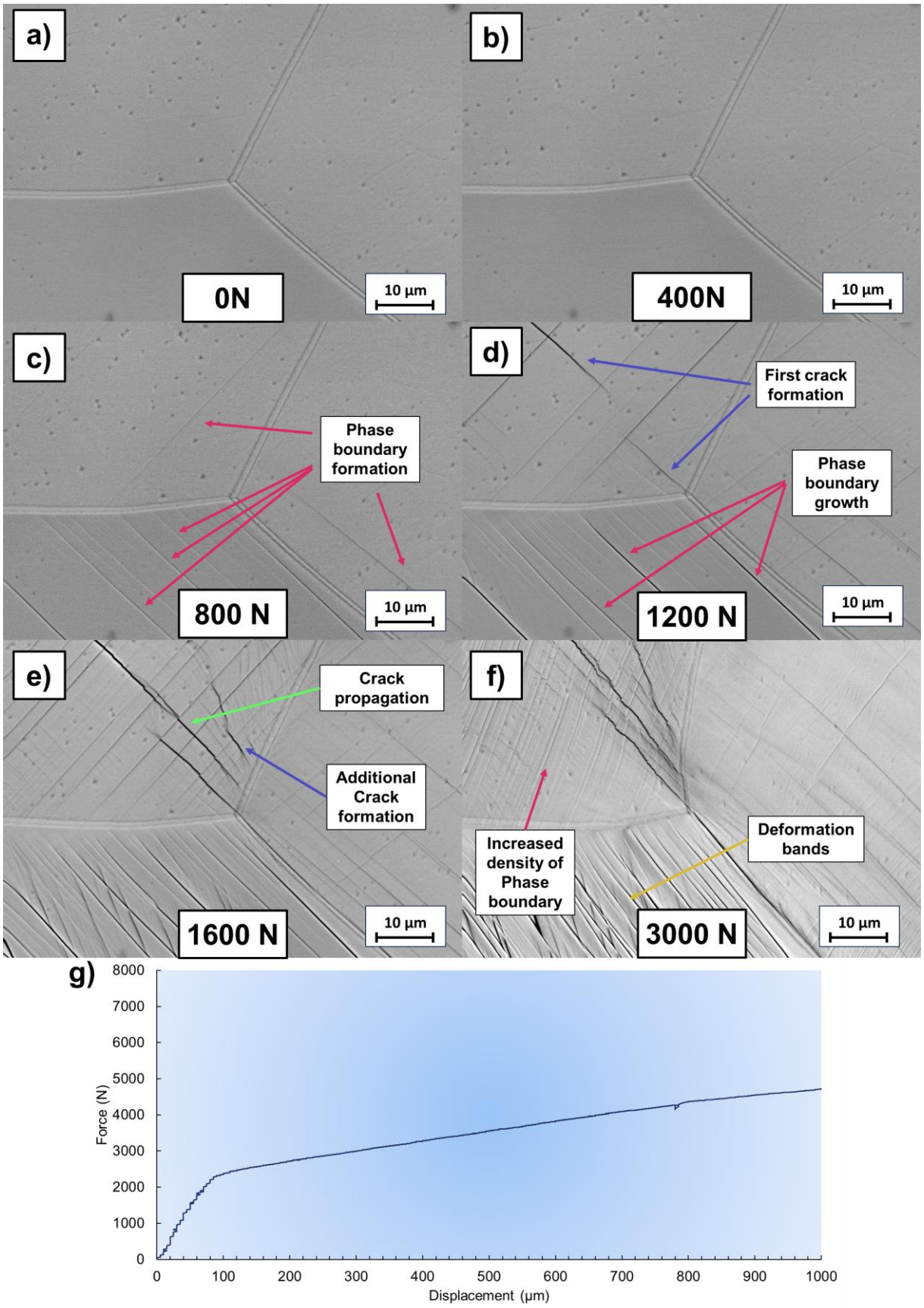

Figure 3.17 Back-scattered electron (BSE) images from the H1-AS sample under compression load of a) 0, b) 400N, c) 800N, d) 1200N, e) 1600N, and e) 3000N. g) The

force versus displacement curve of the compressed sample.

In order to gain a better understanding of the microstructure and phase transformations during compression, samples were compressed inside the SEM using a compression module, with results presented in Figures 3.17 and 3.19 for H1-AS and H1-HT. In Figure 3.17 a and b, no transformation is visible. However, with an increase of the force to 800N, phase boundaries form inside grains, as shown in Figure 3.17 c. Further increase in the force to 1200N causes the formation of first cracks in samples. Additional force to 1600N increases the density of phase boundaries and propagates the previously formed cracks. The material up to approximately 2500N (Yielding, Figure 3.17 g) shows jagged line behavior, which can be attributed to the competition between the cracks and phase boundaries forming to release the energy. In addition, this behavior can be attributed to the twinning inside the material. Further increase results in the plastic deformation and appearance of deformation bands and higher density of phase boundaries (Figure 3.17 f).

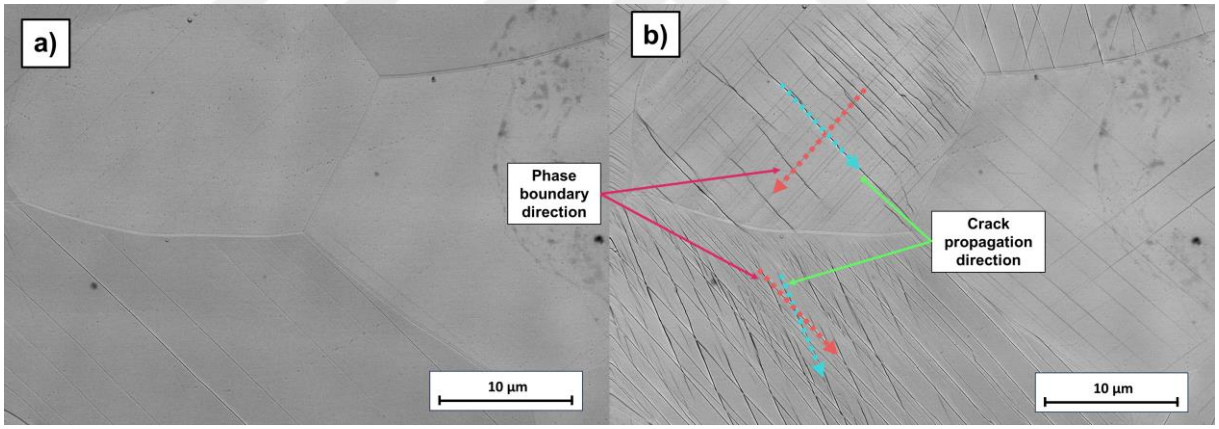

Figure 3.18 BSE images of H1-AS samples with smaller magnification, a) showing the sample before the formation of cracks at 800N force and b) the sample after the formation of significant phase boundaries and cracks at 1600N.

Figure 3.18 shows a lower magnification view of Figure 3.17. As can be seen, there is no relation between the phase boundary and crack initiation direction. Therefore, it is reasonable to say that the phase boundaries do not provide a weak point for the nucleation of cracks. In fact, the cracks in the upper side of Figure 3.18 b are perpendicular to the phase boundaries and pass through them without changing the direction of cracks.

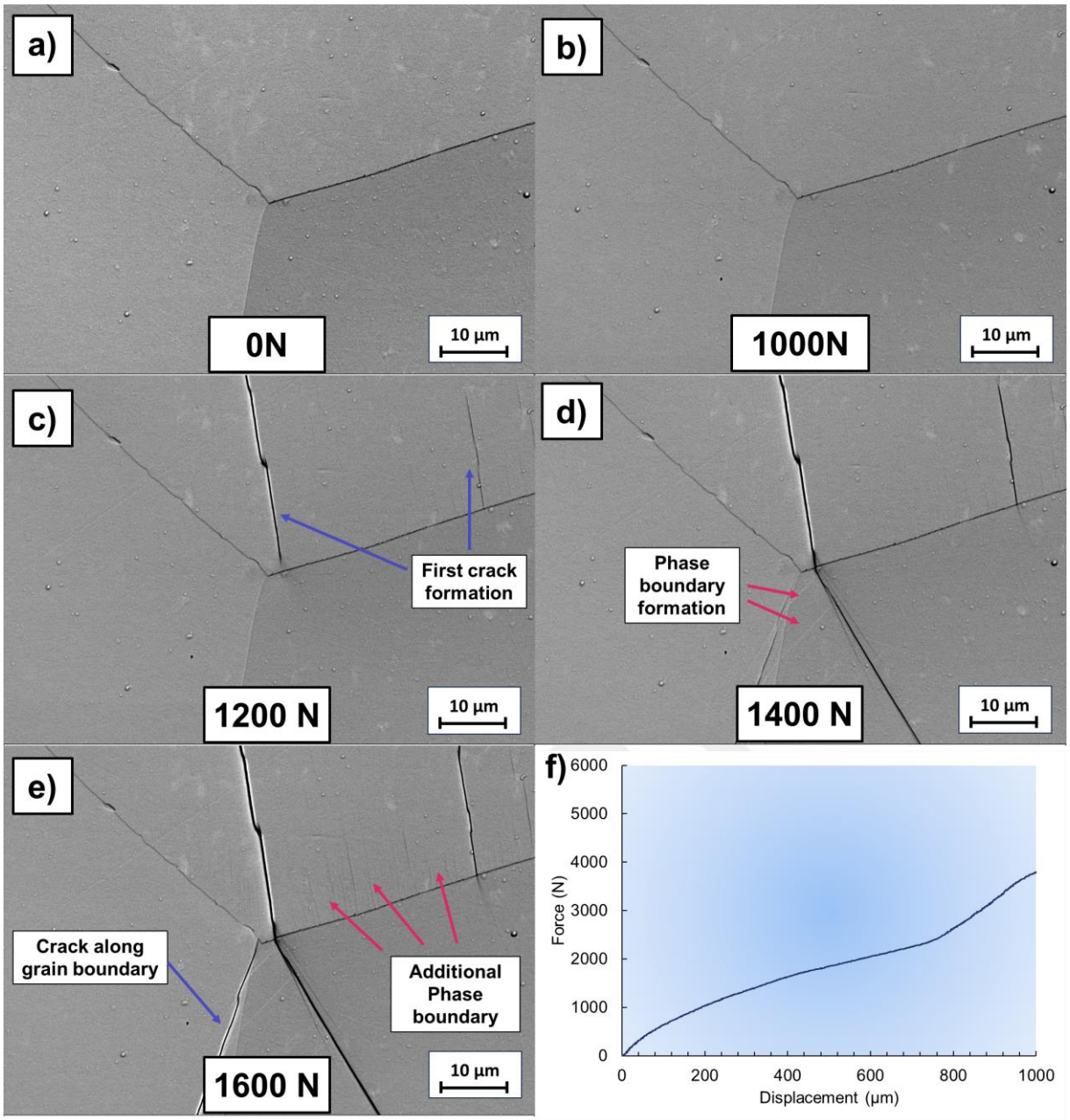

Figure 3.19 Back-scattered electron (BSE) images from the H1-HT sample under compression load of a) 0, b) 1000N, c) 1200N, d) 1400N, and e) 1600N. f) The force versus displacement curve of the compressed sample.

The evolution of the H1-HT sample under compression is provided in Figure 3.19. As can be seen, the first feature appearing in the H1-HT sample was cracks forming at 1200N (Figure 3.19 c). However, a further increase in the force initiated minor phase boundaries to form (Figure 3.19 d). With additional force, more phase boundaries appeared. However, at this point, cracks appeared on the grain boundaries and caused failure of the grains. Comparing Figure 3.17 g and 3.19 f, one can see that the deformation in the H1-

HT follows a different path, with the sample losing its overall strength due to the failure of grain boundaries.

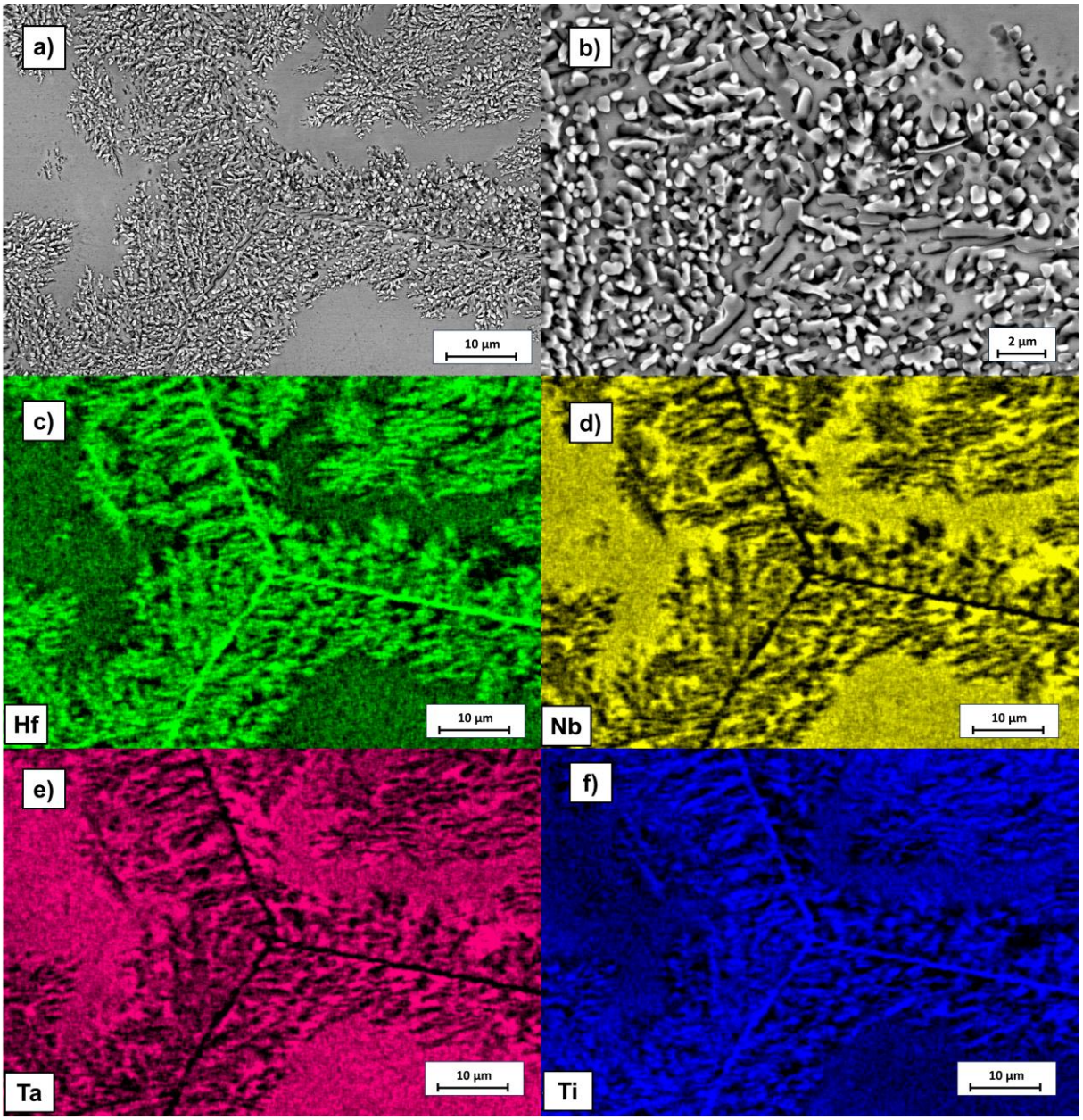

Figure 3.20 a) BSE image of the grain boundaries after ion polishing in the H1-HT sample. b) higher magnification of 3.20 a figure. c-f) The EDX impulse mapping of the H1-HT sample for Hf, Nb, Ta, Ti.

In order to understand the reason behind the early failure of H1-HT in the compression experiment, the composition of the grain boundaries of H1-HT was investigated via EDX mapping after ion-polishing the sample. As can be seen, after the ion-polishing, certain

phases are exposed around the grain boundaries (Figure 3.20 a and b). These phases and the grain boundary line are rich in Ti and Hf, while the other parts are deficient in these elements. Therefore, one can attribute the early failure of material along its grain boundary to the harder compositions forming in these regions.

3.5 Discussion

The initial hypothesis in this work was that the formation of CSROs in the RHEAs of the Senkov family can enhance the mechanical properties of these alloys. The computational results for a perfect single crystal showed that the formation of CSROs in the H1 and H2 alloys is mainly in two groups of Ta-Nb and Hf-Ti (H1) and Hf-Ti-Zr (H2). The formation of such CSROs is supported by the XRD results showing a single-phase crystal structure after the prolonged heat treatment. Additional support for this idea can be the persistence of dendritic arms in the H1-HT sample even after such a long heat treatment, suggesting the thermodynamic preference of Nb-Ta and Hf-Ti-rich regions. Subsequently, the mechanical effect of the CSRO formation was simulated by MD simulations, suggesting the hardening effect of CSRO on the alloys. In addition to hardening, it is possible to see that the formation of CSRO mostly suppressed the twinning effect in the H1-AS alloy at 300K. The increase in the hardness of the H1 alloy after the formation of CSRO is supported by the microhardness measurements, and the twinning effect also disappeared in the compression H1-HT sample. This result matches an experimental work on the HfNbTaTiZr single crystal that suggested that the formation of CSROs hinders the twinning because these regions require additional energy (stress) for twinning formation [137]. In addition to twinning, MD simulations showed that the CSROs made Deformation-induced phase transformation (DIPT) more difficult. This idea can be supported by comparing the XRD results of the H1-AS and H1-Ht compressed samples. In these samples, the heat treatment stabilized the BCC phase and suppressed the formation of BCT phase and minimized the transformation to HCP. This result is supported by the work mentioned above on the HfNbTaTiZr single crystal that showed the deformation-induced ω phase was minimized due to the formation of CSROs [137]. Although the CSROs stabilized the alloys and caused additional hardness in the materials, their positive effect was affected by the formation of Hf-Ti-rich compounds around the grain boundary, resulting in the failure of the material at those points prior to the failure of the grains. The failure due to grain boundary is also supported by the shape of the

force-displacement curve that shows an insignificant amount of elastic region, which is attributed to the weak cohesive zone around the grain boundaries [138]. Therefore, it is reasonable to suggest that although the RHEAs forming CSROs at high temperatures can benefit from the strength increase within the grains, additional effort should be put into enhancing grain boundary strength to prevent the failure of materials. In addition, MC and MD simulations showed that at 1273K, the CSRO formation provided the possibility of twinning, which can be due to the destabilization of the alloy and the decrease in its stacking fault energy. However, such a claim should be validated via further experimental works.

3.6 Conclusion

In this work, the effect of the formation of chemical short-range order (CSRO) on the room temperature and high-temperature mechanical properties of two refractory high entropy alloys (RHEAs) of $HfNbTaTi_3$ (H1) and HfNbTaTiZr (H2) was investigated using atomistic simulations. To be more specific, Monte Carlo simulations were used to find the thermodynamically stable configuration of atoms. Subsequently, compression simulations were performed on the systems at 300K, showing that the random state of the H1 sample undergoes a BCC to HCP transformation and a twinning formation due to compression. However, the formation of CSROs results in material hardening and diminishing the deformation-induced transformation. In the H2 system, a similar effect of CSROs was observed. In higher temperatures, the effect of CSRO in the H1 system was reversed, causing twinning and additional ductility. While the H2 system had a minor hardening effect caused by the formation of CSROs.

In order to validate the results, H1 and H2 samples were produced via the vacuum arc melting (VAR) method, and the samples were heat treated at 1000 °C for 72 hours to allow the formation of CSROs. The X-ray diffraction (XRD) measurements showed that the H1 sample forms a BCC structure, while the H2 sample forms two BCCs and one HCP phase in as-cast form and 2 BCCs after heat treatment. Therefore, isolating the CSRO effect in the H2 samples was not possible. This idea was supported by the fact that the hardness of the H2 sample decreased after heat treatment due to dissolution of the HCP phase. Further investigation of H1 samples showed that the hardness of these materials increased as a result of the formation of CSRO and phase analysis via XRD after compression showed that CSROs significantly suppressed the BCC to HCP phase

transformation and hindered the formation of BCT phase. Compression experiments also showed that the formation of CSROs, although it increases the hardness of grains, causes the grain boundaries to be the point of failure for the materials. Therefore, the results of this work suggest that in order to utilize the full potential of the CSROs in RHEAs at both room and high temperatures, it is necessary to optimize the grain boundaries of the alloys for enhanced high-temperature properties.

Chapter 4:
CONCLUSIONS

Considering the great potential of refractory high entropy alloys (RHEAs) in high-temperature applications, two aspects of the high-temperature property of these alloys were investigated. After a brief introduction to the fundamentals of the high entropy alloys, oxidation properties of metallic alloys, and atomistic simulations, a chapter was dedicated to the oxidation properties of RHEAs. To be more specific, four alloys of $HfNbTaTi_3$, HfNbTaTiZr, HfMoTaTiZr, and NbMoTaTiZr underwent static oxidation experiments to shed light on the mechanism of oxidations in these alloys. To do so, various analysis methods, such as X-ray diffraction (XRD), X-ray photon spectrometry (XPS), and scanning electron microscopy (SEM) were performed on the samples. To understand the effect of crystallinity on the samples, an amorphous coating of the NbMoTaTiZr was produced using physical vapor deposition (PVD). The results of these investigations showed three different mechanisms in the studied alloys:

1) Formation of a non-protective oxide layer on the surface
2) Volatilization of Mo and pesting of the alloys
3) Significantly different oxidation response of the amorphous coating

In addition, the effect of different elements was discussed, showing that some of the elements (such as Nb and Ta) have the potential to form oxides with a high Pilling-Bedworth ratio that can cause severe stress in the oxide layer. On the other hand, some elements, such as Hf and Zr, cause internal oxidation. Overall, the results of this chapter could shed light on the mechanism of oxidation in the studied RHEAs.

In the third chapter, the formation of chemical short-range order (CSRO) and its effect on the mechanical properties was investigated in two alloys of $HfNbTaTi_3$ and HfNbTaTiZr. The motivation for choosing CSROs as the topic of this study was their effect on the strength of the materials at high temperatures. To conduct the study, the Monte Carlo atomistic simulations were conducted on random configuration of atoms, and the formation of CSROs was investigated. Subsequently, these systems underwent molecular dynamics compression simulations under different strain rates, temperatures, and system sizes. The results of these simulations suggested the strengthening role of CSROs in these alloys. In addition, these simulations predicted a deformation-induced phase transformation, which was affected by the formation of

CSROs.

In order to validate these results, in-situ compression experiments under SEM, XRD, and microhardness measurements were conducted on As-cast and heat-treated samples. The microhardness measurements pointed out the formation of CSROs in the $HfNbTaTi_3$ alloy, and the compression experiments proved the BCC to HCP deformation-induced phase transformation in As-cast samples. Moreover, it was observed that the CSRO suppresses the deformation-induced transformation as suggested by MD simulation. In addition, the effect of CSRO formation on the weakening of the grain boundaries was observed, causing the failure of the samples from that region. As a result, to enhance the high-temperature properties of RHEAs, the formation of CSROs can be utilized as a new tool, while additional effort should be made to optimize the grain boundary properties in these alloys.

Overall, the results and the discussions made in this work aimed to deepen the knowledge of the high-temperature properties of RHEAs. In particular, the results recommend that additional effort be put into optimizing the compositions of the alloys to have a better capacity to form a dense and thin oxide layer while forming CSROs to enhance their strength. On the other hand, considerations should be made to prevent weakening the grain boundary due to the formation of CSROs in these regions. Therefore, a long journey is ahead to utilize the full potential of RHEAs in high-temperature applications.

BIBLIOGRAPHY

[1] B. Cantor, I.T.H. Chang, P. Knight, A.J.B. Vincent, Microstructural development in equiatomic multicomponent alloys, Materials Science and Engineering: A, 375-377 (2004) 213-218.

[2] J.W. Yeh, S.K. Chen, S.J. Lin, J.Y. Gan, T.S. Chin, T.T. Shun, C.H. Tsau, S.Y. Chang, Nanostructured High-Entropy Alloys with Multiple Principal Elements: Novel Alloy Design Concepts and Outcomes, Advanced Engineering Materials, 6 (2004) 299-303.

[3] J. Chen, X. Zhou, W. Wang, B. Liu, Y. Lv, W. Yang, D. Xu, Y. Liu, A review on fundamental of high entropy alloys with promising high–temperature properties, Journal of Alloys and Compounds, 760 (2018) 15-30.

[4] A.M. Manzoni, U. Glatzel, New multiphase compositionally complex alloys driven by the high entropy alloy approach, Materials Characterization, 147 (2019) 512-532.

[5] Z. Tang, O.N. Senkov, C.M. Parish, C. Zhang, F. Zhang, L.J. Santodonato, G. Wang, G. Zhao, F. Yang, P.K. Liaw, Tensile ductility of an AlCoCrFeNi multi-phase high-entropy alloy through hot isostatic pressing (HIP) and homogenization, Materials Science and Engineering: A, 647 (2015) 229-240.

[6] Y. Zou, S. Maiti, W. Steurer, R. Spolenak, Size-dependent plasticity in an Nb25Mo25Ta25W25 refractory high-entropy alloy, Acta Materialia, 65 (2014) 85-97.

[7] F.J. Wang, Y. Zhang, G.L. Chen, Atomic packing efficiency and phase transition in a high entropy alloy, Journal of Alloys and Compounds, 478 (2009) 321-324.

[8] I. Toda-Caraballo, J.S. Wróbel, S.L. Dudarev, D. Nguyen-Manh, P.E.J. Rivera-Díaz-del-Castillo, Interatomic spacing distribution in multicomponent alloys, Acta Materialia, 97 (2015) 156-169.

[9] L.R. Owen, E.J. Pickering, H.Y. Playford, H.J. Stone, M.G. Tucker, N.G. Jones, An assessment of the lattice strain in the CrMnFeCoNi high-entropy alloy, Acta Materialia, 122 (2017) 11-18.

[10] J. Dąbrowa, M. Zajusz, W. Kucza, G. Cieślak, K. Berent, T. Czeppe, T. Kulik, M. Danielewski, Demystifying the sluggish diffusion effect in high entropy alloys, Journal of Alloys and Compounds, 783 (2019) 193-207.

[11] J. Zhang, C. Gadelmeier, S. Sen, R. Wang, X. Zhang, Y. Zhong, U. Glatzel, B. Grabowski, G. Wilde, S.V. Divinski, Zr diffusion in BCC refractory high entropy alloys: A case of ‘non-sluggish’ diffusion behavior, Acta Materialia, 233 (2022).

[12] M.S. Daw, M. Chandross, Sluggish diffusion in random equimolar FCC alloys, Physical Review Materials, 5 (2021).

[13] B.X. Cao, C. Wang, T. Yang, C.T. Liu, Cocktail effects in understanding the stability and properties of face-centered-cubic high-entropy alloys at ambient and cryogenic temperatures, Scripta Materialia, 187 (2020) 250-255.

[14] O.N. Senkov, J.M. Scott, S.V. Senkova, D.B. Miracle, C.F. Woodward, Microstructure and room temperature properties of a high-entropy TaNbHfZrTi alloy, Journal of Alloys and Compounds, 509 (2011) 6043-6048.

[15] J.X. Fang, J.X. Wang, Y.J. Wang, H.T. He, D.B. Zhang, Y. Cao, Microstructure evolution and deformation behavior during stretching of a compositionally inhomogeneous TWIP-TRIP cantor-like alloy by laser powder deposition, Materials Science and Engineering: A, 847 (2022).

[16] S. Chen, H.S. Oh, B. Gludovatz, S.J. Kim, E.S. Park, Z. Zhang, R.O. Ritchie, Q. Yu, Real-time observations of TRIP-induced ultrahigh strain hardening in a dual-phase CrMnFeCoNi high-entropy alloy, Nat Commun, 11 (2020) 826.

[17] O.N. Senkov, S.L. Semiatin, Microstructure and properties of a refractory high-entropy alloy after cold working, Journal of Alloys and Compounds, 649 (2015) 1110-1123.

[18] Engineering Steels and High Entropy-Alloys, in, IntechOpen, Rijeka, 2020.

[19] S. Gurel, M.B. Yagci, B. Bal, D. Canadinc, Corrosion behavior of novel Titanium-based high entropy alloys designed for medical implants, Materials Chemistry and Physics, (2020) 123377-123377.

[20] A. Motallebzadeh, N.S. Peighambardoust, S. Sheikh, H. Murakami, S. Guo, D. Canadinc, Microstructural, mechanical and electrochemical characterization of TiZrTaHfNb and Ti1.5ZrTa0.5Hf0.5Nb0.5 refractory high-entropy alloys for biomedical applications, Intermetallics, 113 (2019) 106572-106572.

[21] S. Gurel, A. Nazarahari, D. Canadinc, H. Cabuk, B. Bal, Assessment of biocompatibility of novel TiTaHf-based high entropy alloys for utility in orthopedic implants, in: Materials Chemistry and Physics, Elsevier B.V., 2021, pp. 124573.

[22] H.C. Ozdemir, A. Nazarahari, B. Yilmaz, U. Unal, H.J. Maier, D. Canadinc, E. Bedir, R. Yilmaz, Understanding the enhanced corrosion performance of two novel Ti-based biomedical high entropy alloys, Journal of Alloys and Compounds, (2023).

[23] S. Gurel, M.B. Yagci, D. Canadinc, G. Gerstein, B. Bal, H.J. Maier, Fracture behavior of novel biomedical Ti-based high entropy alloys under impact loading, Materials Science and Engineering: A, 803 (2021) 140456-140456.

[24] H.C. Ozdemir, E. Bedir, R. Yilmaz, M.B. Yagci, D. Canadinc, Machine learning-assisted design of biomedical high entropy alloys with low elastic modulus for orthopedic implants, in: Journal of Materials Science, 2022.

[25] Y. Noyama, T. Miura, T. Ishimoto, T. Itaya, M. Niinomi, T. Nakano, Bone Loss and Reduced Bone Quality of the Human Femur after Total Hip Arthroplasty under Stress-Shielding Effects by Titanium-Based Implant, Materials Transactions, 53 (2012) 565-570.

[26] O.N.N. Senkov, G.B.B. Wilks, D.B.B. Miracle, C.P.P. Chuang, P.K.K. Liaw, Refractory high-entropy alloys, Intermetallics, 18 (2010) 1758-1765.

[27] O.N. Senkov, D.B. Miracle, K.J. Chaput, J.P. Couzinie, Development and exploration of refractory high entropy alloys—A review, Journal of Materials Research 2018 33:19, 33 (2018) 3092-3128.

[28] O.N. Senkov, D.B. Miracle, K.J. Chaput, J.P. Couzinie, Development and exploration of refractory high entropy alloys - A review, in, Cambridge University Press, 2018, pp. 3092-3128.

[29] S.K. Dewangan, A. Mangish, S. Kumar, A. Sharma, B. Ahn, V. Kumar, A review on High-Temperature Applicability: A milestone for high entropy alloys, Engineering Science and Technology, an International Journal, 35 (2022).

[30] O.U. Tukac, A. Ozalp, E. Aydogan, Development and thermal stability of Cr10Mo25Ta25Ti15V25 refractory high entropy alloys, Journal of Alloys and Compounds, 930 (2023).

[31] B.X. Cao, T. Yang, L. Fan, J.H. Luan, Z.B. Jiao, C.T. Liu, Refractory alloying additions on the thermal stability and mechanical properties of high-entropy alloys, Materials Science and Engineering: A, 797 (2020).

[32] S. Sheikh, M.K. Bijaksana, A. Motallebzadeh, S. Shafeie, A. Lozinko, L. Gan, T.-K.K. Tsao, U. Klement, D. Canadinc, H. Murakami, S. Guo, Accelerated oxidation in ductile refractory high-entropy alloys, Intermetallics, 97 (2018) 58-66.

[33] S. Sheikh, L. Gan, T.-K. Tsao, H. Murakami, S. Shafeie, S. Guo, Aluminizing for enhanced oxidation resistance of ductile refractory high-entropy alloys, Intermetallics, 103 (2018) 40-51.

[34] N. Birks, G.H. Meier, F.S. Pettit, Introduction to the High-Temperature Oxidation of Metals, Cambridge University Press, Cambridge, 2006.

[35] P. Kofstad, High temperature corrosion, Elsevier Applied Science Publishers, Crown House, Linton Road, Barking, Essex IG 11 8 JU, UK, 1988., (1988).

[36] G.R. Wallwork, The oxidation of alloys, Reports on Progress in Physics, 39 (1976) 401-485.

[37] G.C. Wood, F.H. Stott, Oxidation of alloys, Materials Science and Technology, 3 (2016) 519-530.

[38] J.S. Wang, A.G. Evans, Measurement and analysis of buckling and buckle propagation in compressed oxide layers on superalloy substrates, Acta Materialia, 46 (1998) 4993-5005.

[39] H.E. Evans, Stress effects in high temperature oxidation of metals, International Materials Reviews, 40 (2013) 1-40.

[40] C. Xu, W. Gao, Pilling-Bedworth ratio for oxidation of alloys, Materials Research Innovations, 3 (2000) 231-235.

[41] D.V. Malakhov, Pilling–Bedworth Ratio for Homogeneous Alloys: A Physically Sound Practical Generalization, Metallurgical and Materials Transactions B, 54 (2023) 1174-1180.

[42] M.M. Nagl, W.T. Evans, The mechanical failure of oxide scales under tensile or compressive load, Journal of Materials Science, 28 (1993) 6247-6260.

[43] G.H. Meier, K. Jung, N. Mu, N.M. Yanar, F.S. Pettit, J. Pirón Abellán, T. Olszewski, L. Nieto Hierro, W.J. Quadakkers, G.R. Holcomb, Effect of Alloy Composition and Exposure Conditions on the Selective Oxidation Behavior of Ferritic Fe–Cr and Fe–Cr–X Alloys, Oxidation of Metals, 74 (2010) 319-340.

[44] L. Garcia-Fresnillo, J.M. Alvarado-Orozco, G.H. Meier, Influence of Alloy Composition and Exposure Conditions on the Selective Oxidation Behavior of Ni–Al Alloys, Oxidation of Metals, 88 (2017) 327-338.

[45] J. Young, Chapter 6 Oxidation of Alloys II: Internal Oxidation, in: D.J. Young (Ed.) Corrosion Series, Elsevier Science, 2008, pp. 247-314.

[46] H.W. Pickering, On the Transition from Internal to External Oxidation in Ternary Alloys, Journal of The Electrochemical Society, 119 (1972).

[47] L. Qin, Y. Pei, S. Li, X. Zhao, S. Gong, H. Xu, Role of volatilization of molybdenum oxides during the cyclic oxidation of high-Mo containing Ni-based single crystal superalloys, Corrosion Science, 129 (2017) 192-204.

[48] C.S. Tedmon, The Effect of Oxide Volatilization on the Oxidation Kinetics of Cr and Fe-Cr Alloys, Journal of The Electrochemical Society, 113 (1966).
[49] R. de Borst, Challenges in computational materials science: Multiple scales, multi-physics and evolving discontinuities, Computational Materials Science, 43 (2008) 1-15.
[50] A. Borrelli, J. Wellmann, Computer Simulations Then and Now: an Introduction and Historical Reassessment, NTM, 27 (2019) 407-417.
[51] D. Frenkel, B. Smit, Understanding molecular simulation: from algorithms to applications, Academic Press San Diego, 2002.
[52] S. Plimpton, Computational limits of classical molecular dynamics simulations, Computational Materials Science, 4 (1995) 361-364.
[53] B. Sadigh, P. Erhart, A. Stukowski, A. Caro, E. Martinez, L. Zepeda-Ruiz, Scalable parallel Monte Carlo algorithm for atomistic simulations of precipitation in alloys, Physical Review B, 85 (2012).
[54] K. Sargsyan, C. Grauffel, C. Lim, How Molecular Size Impacts RMSD Applications in Molecular Dynamics Simulations, J Chem Theory Comput, 13 (2017) 1518-1524.
[55] I.-C. Yeh, G. Hummer, System-Size Dependence of Diffusion Coefficients and Viscosities from Molecular Dynamics Simulations with Periodic Boundary Conditions, The Journal of Physical Chemistry B, 108 (2004) 15873-15879.
[56] A.P. Thompson, H.M. Aktulga, R. Berger, D.S. Bolintineanu, W.M. Brown, P.S. Crozier, P.J. in 't Veld, A. Kohlmeyer, S.G. Moore, T.D. Nguyen, R. Shan, M.J. Stevens, J. Tranchida, C. Trott, S.J. Plimpton, LAMMPS - a flexible simulation tool for particle-based materials modeling at the atomic, meso, and continuum scales, in: Computer Physics Communications, North-Holland, 2022, pp. 108171.
[57] E.P. George, W.A. Curtin, C.C. Tasan, High entropy alloys: A focused review of mechanical properties and deformation mechanisms, Acta Materialia, 188 (2020) 435-474.
[58] E.P. George, D. Raabe, R.O. Ritchie, High-entropy alloys, Nature Reviews Materials 2019 4:8, 4 (2019) 515-534.
[59] W. Xiong, A.X.Y. Guo, S. Zhan, C.-T. Liu, S.C. Cao, Refractory high-entropy alloys: A focused review of preparation methods and properties, Journal of Materials Science & Technology, 142 (2023) 196-215.
[60] D.B. Miracle, O.N. Senkov, A critical review of high entropy alloys and related concepts, Acta Materialia, 122 (2017) 448-511.

[61] H.C. Ozdemir, E. Bedir, R. Yilmaz, M.B. Yagci, D. Canadinc, Machine learning-assisted design of biomedical high entropy alloys with low elastic modulus for orthopedic implants, Journal of Materials Science, 57 (2022) 11151-11169.
[62] D. Ouyang, Z.-j.j. Chen, H.-b.b. Yu, K.C.C. Chan, L. Liu, Oxidation behavior of the Ti38V15Nb23Hf24 refractory high-entropy alloy at elevated temperatures, Corrosion Science, 198 (2022) 110153-110153.
[63] Y. Wei, Y. Fu, Z.-m. Pan, Y.-c. Ma, H.-x. Cheng, Q.-c. Zhao, H. Luo, X.-g. Li, Y. Wei, Y. Fu, Z.-m. Pan, Y.-c. Ma, H.-x. Cheng, Q.-c. Zhao, H. Luo, X.-g. Li, Influencing factors and mechanism of high-temperature oxidation of high-entropy alloys: A review, International Journal of Minerals, Metallurgy and Materials, 28 (2021) 915-930.
[64] Z. Gronostajski, M. Kaszuba, M. Hawryluk, M. Zwierzchowski, A review of the degradation mechanisms of the hot forging tools, Archives of Civil and Mechanical Engineering, 14 (2014) 528-539.
[65] Z. Tong, H. Liu, J. Jiao, W. Zhou, Y. Yang, X. Ren, Laser additive manufacturing of CrMnFeCoNi high entropy alloy: Microstructural evolution, high-temperature oxidation behavior and mechanism, Optics & Laser Technology, 130 (2020).
[66] S. Gou, M. Gao, Y. Shi, S. Li, Y. Fang, X. Chen, H. Chen, W. Yin, J. Liu, Z. Lei, H. Wang, Additive manufacturing of ductile refractory high-entropy alloys via phase engineering, Acta Materialia, 248 (2023).
[67] S. Schellert, M. Weber, H.J. Christ, C. Wiktor, B. Butz, M.C. Galetz, S. Laube, A. Kauffmann, M. Heilmaier, B. Gorr, Formation of rutile (Cr,Ta,Ti)O2 oxides during oxidation of refractory high entropy alloys in Ta-Mo-Cr-Ti-Al system, Corrosion Science, 211 (2023).
[68] Y. Yan, K.A. McGarrity, D.J. Delia, C. Fekety, K. Wang, The oxidation-resistance mechanism of WTaNbTiAl refractory high entropy alloy, Corrosion Science, 204 (2022).
[69] X. Yang, Z. An, Y. Zhai, X. Wang, Y. Chen, S. Mao, X. Han, Effect of Al content on the thermal oxidation behaviour of AlHfMoNbTi high-entropy alloys analysed by in situ environmental TEM, Corrosion Science, 191 (2021).
[70] S. Sheikh, L. Gan, A. Ikeda, H. Murakami, S. Guo, Alloying effect on the oxidation behavior of a ductile Al0.5Cr0.25Nb0.5Ta0.5Ti1.5 refractory high-entropy alloy, Materials Today Advances, 7 (2020).
[71] J. Dąbrowa, G. Cieślak, M. Stygar, K. Mroczka, K. Berent, T. Kulik, M. Danielewski, Influence of Cu content on high temperature oxidation behavior of AlCoCrCuxFeNi high entropy alloys (x = 0; 0.5; 1), Intermetallics, 84 (2017) 52-61.

[72] S. Sheikh, L. Gan, A. Ikeda, H. Murakami, S. Guo, Alloying effect on the oxidation behavior of a ductile Al0.5Cr0.25Nb0.5Ta0.5Ti1.5 refractory high-entropy alloy, Materials Today Advances, 7 (2020) 100104-100104.

[73] S. Sheikh, L. Gan, X. Montero, H. Murakami, S. Guo, Forming protective alumina scale for ductile refractory high-entropy alloys via aluminizing, Intermetallics, 123 (2020).

[74] O.A. Waseem, H.J. Ryu, Combinatorial synthesis and analysis of AlxTayVz-Cr20Mo20Nb20Ti20Zr10 and Al10CrMoxNbTiZr10 refractory high-entropy alloys: Oxidation behavior, Journal of Alloys and Compounds, 828 (2020).

[75] S. Oswald, X-Ray Photoelectron Spectroscopy in Analysis of Surfaces, Encyclopedia of Analytical Chemistry, (2013).

[76] P.S. Bagus, E.S. Ilton, C.J. Nelin, The interpretation of XPS spectra: Insights into materials properties, Surface Science Reports, 68 (2013) 273-304.

[77] D.R. Baer, K. Artyushkova, C.R. Brundle, J.E. Castle, M.H. Engelhard, K.J. Gaskell, J.T. Grant, R.T. Haasch, M.R. Linford, C.J. Powell, A.G. Shard, P.M.A. Sherwood, V.S. Smentkowski, Practical Guides for X-Ray Photoelectron Spectroscopy (XPS): First Steps in planning, conducting and reporting XPS measurements, J Vac Sci Technol A, 37 (2019).

[78] J.P. Couzinié, G. Dirras, L. Perrière, T. Chauveau, E. Leroy, Y. Champion, I. Guillot, Microstructure of a near-equimolar refractory high-entropy alloy, Materials Letters, 126 (2014) 285-287.

[79] O.N. Senkov, J.M. Scott, S.V. Senkova, F. Meisenkothen, D.B. Miracle, C.F. Woodward, Microstructure and elevated temperature properties of a refractory TaNbHfZrTi alloy, Journal of Materials Science, 47 (2012) 4062-4074.

[80] G.T. Galyon, L. Palmer, An integrated theory of whisker formation: The physical metallurgy of whisker formation and the role of internal stresses, IEEE Transactions on Electronics Packaging Manufacturing, 28 (2005) 17-30.

[81] P. Zhang, Y. Zhang, Z. Sun, Spontaneous Growth of Metal Whiskers on Surfaces of Solids: A Review, Journal of Materials Science & Technology, 31 (2015) 675-698.

[82] F. Zhang, B. Zhang, X. Chen, X. Zhang, X. Zhu, H. Du, Computational simulation of voids formation and evolution in Kirkendall effect, Physica A: Statistical Mechanics and its Applications, 554 (2020).

[83] H. Yeom, B. Maier, G. Johnson, T. Dabney, M. Lenling, K. Sridharan, High temperature oxidation and microstructural evolution of cold spray chromium coatings on Zircaloy-4 in steam environments, Journal of Nuclear Materials, 526 (2019).

[84] M.K. Nowotny, T. Bak, J. Nowotny, Electrical Properties and Defect Chemistry of TiO2 Single Crystal. IV. Prolonged Oxidation Kinetics and Chemical Diffusion, The Journal of Physical Chemistry B, 110 (2006) 16302-16308.

[85] C.-H. Chang, M.S. Titus, J.-W. Yeh, Oxidation Behavior between 700 and 1300 °C of Refractory TiZrNbHfTa High-Entropy Alloys Containing Aluminum, Advanced Engineering Materials, 20 (2018) 1700948-1700948.

[86] M. Gashti, R.M. Aghdam, A. Motallebzadeh, F.G. Asl, R. Soltani, A. Ashrafi, H. Balaei, A. Razazzadeh, Bio-Corrosion, Mechanical and Microstructural Properties of TiTaMoVZr High-Entropy Alloy Film on Ti–6Al–4V Substrate, Metals and Materials International, (2023).

[87] N.S. Peighambardoust, A.A. Alamdari, U. Unal, A. Motallebzadeh, In vitro biocompatibility evaluation of Ti1.5ZrTa0.5Nb0.5Hf0.5 refractory high-entropy alloy film for orthopedic implants: Microstructural, mechanical properties and corrosion behavior, Journal of Alloys and Compounds, 883 (2021).

[88] P. Hruška, F. Lukáč, S. Cichoň, M. Vondráček, J. Čížek, L. Fekete, J. Lančok, J. Veselý, P. Minárik, M. Cieslar, O. Melikhova, T. Kmječ, M.O. Liedke, M. Butterling, A. Wagner, Oxidation of amorphous HfNbTaTiZr high entropy alloy thin films prepared by DC magnetron sputtering, Journal of Alloys and Compounds, 869 (2021).

[89] D.O. Scanlon, G.W. Watson, D.J. Payne, G.R. Atkinson, R.G. Egdell, D.S.L. Law, Theoretical and Experimental Study of the Electronic Structures of MoO3 and MoO2, The Journal of Physical Chemistry C, 114 (2010) 4636-4645.

[90] Q.-T. Song, J. Xu, (TiZrNbTa)90Mo10 high-entropy alloy: Electrochemical behavior and passive film characterization under exposure to Ringer's solution, Corrosion Science, 167 (2020).

[91] E.A. Gulbransen, K.F. Andrew, F.A. Brassart, Oxidation of Molybdenum 550° to 1700°C, Journal of The Electrochemical Society, 110 (1963) 952-952.

[92] F.Y. Zhou, B.L. Wang, K.J. Qiu, W.J. Lin, L. Li, Y.B. Wang, F.L. Nie, Y.F. Zheng, Microstructure, corrosion behavior and cytotoxicity of Zr–Nb alloys for biomedical application, Materials Science and Engineering: C, 32 (2012) 851-857.

[93] J. Jayaraj, C. Thinaharan, S. Ningshen, C. Mallika, U. Kamachi Mudali, Corrosion behavior and surface film characterization of TaNbHfZrTi high entropy alloy in aggressive nitric acid medium, Intermetallics, 89 (2017) 123-132.

[94] T.A. Parthasarathy, M.G. Mendiratta, D.M. Dimiduk, Oxidation mechanisms in Mo-reinforced Mo5SiB2(T2)–Mo3Si alloys, Acta Materialia, 50 (2002) 1857-1868.

[95] D. Gonbeau, C. Guimon, G. Pfister-Guillouzo, A. Levasseur, G. Meunier, R. Dormoy, XPS study of thin films of titanium oxysulfides, Surface Science, 254 (1991) 81-89.

[96] A.R. González-Elipe, G. Munuera, J.P. Espinos, J.M. Sanz, Compositional changes induced by 3.5 keV Ar+ ion bombardment in Ni-Ti oxide systems, Surface Science, 220 (1989) 368-380.

[97] H. Ikawa, T. Yamada, K. Kojima, S. Matsumoto, X-ray Photoelectron Spectroscopy Study of High- and Low-Temperature Forms of Zirconium Titanate, Journal of the American Ceramic Society, 74 (1991) 1459-1462.

[98] W. Yang, Y. Liu, S. Pang, P.K. Liaw, T. Zhang, Bio-corrosion behavior and in vitro biocompatibility of equimolar TiZrHfNbTa high-entropy alloy, Intermetallics, 124 (2020).

[99] Q. Zhou, S. Sheikh, P. Ou, D. Chen, Q. Hu, S. Guo, Corrosion behavior of Hf0.5Nb0.5Ta0.5Ti1.5Zr refractory high-entropy in aqueous chloride solutions, Electrochemistry Communications, 98 (2019) 63-68.

[100] S. Mendis, W. Xu, H.P. Tang, L.A. Jones, D. Liang, R. Thompson, P. Choong, M. Brandt, M. Qian, Characteristics of oxide films on Ti-(10–75)Ta alloys and their corrosion performance in an aerated Hank's balanced salt solution, Applied Surface Science, 506 (2020).

[101] R. Simpson, R.G. White, J.F. Watts, M.A. Baker, XPS investigation of monatomic and cluster argon ion sputtering of tantalum pentoxide, Applied Surface Science, 405 (2017) 79-87.

[102] B. Gorr, S. Schellert, F. Müller, H.-J. Christ, A. Kauffmann, M. Heilmaier, Current Status of Research on the Oxidation Behavior of Refractory High Entropy Alloys, Advanced Engineering Materials, 23 (2021) 2001047.

[103] Competition of Oxide Scale and Intermetallic Phase Formation with Addition of Al in HfNbTaTiZr Refractory High Entropy Alloy.

[104] E.J. Buchovecky, N. Du, A.F. Bower, A model of Sn whisker growth by coupled plastic flow and grain boundary diffusion, Applied Physics Letters, 94 (2009) 191904-191904.

[105] ASM Handbook: Corrosion, ASM International, 1992.

[106] R. Ghorbani, M. Rahmati, K. Raeissi, A. Hakimizad, M. Santamaria, Effect of Molybdate on Corrosion Performance of Oxide Coating Produced on 7075 Al Alloy Using PEO, Coatings, 12 (2022).

[107] D.A. Stewart, Diffusion of oxygen in amorphous tantalum oxide, Physical Review Materials, 3 (2019).

[108] A. von der Heiden, M. Bornhofft, J. Mayer, M. Martin, Oxygen diffusion in amorphous and partially crystalline gallium oxide, Phys Chem Chem Phys, 21 (2019) 4268-4275.

[109] E.J. Pickering, N.G. Jones, High-entropy alloys: a critical assessment of their founding principles and future prospects, International Materials Reviews, 61 (2016) 183-202.

[110] R. Feng, B. Feng, M.C. Gao, C. Zhang, J.C. Neuefeind, J.D. Poplawsky, Y. Ren, K. An, M. Widom, P.K. Liaw, Superior High-Temperature Strength in a Supersaturated Refractory High-Entropy Alloy, Adv Mater, 33 (2021) e2102401.

[111] G.E. Dieter, D. Bacon, Mechanical metallurgy, McGraw-hill New York, 1976.

[112] D.A. Porter, K.E. Easterling, Phase transformations in metals and alloys (revised reprint), CRC press, 2009.

[113] K.H. Lee, S.-K. Hong, S.I. Hong, Precipitation and decomposition in CoCrFeMnNi high entropy alloy at intermediate temperatures under creep conditions, Materialia, 8 (2019).

[114] C.N.J. Wagner, DIRECT METHODS FOR THE DETERMINATION OF ATOMIC SHORT-RANGE ORDER IN AMORPHOUS SOLIDS, in: S. Steeb, H. Warlimont (Eds.) Rapidly Quenched Metals, Elsevier, 1985, pp. 405-412.

[115] L. Zhou, Q. Wang, J. Wang, X. Chen, P. Jiang, H. Zhou, F. Yuan, X. Wu, Z. Cheng, E. Ma, Atomic-scale evidence of chemical short-range order in CrCoNi medium-entropy alloy, Acta Materialia, 224 (2022).

[116] L.T.F. Eleno, C.G. Schön, J. Balun, G. Inden, Prototype calculations of B2 miscibility gaps in ternary b.c.c. systems with strong ordering tendencies, Intermetallics, 11 (2003) 1245-1252.

[117] T. Mohri, D. de Fontaine, J.M. Sanchez, Short range order hardening with second neighbor interactions in fcc solid solutions, Metallurgical Transactions A, 17 (1986) 189-194.
[118] C.G. Schön, On short-range order strengthening and its role in high-entropy alloys, Scripta Materialia, 196 (2021).
[119] X. Wu, Chemical short-range orders in high-/medium-entropy alloys, Journal of Materials Science & Technology, 147 (2023) 189-196.
[120] X. Chen, Q. Wang, Z. Cheng, M. Zhu, H. Zhou, P. Jiang, L. Zhou, Q. Xue, F. Yuan, J. Zhu, X. Wu, E. Ma, Direct observation of chemical short-range order in a medium-entropy alloy, Nature, 592 (2021) 712-716.
[121] W.-R. Jian, Z. Xie, S. Xu, Y. Su, X. Yao, I.J. Beyerlein, Effects of lattice distortion and chemical short-range order on the mechanisms of deformation in medium entropy alloy CoCrNi, Acta Materialia, 199 (2020) 352-369.
[122] R. Zhang, S. Zhao, J. Ding, Y. Chong, T. Jia, C. Ophus, M. Asta, R.O. Ritchie, A.M. Minor, Short-range order and its impact on the CrCoNi medium-entropy alloy, Nature, 581 (2020) 283-287.
[123] X. Huang, L. Liu, X. Duan, W. Liao, J. Huang, H. Sun, C. Yu, Atomistic simulation of chemical short-range order in HfNbTaZr high entropy alloy based on a newly-developed interatomic potential, Materials & Design, 202 (2021).
[124] P. Hirel, Atomsk: A tool for manipulating and converting atomic data files, Computer Physics Communications, 197 (2015) 212-219.
[125] A.P. Thompson, H.M. Aktulga, R. Berger, D.S. Bolintineanu, W.M. Brown, P.S. Crozier, P.J. in 't Veld, A. Kohlmeyer, S.G. Moore, T.D. Nguyen, R. Shan, M.J. Stevens, J. Tranchida, C. Trott, S.J. Plimpton, LAMMPS - a flexible simulation tool for particle-based materials modeling at the atomic, meso, and continuum scales, Computer Physics Communications, 271 (2022) 108171.
[126] A. Stukowski, Visualization and analysis of atomistic simulation data with OVITO–the Open Visualization Tool, Modelling and Simulation in Materials Science and Engineering, 18 (2010) 015012.
[127] A. Nazarahari, A.C. Fromm, H.C. Ozdemir, C. Klose, H.J. Maier, D. Canadinc, Determination of thermal conductivity of eutectic Al–Cu compounds utilizing experiments, molecular dynamics simulations and machine learning, Modelling and Simulation in Materials Science and Engineering, 31 (2023) 045001.

[128] N. Bertin, R. Carson, V.V. Bulatov, J. Lind, M. Nelms, Crystal plasticity model of BCC metals from large-scale MD simulations, Acta Materialia, 260 (2023).
[129] S. Menon, G. Leines, J. Rogal, pyscal: A python module for structural analysis of atomic environments, Journal of Open Source Software, 4 (2019) 1824.
[130] D. de Fontaine, The number of independent pair-correlation functions in multicomponent systems, Journal of Applied Crystallography, 4 (1971) 15-19.
[131] S.Y. Chen, Y. Tong, K.K. Tseng, J.W. Yeh, J.D. Poplawsky, J.G. Wen, M.C. Gao, G. Kim, W. Chen, Y. Ren, R. Feng, W.D. Li, P.K. Liaw, Phase transformations of HfNbTaTiZr high-entropy alloy at intermediate temperatures, Scripta Materialia, 158 (2019) 50-56.
[132] Y.O. Yildiz, A. Ahadi, M. Kirca, Strain rate effects on tensile and compression behavior of nano-crystalline nanoporous gold: A molecular dynamic study, Mechanics of Materials, 143 (2020).
[133] W. Abuzaid, H. Sehitoglu, Critical resolved shear stress for slip and twin nucleation in single crystalline FeNiCoCrMn high entropy alloy, Materials Characterization, 129 (2017) 288-299.
[134] Z. Li, K.G. Pradeep, Y. Deng, D. Raabe, C.C. Tasan, Metastable high-entropy dual-phase alloys overcome the strength-ductility trade-off, Nature, 534 (2016) 227-230.
[135] J. Moon, Y. Qi, E. Tabachnikova, Y. Estrin, W.-M. Choi, S.-H. Joo, B.-J. Lee, A. Podolskiy, M. Tikhonovsky, H.S. Kim, Deformation-induced phase transformation of Co20Cr26Fe20Mn20Ni14 high-entropy alloy during high-pressure torsion at 77 K, Materials Letters, 202 (2017) 86-88.
[136] O.N. Senkov, D.B. Miracle, K.J. Chaput, J.-P. Couzinie, Development and exploration of refractory high entropy alloys—A review, Journal of Materials Research, 33 (2018) 3092-3128.
[137] H.Y. Yasuda, Y. Yamada, K. Cho, T. Nagase, Deformation behavior of HfNbTaTiZr high entropy alloy singe crystals and polycrystals, Materials Science and Engineering: A, 809 (2021).
[138] A. Ma, A. Hartmaier, Scale bridging modeling of plastic deformation and damage initiation in polycrystals, INTECH Open Access Publisher, 2012.

Appendix

Examples for the LAMMPS input files used in this work are provided to enable reproduction of the results. The user needs to modify these files with the correct set of parameters depending on the intended simulation.

LAMMPS input for Monte Carlo simulations:

```
#USER INPUT
variable filename string H1 #defining input file
variable t equal 300.0 #defining temperature
variable logprefix index VAR          #the name of the saved log file
log VAR.txt append

#SIMULATION SETUP
units          metal
atom_style     atomic
dimension 3
boundary p p p

# ATOM DEFINITION
read_data VAR.lmp
timestep 0.001

# DEFINE INTERATOMIC POTENTIAL
pair_style meam
pair_coeff * * library.meam Hf Nb Ta Ti Zr HfNbTaTiZr.meam Hf Nb Ta Ti

#Define Computes
compute        p all pressure thermo_temp

#EQUILIBRIUM of the input system
reset_timestep 0
velocity all create VAR 12345 mom yes rot no
fix 1 all npt temp VAR VAR S(100.0*dt) aniso 0 0 S(1000.0*dt)
thermo 1000
thermo_style yaml
dump eqdump all atom 1000 Eq_dump_VAR_*
```

```
run 20000
unfix 1
undump eqdump

#HYBRID MONTE CARLO (MC + NPT)
reset_timestep 0
fix 1 all npt temp VAR VAR VAR(100.0*dt) iso 0 0 VAR(1000.0*dt)
fix 2 all atom/swap 100 10 29494 VAR ke no types 1 2
fix 3 all atom/swap 100 10 29494 VAR ke no types 1 3
fix 4 all atom/swap 100 10 29494 VAR ke no types 1 4
fix 5 all atom/swap 100 10 29494 VAR ke no types 2 3
fix 6 all atom/swap 100 10 29494 VAR ke no types 2 4
fix 7 all atom/swap 100 10 29494 VAR ke no types 3 4

#Dumping outputs and restart files
dump 1 all cfg 2000 VAR_*.lmp mass type xs ys zs
dump 2 all atom 2000 VAR_*
dump_modify     1 element Hf Nb Ta Ti
thermo          2000
thermo_style yaml
restart 100000 VAR.restart

#Running the simulation
run             1000000
write_data VAR_Final_*.lmp
```

LAMMPS input for Compression simulations:

```
########################################
#USER INPUTS
variable filename string H1_AN_300_eq #NAME OF THE INPUT FILE
variable T equal 300.0#TEMPERATURE OF THE SIMULATION
variable output_file string H1_AN_300k_Comp_1X1X1_ESR_1%_run_30k
        #NAME OF THE OUTPUT FILE
variable srate1 equal -0.01     #esrate in % per ps (ENGINEERING STRAIN RATE)

########################################
# INITIALIZATION
units metal
dimension 3
boundary p p p
atom_style atomic

########################################
# ATOM DEFINITION
```

```
read_restart VAR.lmp #TO FACILITATE THE SIMULTAIONS, THE
EQUILIBRATION WAS PERFORMED SEPARATELY
timestep 0.001

#######################################
# DEFINE INTERATOMIC POTENTIAL
pair_style meam
pair_coeff * * library.meam Hf Nb Ta Ti Zr HfNbTaTiZr.meam Hf Nb Ta Ti #HAUNG
INTERATOMIC POTENTIAL

#######################################
# DEFINE COMPUTES

compute peratom all pe/atom #COMPUTE THE ENERGY OF ATOMS

#######################################
# SHORT EQUILIBRATION BEFORE COMPRESSION
reset_timestep 0
timestep 0.001
velocity all create VAR 12345 mom yes rot no
fix 1 all npt temp VAR VAR VAR(100.0*dt) iso 0 0 VAR(1000.0*dt) drag 0.2
thermo 1000
thermo_style custom step lx ly lz press pxx pyy pzz pe temp
run 1000
unfix 1

# FINAL LENGTH OF THE SYSTEM IS SAVED FOR STRAIN CALC
variable temporary equal "lx"
variable L0 equal VAR
print "Initial Length, L0: VAR”

#######################################
#NOW COMPRESSION SIMULATION
# DEFORMATION
reset_timestep 0        #RESETING THE TIME TO EASE THE DEFORMATION
#CALC
fix 1 all npt temp VAR VAR VAR(100.0*dt) y 0 0 1 z 0 0 1 drag 0.2 #TO
EQUILIBRATE THE SYSTEM UNDER DEFORMATION
fix 2 all deform 1 x erate VAR units box remap x
variable strain equal "(lx - v_L0)/v_L0"
variable p1 equal "v_strain"
variable p2 equal "-pxx/10000"
variable p3 equal "-pyy/10000"
variable p4 equal "-pzz/10000"
fix def1 all print 100 "S VAR VAR VAR VAR" file VAR.txt screen no

#DUMPING THE OUTPUT
dump 1 all cfg 500 dump.comp_*.cfg mass type xs ys zs c_csym c_peratom fx fy fz
dump_modify     1 element Hf Nb Ta Ti
thermo 1000
```

```
thermo_style custom step v_strain temp v_p2 v_p3 v_p4 ke pe press

#RUNNING THE SIMULATION
run 30000

########################################
# SIMULATION DONE
print "All done"
```